University of Wisconsin Milwaukee
UWM Digital Commons

May 2013

System for Detection of Defects in Cables of Bridge Structures

Emad Ismail Abdel Salam
University of Wisconsin-Milwaukee

SYSTEM FOR DETECTION OF DEFECTS IN CABLES OF

BRIDGE STRUCTURES

by

Emad Abdelsalam

A Dissertation Submitted in

Partial Fulfillment of the

Requirements for the Degree of

Doctor of Philosophy

in Engineering

at

The University of Wisconsin – Milwaukee

May 2013

ABSTRACT

SYSTEM FOR DETECTION OF DEFECTS IN CABLES OF BRIDGE STRUCTURES

by

Emad Abdelsalam

The University of Wisconsin – Milwaukee, 2013
Under the Supervision of Dr. Al Ghorbanpoor

Over the last 75 years, many cable-supported bridges have been built in America, Europe, Asia and other parts of the world. However, over the years these bridges have aged and been exposed to environmental conditions such as rain, snow, de-icing and harmful chemicals. These conditions cause various levels of deterioration in bridges, particularly corrosion. Corrosion causes a loss of cross-section in the steel, adversely affecting the bridge's capacity to carry its service loads, and can possibly cause bridge failures. Although many methods have been attempted to inspect these bridges, most have offered limited success. In the recent years, it has been shown that the Magnetic Flux Leakage (MFL) method, may offer the performance and practicality needed to inspect similar structures such as post-tensioned (P-T) tendons in segmental concrete bridges. This thesis offers a design for an NDE system based on the MFL method to inspect the entire length of the cables of cable-stayed bridges. The thesis also addresses the feasibility of integrating a secondary NDE method, the Magnetostrictive (MS) method, with the MFL system to provide a complete assessment of these bridges including the anchorage area. As a part of this study, prototype models of the MFL and MS systems were built. Past experimental results on a real P-T bridge cables have shown that the MFL is capable of

ii

detecting as small as 1% of the cross sectional loss in bridge cables due to corrosion. Experiments carried out on a simulated anchorage area of 13 strands showed that the MS test is capable of detecting steel defects from single to several broken strands. Furthermore, based on simulation and experimental results, a more practical magnet design has been proposed to enhance the bridge cable inspection in future.

iv

ACKNOWLEDGMENT

_____

This thesis wouldn't have been possible without the support of my family and friends. Thanks to my mother Lutfieh Hamadeh and my father Ismail Abdelsalam, my wife Luz Gonzalez, my two kids Ayah and Usama, and my sisters and friends for their continuous support and encouragements. Special thanks to Prof. Al Ghorpanpoor and committee members for their support and directions throughout this work.

TABLE OF CONTENTS

_____

RESULTS & DISCUSSION **69**

LIST OF FIGURES

xvii

LIST OF TABLES

CHAPTER 1

INTRODUCTION

1.1 Motivation and Objectives

In the last seventy five years, a large number of bridges have been built in the United States and around the world. A majority of these bridge structures rely on stressed steel cables to carry all relevant loads from traffic, environmental effects such as wind and temperature, earthquake, and the weight of the structure. Over time, these bridges age and are exposed to environmental conditions such as rain, snow, de-icing and harmful chemicals. These conditions cause various levels of deterioration in the steel, particularly corrosion. Corrosion causes a loss of cross-section in the steel, adversely affecting the bridge's capacity to carry its service loads, and can possibly place the bridge's performance and safety in a critical condition. Several cases of post-tensioned (P-T) cable corrosion in bridges have been reported throughout the world. For example, in the summer of 1999, Florida Department of Transportation (FDOT) discovered corrosion in multiple bridges including the Niles Channel Bridge in the Florida Keys [1]. Also, in 2000, a fractured tendon and advanced stages of corrosion in the cable anchorage area were observed during a routine bridge inspection by FDOT at the Mid-bay Bridge near Destin [1]. Moreover, similar problems have been discovered at the Skyway Bridge in Tampa, FL [1]. Also, bridge collapses due to excessive corrosion have been reported in

the United States and in other parts of the world [2-7]. According to the above, there is a direct need for developing appropriate inspection methods to effectively detect corrosion in bridge cables and evaluate the structural integrity, performance and safety of such bridge structures.

While different defects are formed in various structural members in bridge structures, the focus of this work is placed on the corrosion problems in primary steel cables of large bridges. Such cables are normally enclosed in protective polyethylene or metallic ducts or wrapping materials to prevent exposure to moisture and outside environment. As such, no visual evaluation is possible and there have been no practical commercial technologies that could be used to evaluate the condition of these bridge cables.

There are many NDE methods such as X-ray, Ultrasound, Electrical Resistance gages, Time Domain Reflectometry, Linear Polarization, vibration techniques, Surface Potential Survey and Themography that may be applicable to inspection of bridge cables [8-10, 21-29, 35-44]. Although these NDE methods may seem to be able to offer some evaluation capabilities for bridge cables, it has been shown that they are ineffective in the detection of corrosion in bridge cables [13-51]. The MFL concept has been successfully demonstrated to be effective in detecting defects such as loss of section and corrosion in external P-T ducts of concrete bridge structures [46- 51].

1.2 Proposed Research

Based on the literature survey conducted as a part of this research, it was found that only MFL method can offer both the performance required to detect corrosion in bridge steel cables and the effectiveness for field applications [46-51]. Therefore, to address the problem of detecting corrosion in bridge cables, this work presents development and laboratory evaluation of an MFL system that is capable of inspecting and detecting steel corrosion in cable supported bridge structures.

The basic principle behind the MFL technology is to apply a magnetic field near the surface of the steel cable and monitor the variation of the magnetic flux in the cable. The magnetic field should be strong enough to adequately penetrate through the steel cable. Since steel is a ferromagnetic material, magnetic flux will flow through the steel and will be confined within the steel structure. However, if there is a deficiency in the physical structure of the steel, such as a loss of cross section due to corrosion or fracture, the magnetic flux will leak to the surrounding environment. This is usually referred to as "magnetic fringing" phenomenon. To take advantage of this phenomenon, magnetic sensors, like Hall-effect, are placed near the surface of the cable where an electrical signal can be observed and recorded in the form of voltage variations due to magnetic fringing. This signal, which is an indication of the presence of the flaw, can then be used to evaluate the severity of the deterioration. The magnitude and duration of the signal varies based on several factors, including the depth, size and shape of the defect in the steel cable.

A primary limitation of the MFL technology is that close access to the surface of the steel cable is required. Unfortunately, there are regions where the steel cables in bridges are embedded in thick concrete in the anchorage areas where close access to the cables is

not possible. To overcome this problem, a different technique, such as the Magnetostrictive (MS) method, may be used.

The basic principle behind the MS method is to transmit a traveling mechanical, acoustic, or electromagnetic wave along the length of the steel cable that is embedded in concrete and monitor the waves that are reflected from defects in the cable. This can be accomplished by introducing a time varying magnetic field pulse generated by a coil that is wrapped around the cable. The magnetic pulse causes very small change in the physical dimension of the steel. As a result, guided (acoustic) waves are generated in the steel and propagate along the length of the cable and reflect back from boundaries such as the cable ends, and other discontinuities including defects. The reflected waves cause reverse localized disturbances to the magnetic field. These disturbances can then be detected by means of using a coil or magnetic sensors. Combining a permanent magnet and integrating the system with an external coil with a radio frequency (RF) pulse at one end of the steel cable can accomplish this. The various reflected waves from discontinuities in the steel can then be captured and analyzed to evaluate steel condition in inaccessible areas.

With the above discussion in mind, the goal for this research is to combine both the MS and MFL methods and to design a system that would provide complete information on the condition of the steel in cable-supported bridges.

Therefore, to address the problem of detecting corrosion in bridge cables, it is proposed to develop an MFL/MS system that is capable of inspecting the entire length of bridge cables outside and within the anchorage areas.

1.3 Outline of Thesis Contents

In chapter 2, an overview of the applicable NDE techniques that have been attempted for inspection of corrosion defects in cable bridges, along with a summary of the advantages and disadvantages of each technique are presented. The following NDE methods will be reviewed: Radiography, Computed Tomography, Ultrasound, Acoustic Emission, Remnant Magnet and Magnetic Flux Leakage. A proposed system solution is also presented at the end of the chapter.

In chapter 3, the theory and concept of the Magnetic Flux Leakage (MFL) are provided. Also an overview of the magnetism concept, material classification based on their magnetic property and examples of corrosion defects in steel is presented. The chapter discusses the effect of the density of the magnetic field on defect detection. Mathematical models for relevant types of flaws are also discussed. The theory of Magnetostricitve method and general guided-wave propagation concepts are also presented.

Chapter 4 discusses a prototype MFL system that was built for the purpose of proving the concept and evaluating its performance. Also, the laboratory setup and experiments, including the construction of a typical cable used in cable bridges, are presented. The MS experiments were designed to explore the feasibility of this method for detecting corrosion defects in the anchorage of area of bridge cables. An experimental bridge cable with simulated anchorage section was also built. The experiments were carried out for the MFL system and the MS system using varying sizes of defects fabricated in the steel cable, including surface corrosion, and a single broken wire in a strand to several broken strands.

The results of the experimental work are discussed in chapter 5 and a more practical and efficient system design with cylindrical magnet orientation is presented in chapter 6. Numerical analysis for the new magnet design that shows improved performance and field applications is also presented. Finally, the research conclusions and recommendations for future work are discussed in chapter 7.

CHAPTER 2

NONDESTRUCTIVE EVALUATION METHODS

2.1 Introduction

In this chapter, a review of all applicable methods that may be used in nondestructive evaluation (NDE) of cable-supported bridge structures is presented. Nondestructive evaluation can be defined as an examination/inspection for an object to reveal its mechanical or behavioral characteristics in terms of internal structural, geometry, material characteristics, content and defects without inducing any damage to the structure [2]. Based on the literature survey conducted as a part of this research, the applicable non-destructive methods for detection of corrosion in cable supported bridges may be summarized as follows:

2.2 Visual Inspection

Visual inspection (VI) involves inspecting a structure visually and looking for signs of corrosion or other damage [10]. Visual inspection can be used virtually through all stages of product development and construction, starting from raw material and ending with the finished product. The VI can be used for inspecting gas pipes, tanks, building, bridges,

power generating turbines, and power plants. There are several factors that can affect the outcome of VI such as condition of the object under test, environmental conditions and the skill set for the inspector [8-10]. The condition of the object under test includes material, shape, size, access, and surface condition.   The shape of the object dictates the amount of light, and/or orientation of viewing angle to insure that all surfaces of the object are examined. The size of the object directly influences the pattern, direction and speed of the examination. Surface condition such as cleanness, rust and contamination may prohibit or limit the inspection process and results.

Environmental conditions include lighting, temperature and weather. Sufficient amount of lighting should be available to ensure exposure of the entire surface of the object under test. On the other hand, an inadequate amount of light could inhibit the object's attributes to be revealed; for example because of shadowing. Excessive light (brightness), however, could also inhibit exposing the attributes of the object under test because excessive reflection reduces the ability of the eye to see small details [10]. If the object under test is inspected under high environmental temperature, the temperature may cause a distortion to the field of view because of heat waves. The inspector's experience and health condition (stress, tension and fatigue) may adversely affect the perception of the eye and, consequently, affect the inspection results.

Although there are many tools, such as cameras, magnifiers, rules, micrometers, monitors and scopes, that can be used to aid during VI, the inspector's eyes are the primary inspection tool. Since VI depends primarily on the eye for inspection, the eye is required to be in continuous movement (back and forth) during the inspection [10]. This rapid movement of the eye, after a long time of inspection, could cause muscle fatigue in the eye and affect the inspection results. Another variable that could limit the VI is

accessibility of the object under test. If the object is hidden, partially or completely inaccessible, the inspector may not be able to see the object and fully examine it.

Although it is useful, VI is limited to visible signs of deterioration that appears at the outer surface of the material such as corrosion, erosion, cracks, voids, wear and fatigue [8-10]. Also, depending on the structure of the object under test, a deterioration at the outer surface of the object may or may not be a sign of internal gross damage.

Unfortunately, visual inspection cannot detect non-visible or hidden corrosion, especially for cable-stayed bridge, because the steel cable is covered under one or more protective layers. However, even if the VI is used to inspect the cables of bridge structures, all protective layers (polyethylene and grout) will have to be removed which is expensive but not very practical. However, the visual inspection of cables in bridges is sometimes performed in a few local areas to achieve an understanding of the condition of the cables. In such cases, the wires or strands that are bundled together to form a bridge cable are pried open with a tool (i.e., wooden-wedges) so they can be inspected. This can only be done to a limited portion of the cable (a few feet), making VI impractical, inefficient and very costly.

2.3 Radiography

Radiographic methods use radiation beams to detect defects in the materials under inspection [8-12]. Typically, the source of the beam is either Beta or Gamma particles. X-rays are produced by accelerating electrons at high speed under high voltage to strike a filament material to produce photons [8-10, 12]. The photons can then be directed at the

right angle towards the target under test using a special apparatus. The energy of the produced photons is given by [12]:

$$E \ = \ h\,v \ = \ h\,c \ / \ \lambda \qquad\qquad (2.1)$$

Where,

h : *Plank's constant*

v : *Frequency of radiation (Hz)*

c : *Speed of light (m/s)*

λ : *Wavelength (mm)*

Figure 2.1 shows a general setup for an X-ray inspection method with a material under inspection. X-rays or Gamma-rays enter the material under test from one side and some or all exit from the other side. The beam usually travels in a straight line. However, it goes under scattering, and absorption process; the amount of scattering and absorption depends on the material's molecular structure. The beams that penetrate through the material are detected and recorded either on a real-time digital monitoring receiver or on a special radiographic detector to produce 2D images [13-19].
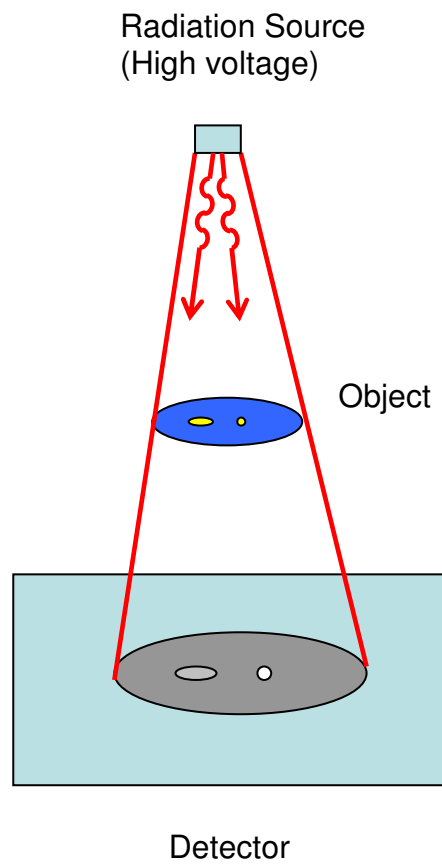
Figure 2.1 X-ray Method: X-ray diagram showing radiation beams penetrating an object and being collected at the receiver end to generate an image.

Images produced from the X-ray exposure are usually gray-scale with varying intensity based on the amount of radiation that is collected at the receiver side. These images are usually poor quality and are not sufficient to clearly show the presence of flaws. Also, the orientation of scanning has to be taken into consideration when imaging steel with with a small loss of section or defect since the defect may be masked by the total mass of the steel. This will make it difficult to detect small defects in 2-D X-ray images. X-ray systems could be portable scanning devices, but special protocol has to be followed to ensure the safety of the operators and other personnel during the radiation exposure process [13, 14, 16, 18]. Although there are advantages for using X-ray systems, including detecting internal defects [9], they require a great amount of radiation to penetrate thick and dense materials such as steel cables in cable supported bridges. Such applications of X-ray technique will require a large source of high voltage power to meet the demand for higher radiation and operation of the system. Providing such high power at the bridge site or in the field and installation of a large testing system on a bridge cable can become difficult. These make X-ray technique a non-field-worthy option for inspection of bridge cables.

2.4 Computed Tomography

Computed Tomography (CT) uses X or Gamma beams but with the consideration of the beam attenuation within the material under inspection. As the beams are transmitted to the material under inspection in straight lines, some partially get absorbed and scattered due to variations in the material's microstructure [12]. The remaining beams travel through the material and the attenuation is measured at the receiver end [12, 21]. The extent of the beam attenuation depends on the atomic structure and atomic density of the material under inspection and is given by [12, 21]:

$$I = I_0 e^{-\alpha x} \qquad (2.2)$$

Where,

I: Intensity of the beam exiting the material

I_o: Intensity of the beam entering the material

α: Attenuation coefficient

x: Thickness of the material under inspection

Figure 2.2 shows a general setup for imaging with computed tomography method. It also shows how the beams travel through different material under inspection.
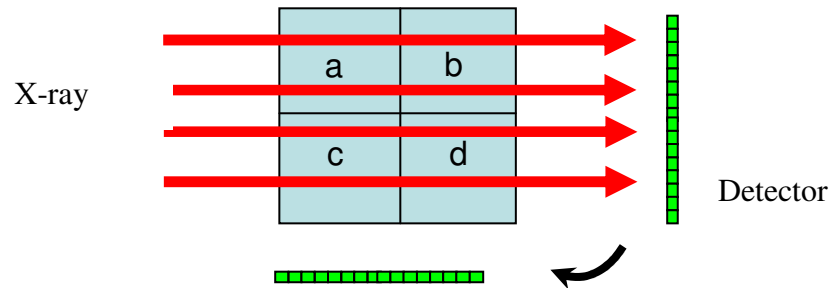
Figure 2.2 Computed Tomography Method: Image reconstruction by rotating the detectors around the material and continually measuring attenuation.

By rotating the detector around the material under inspection, and measuring attenuation, one can produce 2D and 3D images of the internal structure of the material.

CT exhibits the same limitations of X-ray. As such, it has been shown that computed tomography is capable of detecting only relatively large losses of cross section in bridge cables due to corrosion or fractures [21]. Computed Tomography devices are generally slow in operation and are not field worthy [21].

2.5 Ultrasound

The Ultrasound technique works on the concept of generating ultrasonic waves that travel through the material under inspection while monitoring the reflected waves [8-12]. The ultrasonic waves are typically in the range of 20 KHz to 10 MHz. The waves are usually generated by a transducer (crystal) placed at the surface of the material as seen in Figure 2.3. In ultrasound testing, the transmitter and receiver are usually integrated into one device.

Transmitter and receiver are integrated into one device

Defects of different type of material
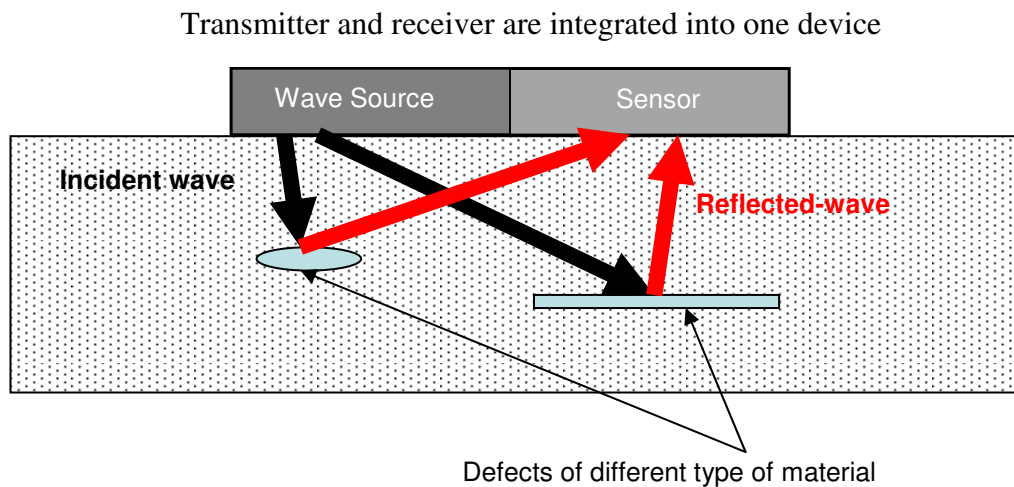
Figure 2.3 Ultrasound Method: Ultrasonic waves are generated from crystal transducer at the surface of the material. Showing reflected waves from defects inside the material.

When ultrasonic waves travel through different types of medium, they undergo reflections and refractions at the boundaries of these media. This interaction at the boundary of the media is due to the difference in their acoustic impedance. This is an important feature of the ultrasound method because it allows the distinction of defects/anomalies from the material. Defects within the material have different types of

acoustic properties than the material, which allow the waves to reflect at their boundary interface with the material. Consider a set of waves that are traveling through material # 1 and then through material # 2, each with acoustic impedance of Z1 and Z2, respectively. When the waves arrive at the interface between the two materials, some of the waves reflect to material #1 and the rest are transmitted into the second material. The amount and direction of reflected and transmitted waves depend on the acoustic characteristics of the two materials and the magnitude and angle of the incident wave, as seen in Figure 2.4.
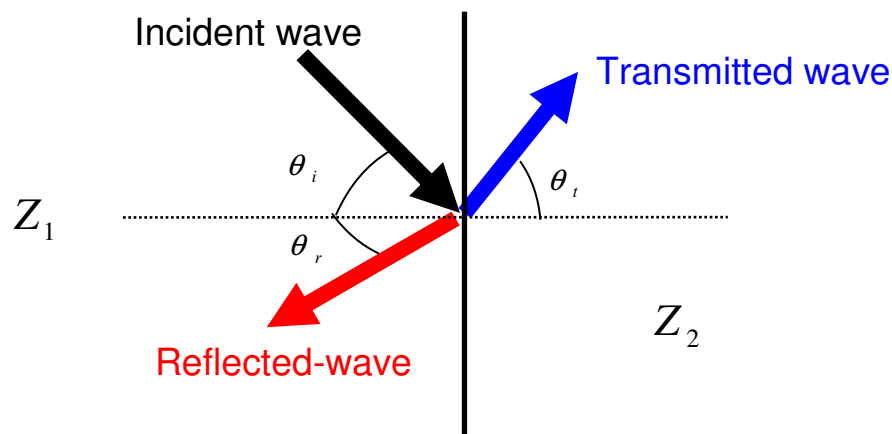
Figure 2.4 Ultrasound Method: Diagram demonstrating wave reflections at interface of two materials with different acoustic impedances.

The percentage of the reflected and transmitted waves can be calculated based on [8-12]:

$$R = \frac{Z_2 \cos \theta_i - Z_1 \cos \theta_t}{Z_2 \cos \theta_i + Z_1 \cos \theta_t} \qquad (2.3)$$

$$T = \frac{2 Z_2 \cos \theta_i}{Z_2 \cos \theta_i + Z_1 \cos \theta_t} \qquad (2.4)$$

Where,

Z_1 & Z_2 : *The acoustic impedance for material one and two respectively*

R : *Reflection coefficient*

T : *Transmission coefficient*

θ_i : *Angle of incident wave*

θ_t : *Angle of transmitted wave*

θ_r : *Angle of reflected wave*

If θ_i is at 0°, the Incident wave is perpendicular to the interface boundary, and the reflection coefficient can be reduced to:

$$R = \frac{Z_2 - Z_1}{Z_2 + Z_1} \qquad (2.5)$$

Table 2.1 shows the acoustic impedance for selected materials. If Z_1 is equal to Z_2, then there will be no reflected wave. However, if we consider a concrete to steel interface and assuming a perpendicular incident wave, then we will have 74% of the wave reflected.

Table 2.1 Acoustic impedances for selected material [9]

Material	Specific acoustic impedance, kg/(m^2 s)
Air	0.4
Water	0.5 x 10^6
Soil	0.3 to 4 x 10^6
Concrete	7 to 10 x 10^6
Steel	47 x 10^6

The reflected waves can be captured by the same transmitting transducer or by another one, where they are converted to electrical signals for processing. Figure 2.5 shows a general block diagram for an ultrasound system. From the reflected waves, one can determine material characteristics, density and geometry of the material, and the presence of defects. 2D and 3D images can be obtained by cross-scanning the surface of the material under test.

The Ultrasound method has many applications in industry for detecting cracks and defects in pipes, aircraft inspection and properties of material [9]. It also has applications in imaging in medicine, such as guided ultrasound for surgery, diagnostics and imaging of soft tissue [12]. Ultrasound can reveal internal structures of material under test, just like X-ray, but without the risk of health hazards. It can inspect and penetrate almost any material including ceramic, metal, concrete, etc. However, it requires significant operator training. Large areas or volume of materials cannot be tested practically, and it can be expensive. Most of the sensors that are available require direct contact with coupling material such as water or gel [8-12].
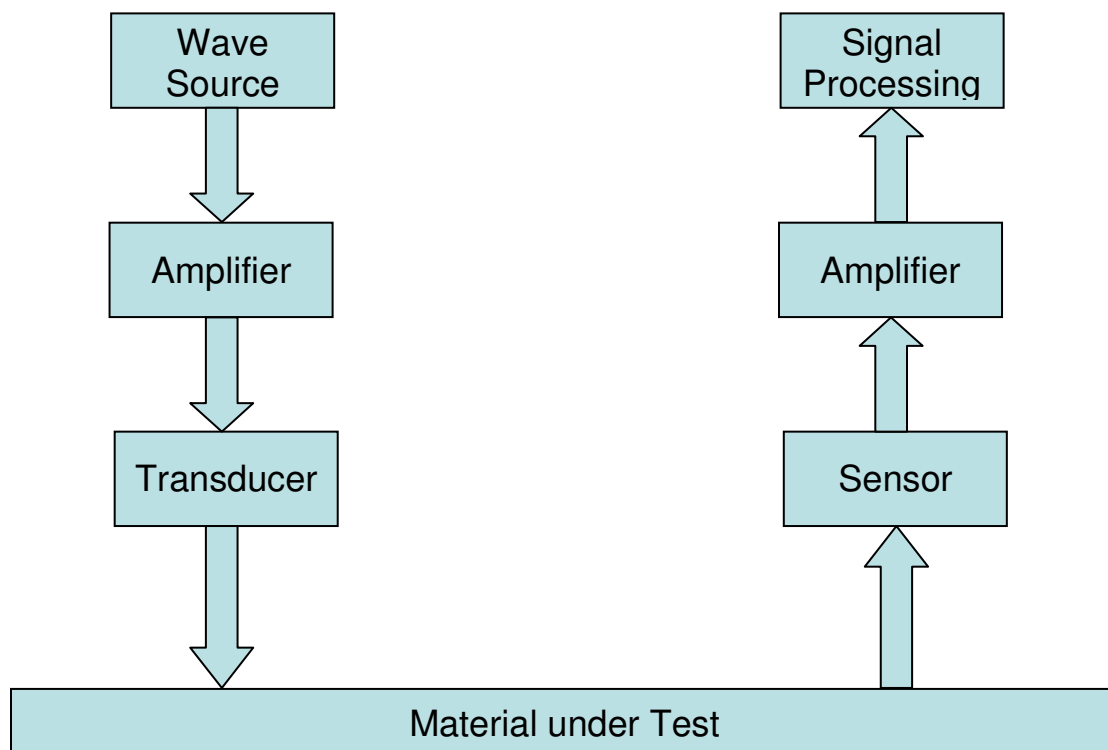
Figure 2.5 Ultrasound: Block Diagram for a typical ultrasound system.

2.6 Acoustic Emission Monitoring

The concept of Acoustic Emission monitoring is based on the principle that mechanical waves are generated when damage occurs in materials. The waves could be generated, for example, from a crack or fracture of steel wires when stored energy is released due to the growth of a crack or defect. The waves created from such events travel in the medium of the material with a constant speed. In order to capture the waves, a real-time monitoring of the material under test is needed. Sensors are usually placed close to the source of energy release and typically installed on exposed surface of the material, as seen in Figure 2.7 below. Sensors capture the traveling waves and generate relevant electrical signals. These signals are usually stored for post-processing and data analysis where various signal characteristics are evaluated and correlated to the defect, see Figure 2.6 below. In this method only new damages can be detected, as long as it is continuously being monitored. As such, existing damages cannot be detected [8-10, 28].
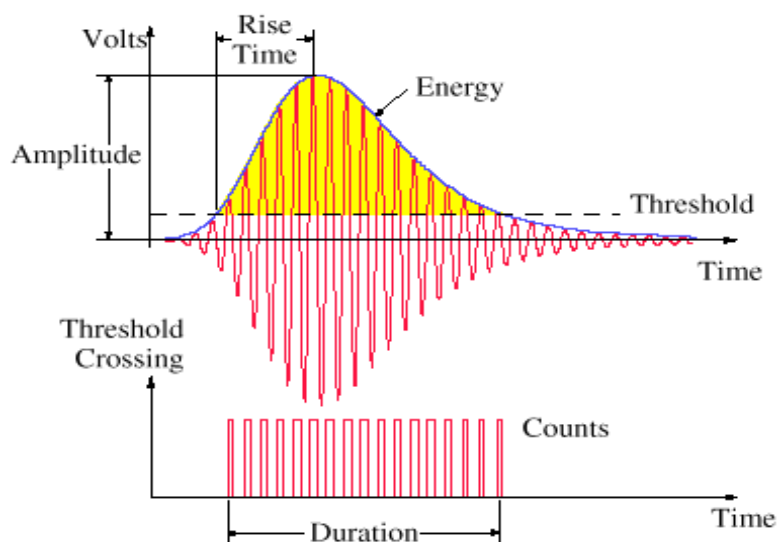
Figure 2.6 Acoustic Emissions: An example of acoustic emission
signal caused by a mechanical damage to material under monitoring [45].
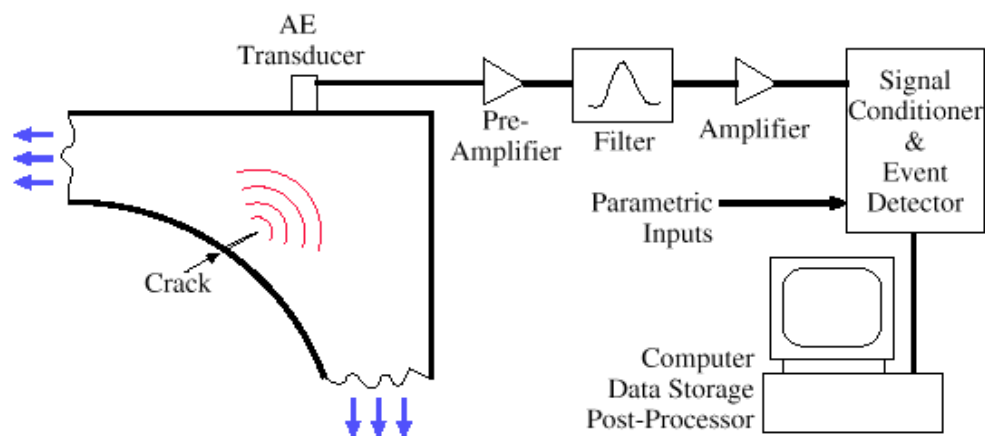
Figure 2.7 Acoustic Emissions: Block diagram for a typical acoustic
emission system [45]

2.7 Magnetic Flux Leakage

The concept of magnetic flux leakage is based on applying an external magnetic field to a

ferromagnetic object under test, while continuously scanning the entire length of the

object. As a result, the object under inspection gets magnetized and flux lines flow within

the object. The stronger the applied magnetic field, the higher the number of flux lines up

to the level of saturation. Magnetization of an object depends on the property of the

material and it is strongly favorable for ferromagnetic materials such as steel. If a steel

bar or cable is exposed to a magnetic field, flux lines flow in straight lines inside the

object in a direction from the north pole to the south pole of the magnet. As such, the flux

lines inside the steel bar or cable are confined within the steel as long as there are no

physical changes. However, if there are physical changes, such as loss of cross section

due to corrosion or fracture, the flux lines leak outside the steel and into the surrounding area causing localized fluctuations in the main magnetic field. These fluctuations can be detected by using magnetic sensors, such as Hall-effect, to determine the presence and magnitude of a defect.

Although MFL is very successful in detecting small and large flaws, it cannot be used to inspect the inaccessible areas of structures or bridges, particularly in the cable anchorage area [46-51]. The MFL method is described in more detail in Chapter 2, where materials are classified based on their magnetic characteristics and mathematical models for selected defects [8, 9, 30-33].

2.8 Remnant Magnetism

The Remnant Magnetism (RM) is similar to the concept of the MFL as described in the previous section. However, RM uses a high level of magnetic field to saturate the material under test (typically steel). The flux fluctuation can then be measured with Hall-effect sensors, or coils [8-10, 33], where the measurements can be taken with or without the active field. Without the active field, the measurements are based on the fluctuation from the residual magnetic field caused by any existing flaws. Unlike the MFL method where there is no need to saturate the test subject, the RM is based on using a time-varying magnetic field that requires coils that use a significant amount of AC power. Although RM is successful in detecting small and large flaws, the disadvantage of power and significant equipment infrastructure requirements makes it unsuitable for field applications to inspect bridge cables.

2.9 Summary and Proposed Research

There are other NDE methods such as Electrical Resistance, Time Domain Reflectometry, Linear Polarization, Surface Potential Survey and Themography that may be applicable to the inspection of bridge cables. Details of these methods can be found in [8-10], [21-29] and [35-44]. Although, theoretically, any of the above mentioned NDE methods can be used for inspection of steel of cable bridges, many of them suffer practical limitations. MFL has been successfully demonstrated to detect defects, loss of section and corrosion in reinforced, pre-stressed and post-tensioned concrete structures [46-51]. As such, based on the literature survey, it seems that only MFL would offer both the performance required to detect defects in steel and provide practicality for field application. Therefore, to address the problem of detecting corrosion in bridge cables, it is proposed to develop an MFL/MS system that is capable of inspecting the entire length of bridge cables outside and within the anchorage areas.

CHAPTER 3
THEORY AND CONCEPTS

_____

3.1 Introduction

The previous chapter presented a review of all applicable methods that may be used in the nondestructive evaluation of cable-supported bridge structures. It was also shown that most of these methods suffer from practical limitations, which make them unsuitable for inspection and evaluations of cable-supported bridge structures. However, the magnetic flux leakage (MFL) technique has been successfully demonstrated to detect loss of section due to corrosion in pre-stressed and post-tensioned concrete structures [46-51]. As such, based on the literature survey, it seems that only MFL method can offer both the performance required to detect defects in steel and the required practicality for field application. Therefore, in this chapter, the theory and concept of the MFL method is provided. An overview of the magnetism concept, material classification based on their magnetic properties and examples of corrosion defects in steel are presented. This chapter also discusses the effect of the density of the magnetic field on defect detection. Mathematical models for relevant types of flaws are also discussed. The theory of Magnetostricitve method and general guided-wave propagation concepts are also presented.

3.2 Magnetic Flux Leakage

An understanding of the principles of magnetism, classification of magnetic materials and their natural performance is presented here. Figure 3.1 shows a permanent magnet bar to demonstrate the concept of magnetism.
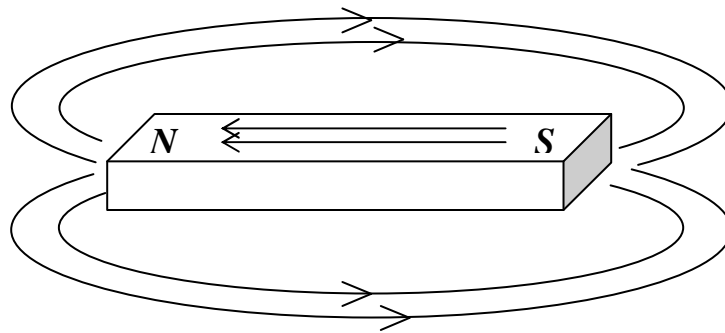
Figure 3.1 A Permanent magnet bar to demonstrate magnetism

By definition, a magnet has two poles; a north-pole and a south-pole. The interaction between the two poles of a magnet is known as magnetic field **H**, measured in Ampere/Meter (A/m). The magnetic field is represented by flux lines that travel from the north-pole to the south-pole outside the magnet as seen in figure 3.1. However, the flux lines travel in an opposite direction, from south-pole to north-pole, inside the magnet. The flux lines are vector quantities (i.e., has magnitude and direction) and they reflect the strength of the magnet; the stronger the magnet, the higher the density of the flux lines. The spacing among the flux lines is a measure of the flux density **B**, measured in Tesla (T); the closer the distance among the flux lines, the higher the flux density. However, in order for the flux lines to exist or travel, they will need a path or a medium, such as air, to

travel through. The path or medium must have certain properties to permit the magnetic flux to pass through. These properties are referred to as "magnetic permeability" and the behavior of the flux lines is governed by the basic principles of magnetism. These principles can be summarized as follows:

1. Flux lines travel through the path of least resistance; which in magnetic terms is the path within a medium with greatest permeability.

2. Flux lines repel each other if their flow direction is the same, or flux lines can never cross each other.

3. Flux lines always travel from the north-pole to the south-pole in a closed loop outside the magnet.

Also, the relationship between the magnetic field and the magnetic flux density is non-linear, as shown in figure 3.2
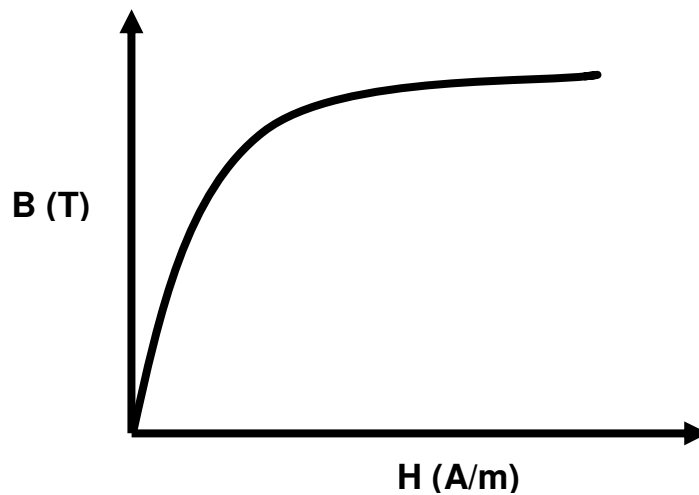
Figure 3.2 Relationships between the magnetic field and the magnetic flux density

When a magnet is placed near a ferromagnetic object; for example steel, the flux lines are channeled through the material to form an induced magnetic flux as seen in Figure 3.3 below.
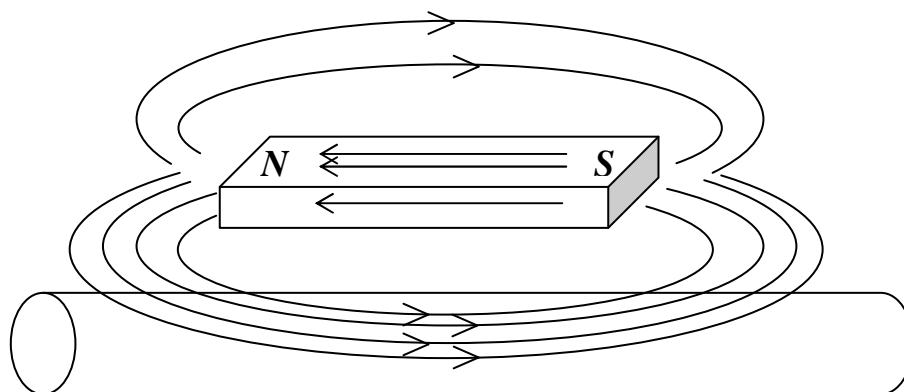
Figure 3.3 Magnetic flux inside a steel bar

The flux density in the material depends on the strength of the external magnetic field and the type of material. Materials react differently to magnets based on their chemical and mechanical structure and how they permit the flux lines to channel through them. Materials, based on their magnetic characteristics, can be classified as diamagnetic, paramagnetic, ferrimagnetic and ferromagnetic. A diamagnetic material resists the magnetic force and has low permeability to allow flux lines to travel through it. An example of such material is bismuth or helium. If the material allows some of the flux lines to travel through it, and if the flux inside is more than the flux outside, then they are called paramagnetic. An example of a paramagnetic material is aluminum (AL). However, if the material allows large number of the flux lines to pass through it, (i.e., if the flux inside the material is much more than the flux outside it) the material is classified as ferromagnetic or ferrimagnetic. An example of ferromagnetic material is steel and an

example for a ferrimagnetic material would be iron oxide (FeO). Ferrimagnetic and ferromagnetic materials remain magnetic as long as they are kept below a specific temperature (Curie temperature). Ferromagnetic material has higher Curie temperature than ferrimagnetic. In ferrimagnetic material, some magnetic dipoles (very small regions in the material) are aligned in one direction and others are in an opposite direction. However, in ferromagnetic material, majority of the magnetic dipoles are aligned in one direction.

Since we are interested in inspecting steel, it is very important to understand the properties and behavior of ferromagnetic materials. As such, a review of the basic properties of the ferromagnetic materials is provided next.

Ferromagnetic materials exhibit physical response or changes when subject to an external magnetic field. This response is shown as an alignment of their magnetic dipoles, magnetic moments, parallel to the direction of the external magnetic field. As such, ferromagnetic materials usually carry greater flux lines through them than the surrounding air, up to a limit. When they reach this limit they become saturated and behave as a transparent medium. When saturation level is achieved, full alignment of the magnetic dipoles is resulted. However, below this saturation level the relation between the external magnetic field and the density of flux lines passing through them is non-linear, as described in figure 3.2. Flux lines always leave the surface of ferromagnetic materials at a right angle.

The MFL method is based on applying a static magnetic field to a ferromagnetic material, like a steel bar, and continuously scanning the surface to monitor and detect fluctuations in the magnetic flux caused by discontinuities, or flaws, inside the steel. When applying a

magnetic field to a ferromagnetic material, the magnetic dipoles orient themselves in the same direction of the magnetic field. The greater the magnetic field, the more alignment of the dipoles until the material reaches its saturation limit. The alignment of the magnetic dipoles allows the magnetic flux lines to pass through the steel, as seen in figure 3.4. The stronger the magnetic field, the greater the density of the flux lines in the steel.
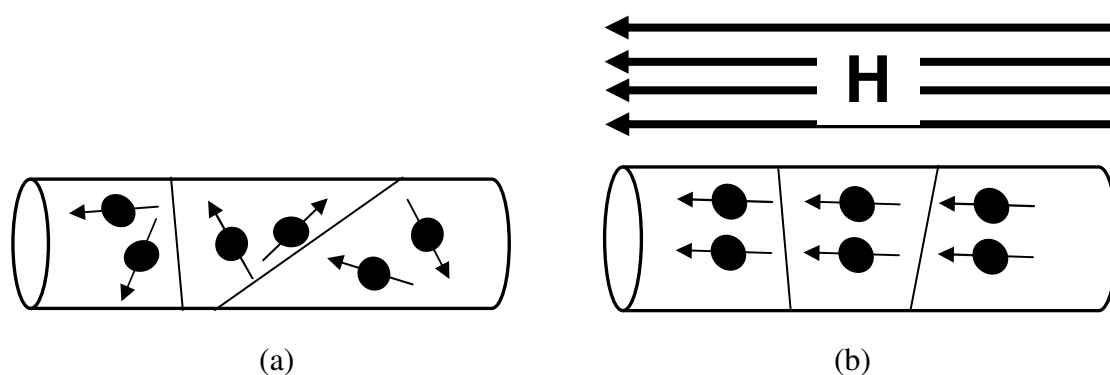
Figure 3.4 Alignment of the magnetic dipoles (a) no magnetic field, (b) with the direction of the magnetic field

The flux lines in the steel will be confined within the steel as long as there are no physical changes. However, if there are physical discontinuities in the steel, such as loss of cross section or corrosion, the magnetic flux lines will leak outside the steel to the surrounding area. These fluctuations can then be detected by Hall-effect sensors to indicate the presence and magnitude of flaws in the steel as seen in figures 3.5 and 3.6.
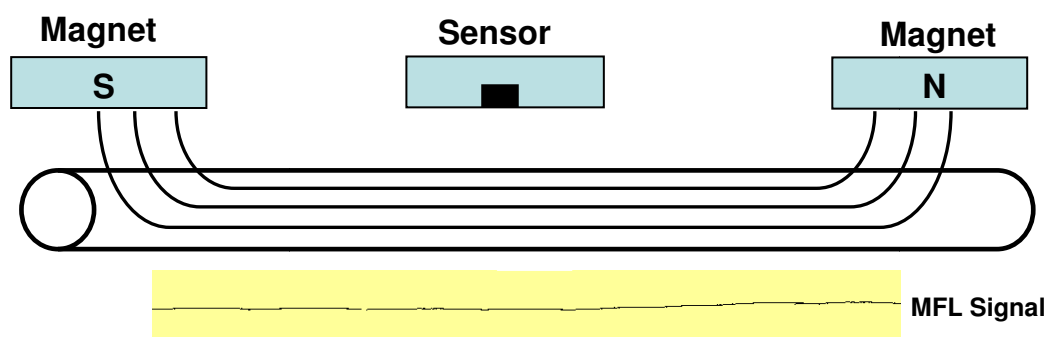
Figure 3.5 Demonstrating MFL concept with no flaw in a steel bar
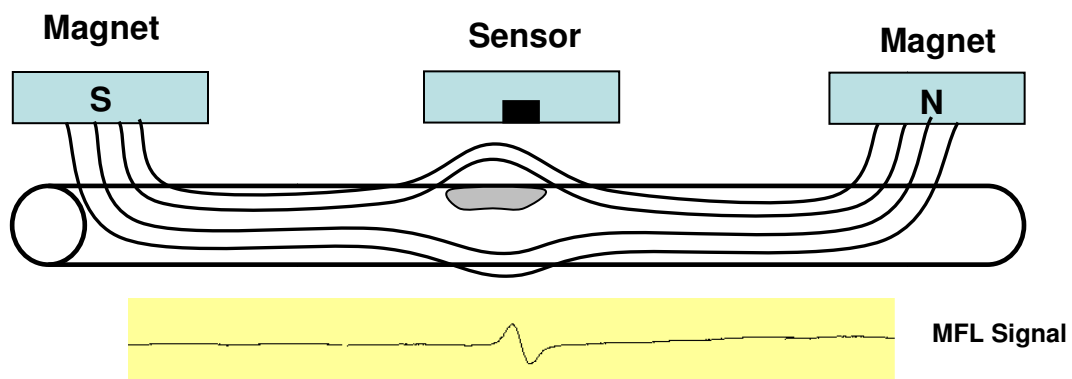
Figure 3.6 Demonstrating MFL concept with a flaw in a steel bar

The flux leakage is dependent on the size of the flaw, the strength of the magnetic field and the distance between the test subject and the magnetic field source and the sensor. The stronger the magnetic field, the more the leakage of the flux lines. Similarly, the larger the flaw is the more leakage of the magnetic field. Figure 3.7 demonstrates the concept of MFL and the effect of the strength of the magnetic field on the amount of flux leakage.

(a)

(b)

(c)
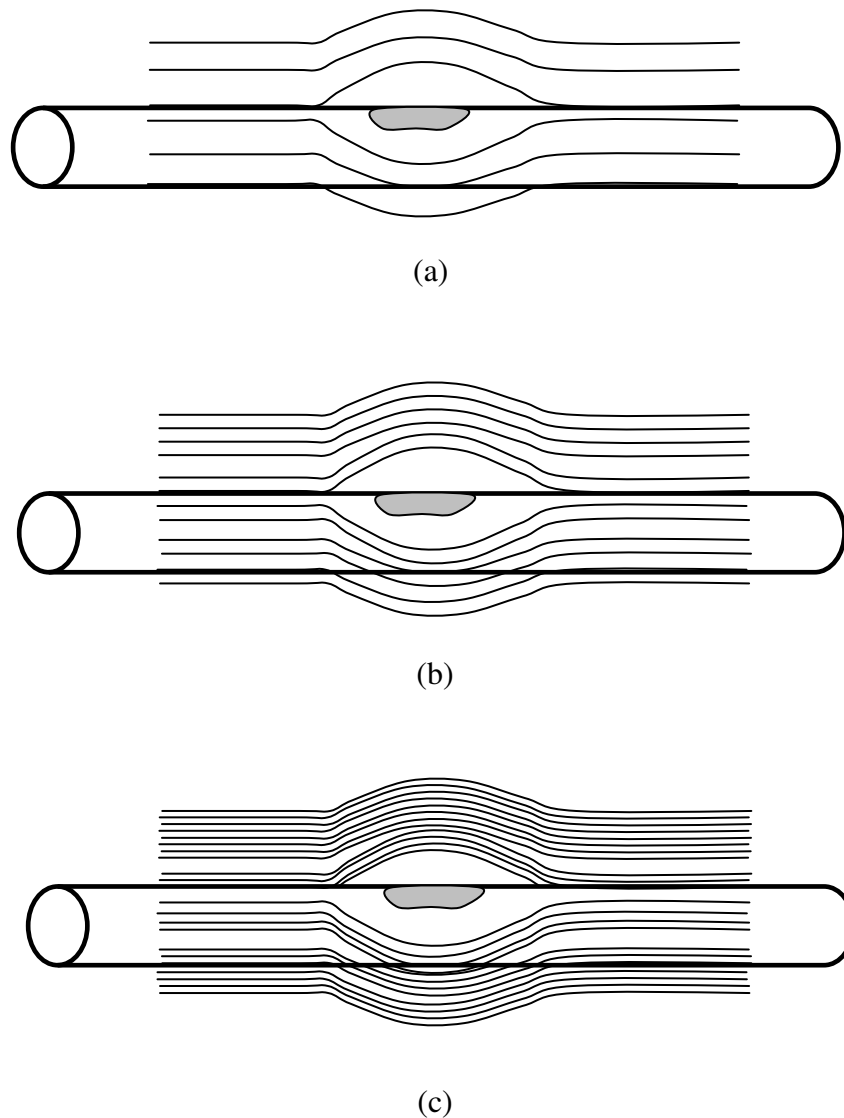
Figure 3.7 Effect of strength of magnetic field on the density of induced flux lines. (a) Low magnetic field, (b) Medium magnetic field and (c) Strong magnetic field

Figure 3.8 shows an example of a typical flaw signature for a cylindrical type flaw, where A and B represent quantitative measures of the peak-to-peak amplitude and width of the flaw.
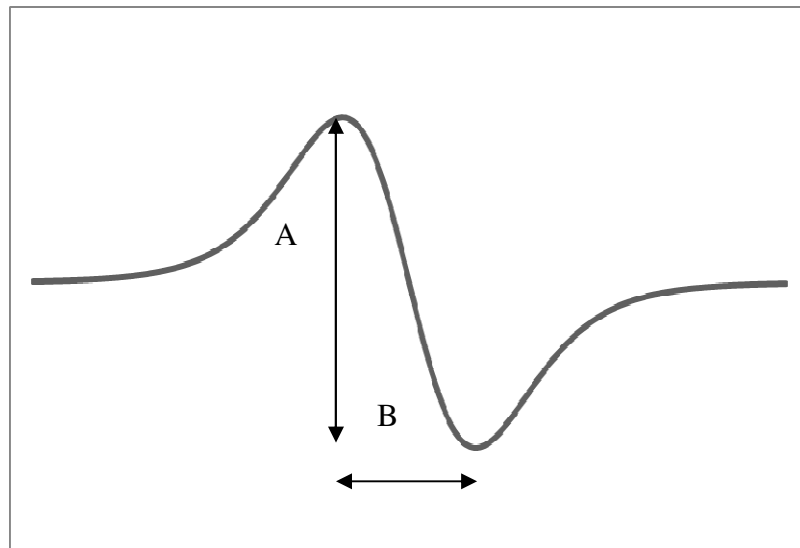
Figure 3.8 Typical MFL flow signal; A is the Peak-to-Peak magnitude and B is the width of the flaw.

3.2.1 MFL Mathematical Models

The MFL technique has been widely used in NDE for detecting metal-loss due to corrosion or fatigue cracking problems in steel structures, particularly for inspecting oil and gas pipe lines. The usage of the MFL technique to inspect gas pipe lines goes back to early 1960's [52-63]. Similar to other NDE techniques, the interest when using the MFL method is to be able to predict the characteristics (size and shape) of the defect by solving the inverse problem of the signal output recorded from MFL sensors. As such, many methods have been attempted to solve the inverse problem solution; these methods can be classified as model or non-model based methods. The model-based methods use a physical model to solve the inverse problem. These methods rely on iterative and optimized loops to find the solution for the inverse problem based an initial guess or prior knowledge of the MFL defect parameters. These methods rely on numerical models [55-57], such as finite element method (FEM), analytical models [58-61] and neural networks [62-64]. Although numerical methods provide an accurate solution for the inverse problem, they are computationally expensive. On the other hand, analytical and neural network methods are less accurate due to the approximation made to drive them, but they are faster methods [71].

The non-model based methods use signal processing techniques to correlate the signal from the MFL sensor to the shape of the defect. For example, the neural network method is used to train the model to predict the shape of the MFL signal based on prior knowledge. However, the model is usually limited to a specific region in the defect and is difficult to apply to an arbitrary shape defect [71]. Other methods tried to combine the accuracy of the FEM methods with the efficiency of the analytical methods using space mapping (SM) [65-70]. This method utilizes a prior knowledge and is usually applied for

34

estimating defects with simple geometry such as rectangular or square. However, in recent work [71], edge detection method is used to predict the shape of the flaw from the top, while using SM methods to estimate the depth parameter for an arbitrary defect.

Also, other methods have been proposed for the mathematical models of MFL defects based on the type of defect. Metal loss defects are classified as surface and sub-surface defects. For surface defects, the focus of the work was to develop an analytical model for a slot-type defect. As such, different models have been proposed which include Foster [16] and Zatsepin, and Shcherbinin [18, 19]. For sub-surface defects, the work was focused on two particular types of defects, cylindrical and spherical. The steel used in cable-stayed bridges is a bundle of either straight wires or strands; each strand consisting of a certain number of individual twisted wires, as seen in figures 3.9 and 3.10. Although defects can be of any shape, it is reasonable to consider fractured wires as a target defect for our work following the same approach and consideration for similar types of research. As such, a broken wire is best represented by cylindrical sub-surface flaw, as seen in figure 3.10. The mathematical model for a sub-surface cylindrical flaw, seen in figure 3.11, has been developed by Swartzendruber [20] and it is available in the literature. Therefore, a brief description of the model is presented in this section.
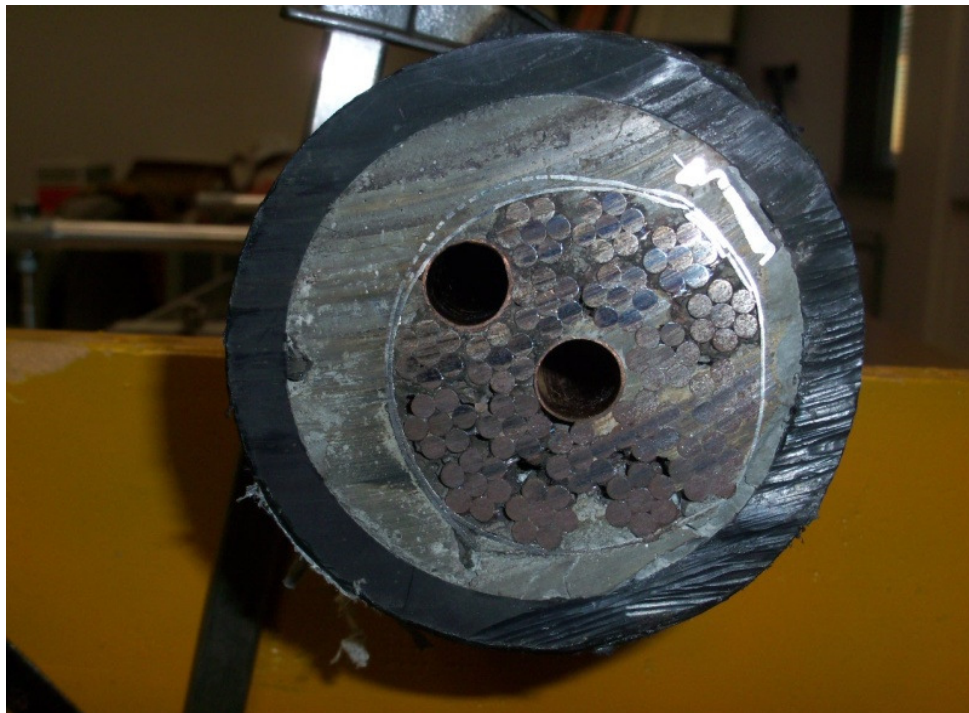
Figure 3.9 Cable showing bundle of steel wires/strands, concrete grout and protective cover

Figure 3.10 Typical steel strands with bundle of wires used in main cables of cable-stayed bridge; Showing man-made defects, from top to bottom, of one broken wire, two broken wires and five broken wires.
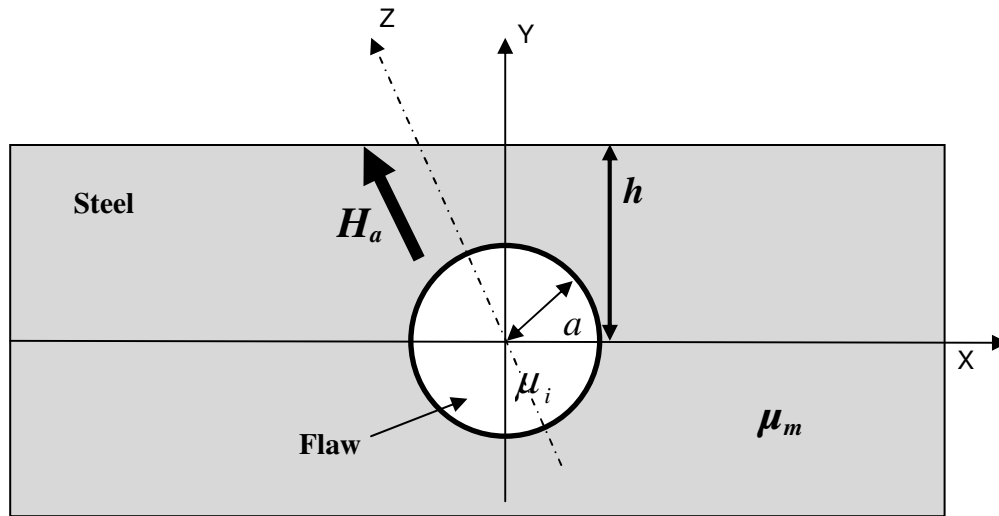
Figure 3.11 MFL Mathematical Model: Illustration of Sub-surface cylindrical flaw

The analytical model for the magnitude of the flux leakage for a sub-surface cylindrical

flaw of a radius *a* and depth *h* can be described with the following equation [20]:

$$m = \frac{2\mu_m}{\mu_m + \mu_i}\left[1 - \left(\frac{\mu_m - \mu_i}{\mu_m + \mu_i}\right)^2\left(\frac{a}{2h}\right)^2\right]^{-1}\frac{\mu_m - \mu_i}{\mu_m + \mu_i}H_a a^2 \qquad (3.1)$$

$$H_y = \frac{2xy}{\left(x^2 + y^2\right)^2}\left(m - 2H_a a^2\right) \qquad (3.2)$$

$$H_x = \frac{\left(x^2 - y^2\right)}{\left(x^2 + y^2\right)^2}\left(m - 2H_a a^2\right) \qquad (3.3)$$

Where,

μ_m : *Permeability of the material under test*

μ_i :   *Permeability of the cylindrical defect*

h :   *Depth of the flaw*

a :   *Radius of the flaw*

H_a :   *The applied magnetic field*

H_x :   *The horizontal component of the magnetic field*

H_y :   *The vertical component of the magnetic field*

The mathematical model shown above represents the flux leakage for a sub-surface cylindrical defect in a two-dimensional form. Figure 3.12 shows a comparison between a real magnetic flux leakage flaw signal from a test and that from the mathematical model of equation (3.2). The figure demonstrates that there is a good agreement between the signals from the real flaw and the mathematical model.
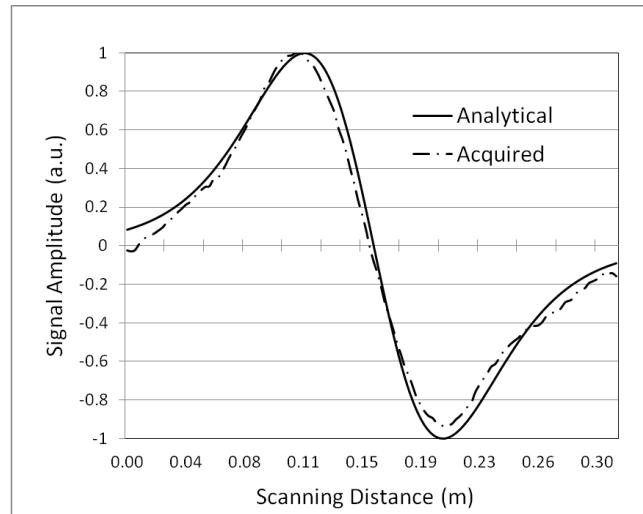
Figure 3.12 Acquired MFL signal and predicated signal based on the mathematical model in equation (3.2).

The mathematical model shown above represents the flux leakage for a sub-surface cylindrical flaw in 2D only and it does not relate to the length of the flaw. An example of a 3D mathematical model for the cylindrical flaw is given in the following equation [11]:

$$Y = \frac{-AX}{(X^2+B^2)^{5/2}} \tag{3.4}$$

Where Y is the signal amplitude as a function of scan position (X), B is the peak-to-peak separation and A is the peak-to-peak signal amplitude. An example of signal from a cylindrical flaw is shown in figure 3.12.

3.3 Magnetostrictive

The Magnetostrictive method works on the concept of applying an external time-varying magnetic field to the surface of a ferromagnetic material (steel cable) for a short period of time to cause small localized physical change. This physical change results in a launch of mechanical waves that travel along the length of the cable. When the waves reach at the end of the cable (anchorage-area) they reflect and travel in the opposite direction. The waves not only reflect from the end of the cable, but they also from the loss of section such as broken wires or corrosion along the wave path in the cable. A transmitting coil, or an electric wire wrapped around the cable, can be used to transmit the initial wave. Similarly, a receiving coil can be used to monitor the reflected waves. The received signal can then be amplified and recorded on a personal computer.

As stated in the previous section, if a ferromagnetic material is exposed to an external static magnetic field, the dipoles in the material will align themselves in the direction of the magnetic field. However, if the same material is exposed to a time-varying magnetic field, the magnetic field produces a time varying current (Eddy currents) through magnetic induction at the surface of the material. The interaction between the Eddy currents and the static magnetic field produces a force whose magnitude is proportional to the Eddy currents and the magnetic field applied. The direction of this force is orthogonal to the direction of the current and the magnetic field. The force is usually referred to as "Lorentz Force" and is identified by the following equation:

$$F = J \times H = a_n \left(|J||H|sin(\theta_{JH}) \right)$$

(3.5)

Where:

F = Lorentz force

H= magnetic field

J= induced Eddy current

a_n= *a vector that points in a direction that is perpendicular to H & J*

θ= *the angle between H & J*

The force works on the lattice structure of the ferromagnetic material, causing a very small localized disturbance (strain). This strain acts as a source to generate waves that travel in all directions through the material and can be related to the applied stress based on the following equation [79]:

$$\rho \frac{\partial^2 u}{\partial t^2} = \frac{\partial \sigma}{\partial y} \tag{3.6}$$

Where,

u = displacement,

ρ = density,

σ = stress

The equations that relate stress to strain are as follows [79, 80]:

$$H = \frac{1}{\mu_r} B - 4\pi\lambda \frac{\partial u}{\partial y} \tag{3.7}$$

$$\sigma = E_a \frac{\partial u}{\partial y} - \lambda B \tag{3.8}$$

Where,

H= magnetic field

B= magnetic flux

λ = magnetostrictive constant,

E_a *= Young's modulus at constant flux,*

∂u /∂y = strain

$μ_r$ *= relative permeability*

H, B, λ, E_a , and $μ_r$ are known quantities and the goal is to find *u.* substituting *B* from

(3.7) into (3.8):

$$\sigma = (E_a - 4\pi\lambda^2\mu_r)\frac{\partial u}{\partial y} - \lambda\mu_r H \tag{3.9}$$

$4\pi\lambda^2\mu_r << E_a$, hence,

$$\sigma = E_a\frac{\partial u}{\partial y} - \lambda\mu_r H \tag{3.10}$$

Differentiate and substitute (3.10) into (3.6):

$$\frac{\partial^2 u}{\partial y^2} - \frac{1}{c^2}\frac{\partial^2 u}{\partial t^2} = \frac{\mu_r\lambda}{E}\frac{\partial H}{\partial y} \tag{3.11}$$

Where c = √ (E/ρ), is the velocity of the wave in the medium.

Depending on the direction of the Eddy currents and the direction of the static magnetic field, different types of waves can be generated; Longitudinal, Transverse (Shear), Rayleigh and Lamb waves. Figure 3.13 demonstrates the concept of magnetostriction to generate longitudinal waves and Figure 3.14 shows how transverse waves are generated. In this illustration, a steel plate is exposed to an external static magnetic field *H*. This could simply be a permanent magnet. The plate is also exposed to a nearby electrical conductor that is carrying a time varying current *I* that generates a time-varying magnetic field surrounding the conductor. An image of the current *I* is created at the surface of the

steel plate, current *J*, due to magnetic induction between the electrical conductor and the steel plate, which is an electrical conductor too.
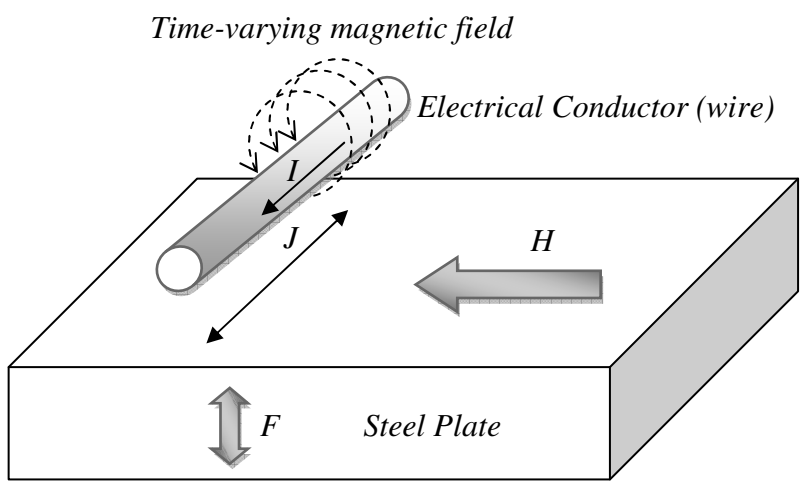
Figure 3.13 Illustration of generating longitudinal waves using Magnetostriction; Steel plate is exposed to a static magnetic field H whose direction is at right angle with Eddy currents flowing at the surface of the plate. The result is a force that is orthogonal to the magnetic field and Eddy currents
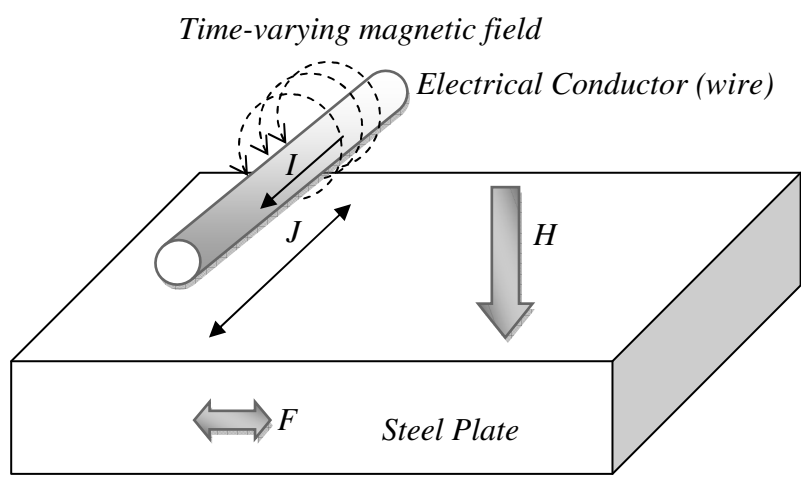
Figure 3.14 Illustration of generating transverse waves using Magnetostriction. Steel plate is exposed to a static magnetic field H whose direction is at right angle with Eddy currents flowing at the surface of the plate. The result is a force that is orthogonal to the magnetic field and the current that generates a transverse wave.

The current *J* and the magnetic field *H* interacts at the surface of the plate and the result is a force *F* that generates a longitudinal, or a transverse wave, depending on the angle between the current *J* and magnetic field *H*. The results of the force *F* is waves that travel within the material. By definition a wave is "a disturbance of a medium from a natural or equilibrium condition that propagates without the transport of matter" [9]. One may think of this as waves travelling through a solid bar, energy from the wave travel through the bar, but the particles of the bar do not travel through the material. Waves travel in nature through all kinds of media; solid, gas, liquids (wood, steel, water, oil, concrete and, of course, air). The manner in which the waves travel (propagate) through the material depends on the material's characteristics and its responses to particular wave functions.

Waves are generally classified based on characteristics such as frequency, magnitude, wave-number, phase velocity and group velocity.

Wave-number:

The wave-number is a real number and it is inversely proportional to the wave length given by:

$$\zeta = \frac{2\pi}{\lambda} \tag{3.12}$$

Where, ζ is the wave-number in radians per meter, and λ is the wave length in feet

Phase velocity:

Phase velocity is the speed at which individual wave crests travel and is given by

$$v_{ph} = \frac{\zeta}{\omega}$$

(3.13)

Where, v_{ph} is the phase velocity in feet per second, and

ω is the circular frequency in radians per feet

Group velocity:

Group velocity defines how fast the material particles are moving and is given by

$$v_{gr} = \frac{\partial \omega}{\partial \zeta}$$

(3.14)

Where, v_{gr} is the group velocity in feet per second,

ω is the circular frequency in radians per feet.

Almost all waves propagate in one of the following methods; longitudinal, transverse (Shear), Rayleigh and Lamb waves.

Longitudinal wave:

Longitudinal wave is a wave in which the particles of the material vibrate in parallel to the direction of the propagation. The longitudinal wave is also called pressure wave or P-wave, because of the compression and tension of the particles that are along the direction of the propagation. Longitudinal wave's propagation is illustrated in Figure 3.15.

Transverse wave:

Transverse wave is a wave in which the particles of the material vibrate perpendicular to the direction of wave propagation. Because the transverse particles' motion has an

associated shear stress, the transverse waves are often called shear waves. Transverse waves propagation is illustrated in Figure 3.16.

Rayleigh wave:

Rayleigh wave is a wave in which the particles of the material vibrate in directions, perpendicular and parallel, to the direction of propagation. They are commonly found in thick plates, where they penetrate to one wave length depth in the material. Rayleigh waves are illustrated in Figure 3.17.

Lamb wave:

Lamb waves are similar to Rayleigh waves, except they propagate in thin plates, where the thickness of the plate is a few wavelengths. Although the particles motions' is possible in multi modes, the most common modes are symmetrical and asymmetrical. Symmetrical lamb waves mode moves in symmetry about the medium of the plate. The propagation mode is also called extensional mode because the plate is stretched and compressed in the wave direction. The asymmetrical lamb wave mode is also called flexural mode because majority of the particles movement is normal to the surface of the plate; the two surface of the plate move on the same direction. Lamb waves are illustrated in Figure 3.18.

Direction of propagation ⟶

Particles motion direction
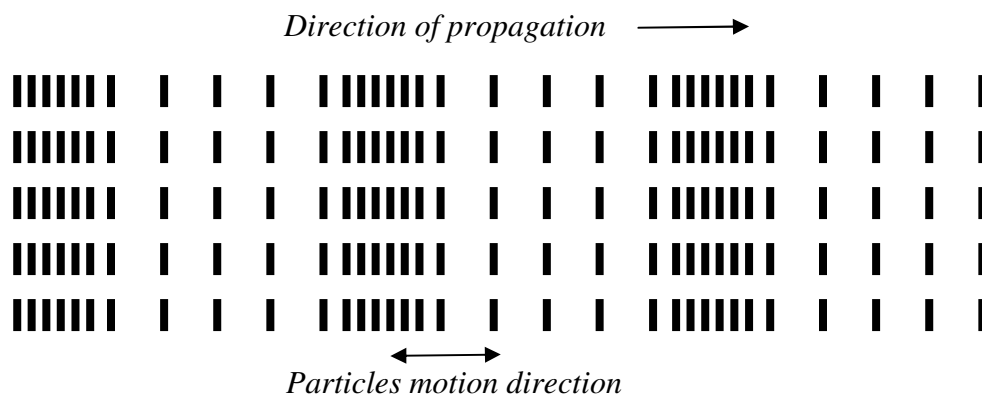
Figure 3.15 Illustration of longitudinal waves; particles of the material are moving in parallel to the direction of propagation.

Direction of propagation ⟶

Particles motion direction
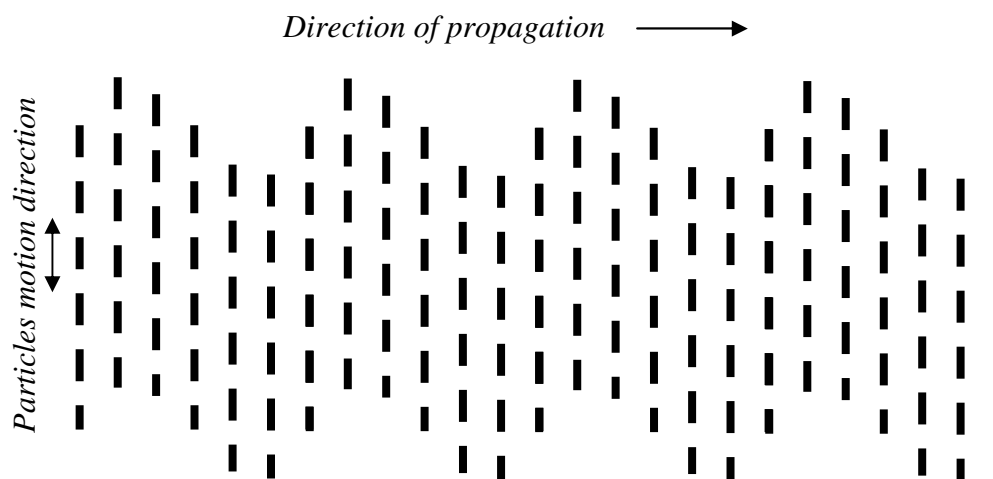
Figure 3.16 Illustration of transverse waves; particles of the material are moving perpendicular to the direction of propagation.

Direction of propagation
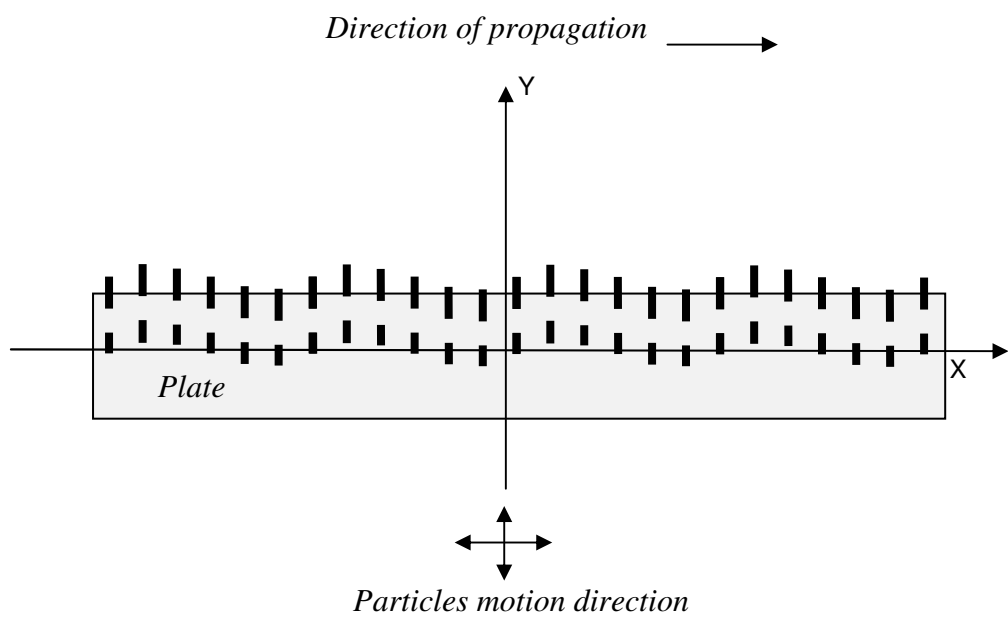
Figure 3.17 Illustration of Rayleigh waves; particles of the material are moving
perpendicular and parallel to the direction of propagation.

(a) Asymmetric waves
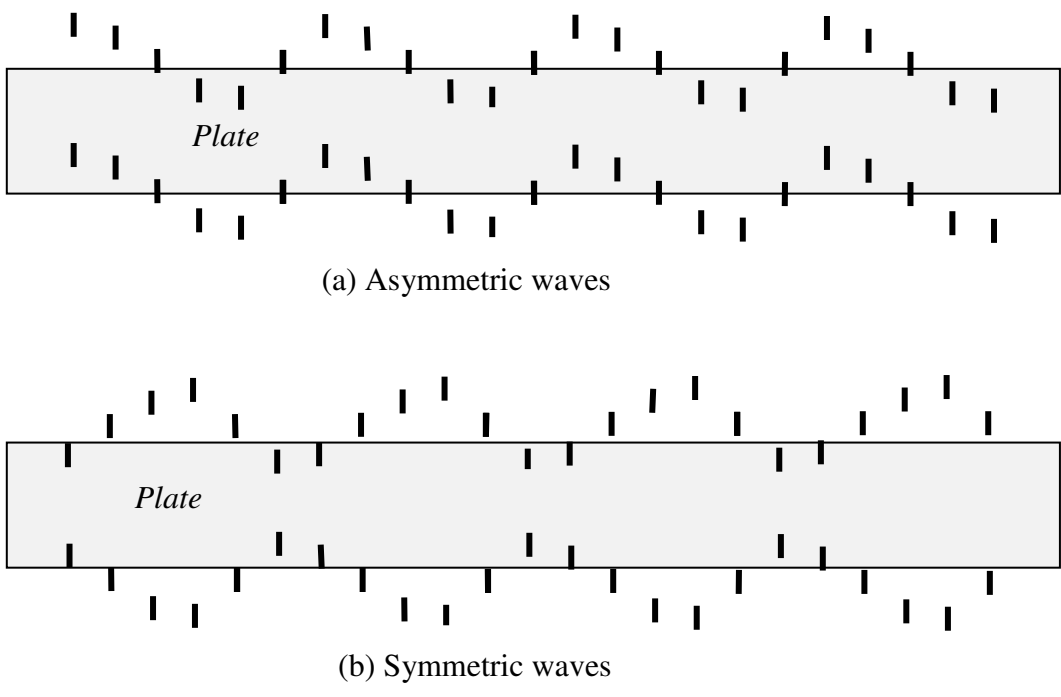
(b) Symmetric waves

Figure 3.18 Illustration of Lamb waves; (a) asymmetric waves; (b) symmetric waves.

3.3.1 Magnetostrictive Mathematical Models

The study and mathematical modeling of the longitudinal guided waves have been reported extensively in the literature [77-83]. Only the governing equations are presented here. Illustration of the mathematical model is shown in Figure 3.19 [81]. The transmitted and received longitudinal waves can be expressed in the following equations [81]:

$$v_t = k_1 \int_0^{\tau_1} \Phi' \left(t - \frac{d}{V_o} - \tau \right) d\tau \qquad (3.15)$$

$$v_i = k_2 \frac{d}{dt} \left[\int_0^{\tau_1} v_t (t - \tau) d\tau \right] \qquad (3.16)$$

Where,

$$\tau = \frac{x}{V_o}, \quad \tau_1 = \frac{l_1}{V_o}$$

x =displacement reference point in ft

V_o = *velocity of the wave in ft/sec*

l_1 = *the length of the cable under the transmit/receive coil*

k_1, k_2 = *constants*

d = travel distance on the cable in (ft) from reference point

v_t = *velocity function of transmitted wave in ft/sec*

$v_{i\,=}$ *induced voltage function at receiver coil in volt*

φ = *magnetic flux function Weber/ft*
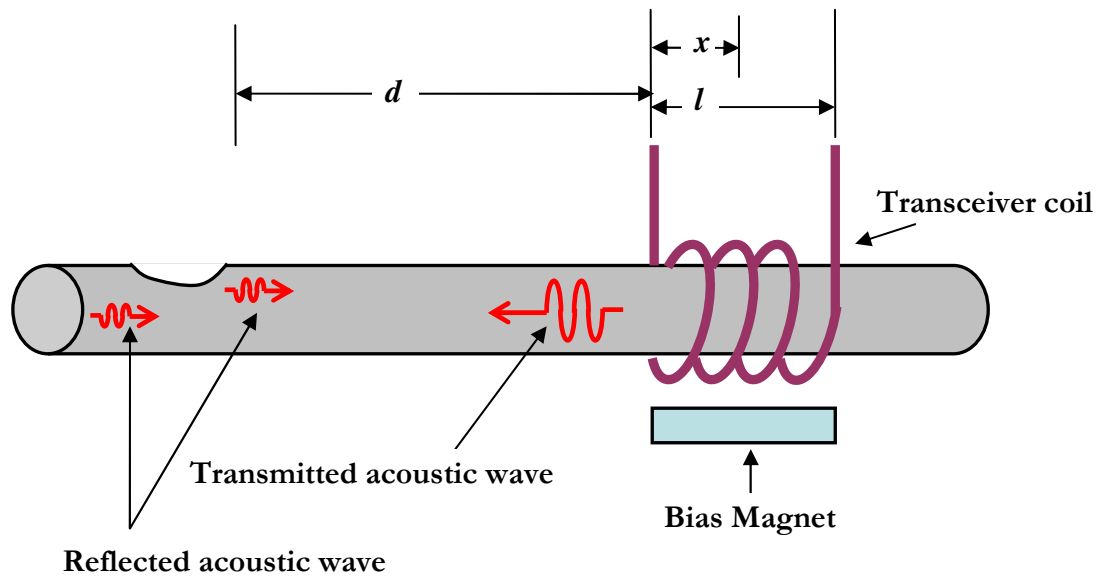
Figure 3.19 MS Mathematical Model: Transceiver coils is wrapped around one end of the cable, *x* is a reference point, *l* is the length of cable under the coil and *d* is traveling distance.

Equation (3.15) describes the velocity function/displacement in the bar at location *d* and

time *t* due to the magnetostrictive effect. Equation (3.16) describes the induced voltage at

the transceiver coil due to the inverse magnetostrictive effect.

Figure 3.20 shows a comparison between a real MS flaw signal from a test and that from the mathematical model of equation (3.15) and (3.16). The figure demonstrates that there is a good agreement between the signal from the real flaw and the mathematical model.
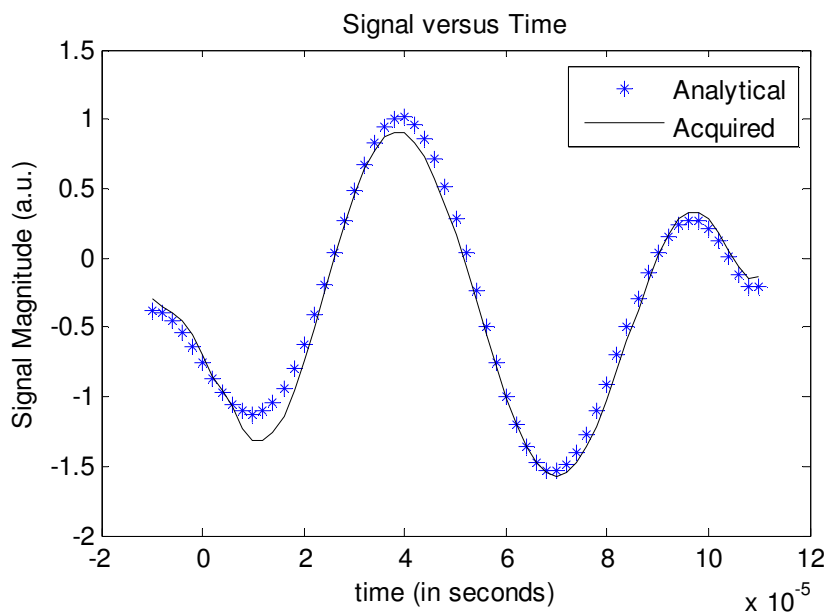
Figure 3.20 Acquired MS signal and predicated signal based on the mathematical model in equation (3.15) and (3.16).

3.3.2 Application of Magnetostrictive to Cable Inspection

The principle of using the MS concept to inspect cables in bridges is to transmit a traveling wave along the length of the cable and monitor the reflected waves. This can be accomplished by creating a localized disturbance in the steel cable using a time-varying magnetic pulse. The magnetic pulse causes a very small change in the physical dimensions of the steel cable; in the order of few parts per million. As a result, guided waves are generated inside the cable, where they propagate along the length of the cable. For the most part, the reflected waves are resulted from discontinuities in the steel cable or the ends of the cable. The reflected waves cause reverse localized disturbances to the magnetic field. These disturbances can then be detected by means of using a coil or magnetic sensors. Combining a permanent magnet and wrapping an external coil at one end of the steel cable and coupling an RF pulse can accomplish this. The various reflected waves from the steel cable can then be analyzed to evaluate the steel condition in the inaccessible areas such as the anchorage zones of cable-supported bridges. Figure 3.21 shows a conceptual design for the MS system.
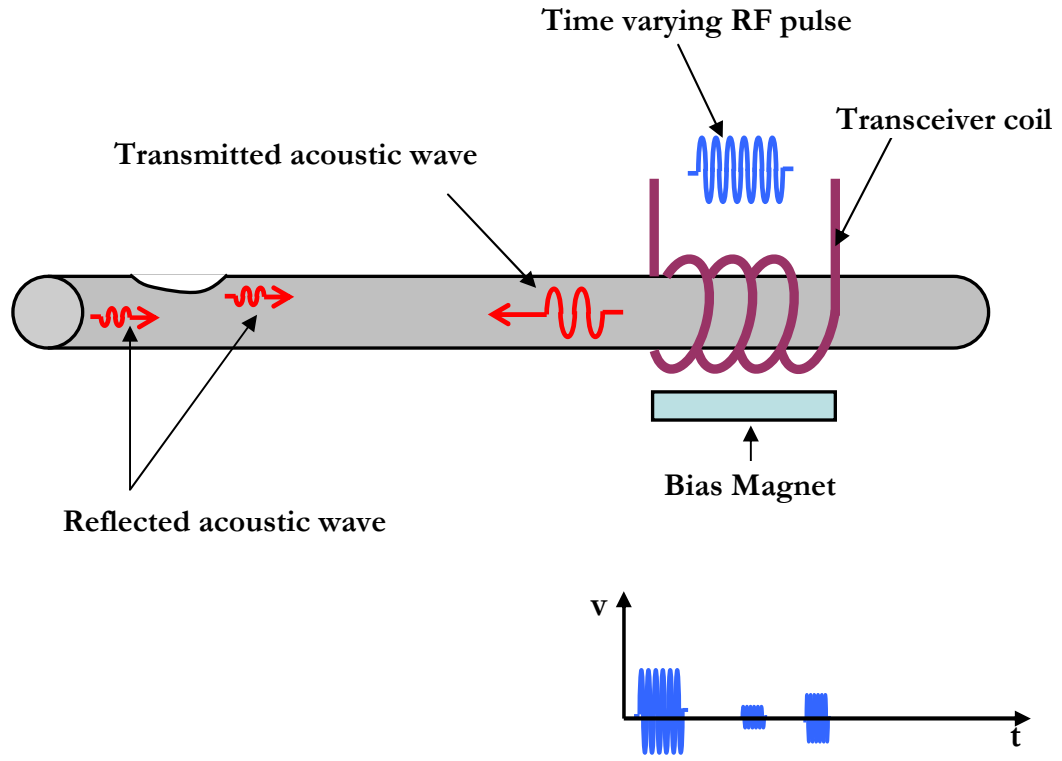
Figure 3.21 Magnetostrictive method: Demonstration of the MS method, showing a RF coil wrapped around the cable and energized by a RF pulse to produce guided waves.

The bias magnet is used to effectively couple the electrical/magnetic pulse to an acoustic wave. The transceiver coil is used as a transmitter to send the magnetic pulse and also as a receiver to receive reflected waves. The MS method will enable us to inspect the inaccessible areas of the cable (i.e., the anchorage area) as seen in figure 3.22
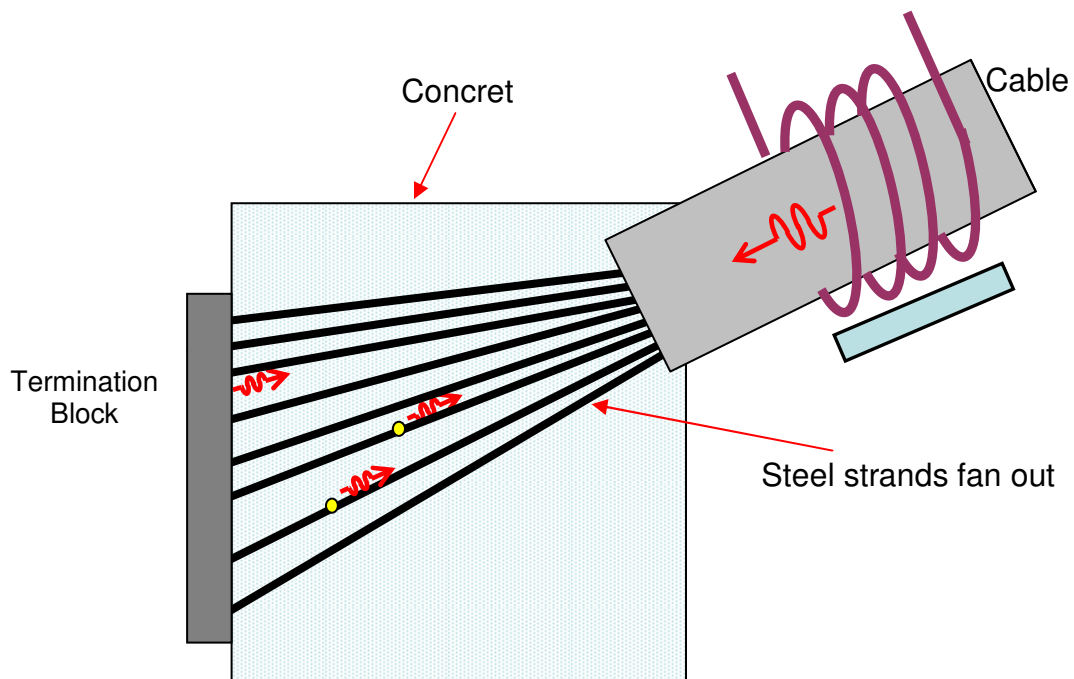
Figure 3.22 Demonstration of the use of the MS method for inspecting cable in the anchorage area

The steel strands in the cable within the anchorage area are usually fanned out into individual strands, where they are anchored by a steel termination plate at the end. The strands inside the anchorage area are typically inaccessible and are covered by concrete. This research has investigated the introduction of the MS method at the exposed end of the cable and near the face of the concrete anchorage block to inspect the condition of the cable inside the anchorage zone. In this configuration, the guided wave will travel through the cable and individual strands. It is expected that the guided waves reflect back from the end of the strands as well as from any defects in the strands. The reflected waves can be captured with a receiver coil, where they are converted to electrical signals. The time-domain signals can then be analyzed to distinguish the presence of defects from

reflections from within the anchorage-area. Since the length of the cable inside the anchorage-area and the speed of wave propagation in steel (16,978.3 ft/sec) are generally known [24], one can calculate the location of any defects by observing the traveling times from the reflected signals. A typical range of the frequency for the RF pulses used in steel inspection is between 8 and 85 KHz [23, 24], with an RF pulse current of up to 41A [24]. As such, we expect a significant amount of current and a near saturation magnetic field to produce an acoustic wave with sufficient energy to travel along the cable strands. However, the key advantage of using the MS concept is that it provides a non-contact, direct coupling of energy to the steel to reduce signal losses due to boundary conditions. A simplified acoustic interface for the cable is shown in Figure 3.23. The amount of reflection can be calculated using the equations 2.3, 2.4 and 2.5 presented in Chapter 2. By considering the acoustic impedances of the steel and concrete from Table 2.1, one can calculate the expected reflection at the steel-concrete interface to be about 74%, assuming 90° incident waves. The equation describing the decay of the wave is given in Equation 2.2 and it is repeated here for convenience:

$$I = I_0 e^{-\alpha x} \tag{3.17}$$

Where,

I : *Intensity of the beam exiting the material*

I_0 : *Intensity of the beam entering the material*

α : *Attenuation coefficient*

x : *Thickness of the material*
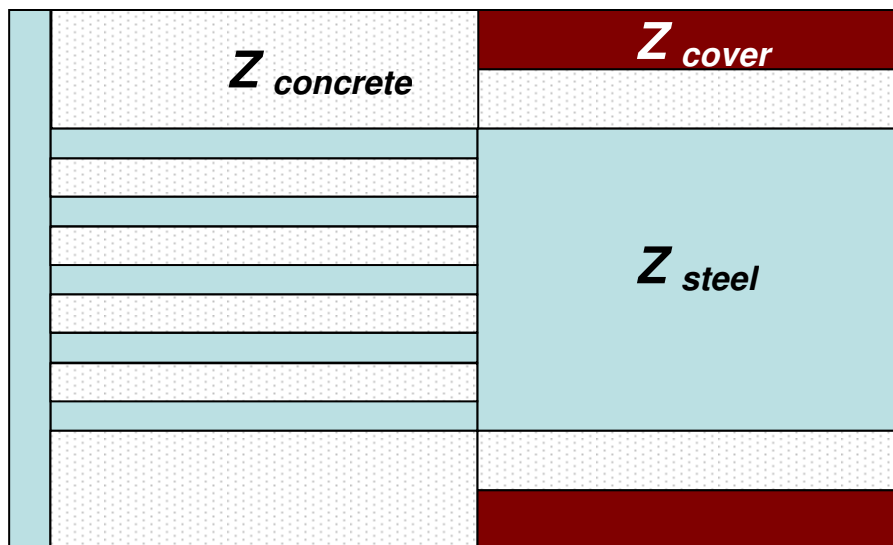
Figure 3.23 Simplified diagram for equivalent cable material acoustic interfaces, showing cable wires fanning-out and terminated at a steel plate. Z is the acoustic impedance of the material.

CHAPTER 4

EXPERIMENTAL PROGRAM

_____

4.1 Introduction

This chapter describes test specimens, instruments and the general experimental setup used in conducting tests to assess the application of MFL and MS methods. The goal of these experiments is to provide an assessment of feasibility of using the MFL method for detecting steel defects in cable-bridges. Furthermore, the tests are designed to measure the sensitivity of the MFL to the defects with varying size and location within the cable. A prototype MFL system was built to carry out the experiments. Also, several steel specimens were used with fabricated defects to simulate real defects in the field. A test cable similar to the cables in bridges was also built to aid the evaluation. Similarly, several laboratory setups and experiments were carried out to assess the feasibility of using the MS method for detecting defects in the cable within the anchorage area. The effect of defect size and the ability of the MS to detect defects with varying sizes were also evaluated. Section 4.2 describes the details of the prototype MFL system, while section 4.3 details the MFL experiments. The prototype MS system setup is discussed in section 4.4. Section 4.5 provides the details of the MS experiments carried out on multiple steel specimens.

4.2 MFL System Prototype

The MFL system developed consists of two strong permanent magnets as shown in figure 4.1. Each magnet is polarized perpendicular to its surface and the flux lines travel from the north-pole surface of the first magnet to the south-pole surface of the second magnet. The pair of magnets is polarized opposite each other to allow the flux lines to travel from one magnet to the other, creating a uniform magnetic field between the two magnets. Each magnet block is 8 in long by 4 in wide by 2 in thick.
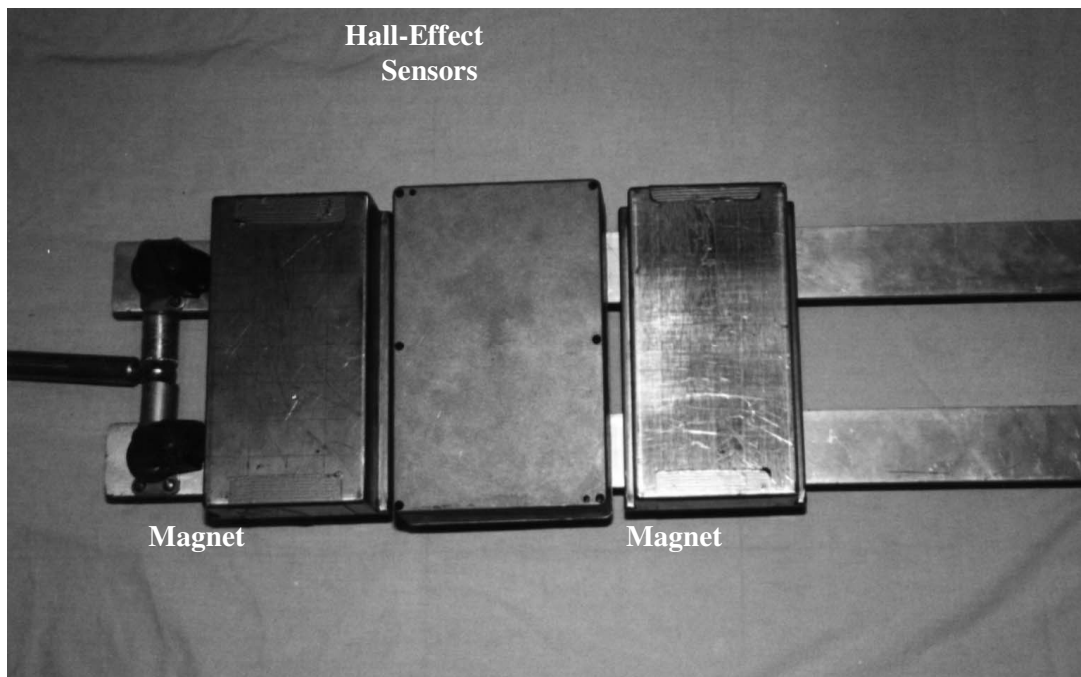
Figure 4.1 The MFL system with two permanent magnets and a sensor enclosure
in the middle [46, 48].

Each magnet's dimensions and layout have been optimized to provide a uniform magnetic field and maximum field penetration (2-3 in from the surface of the cable) within the desired limits of detection for loss of section in bridge cables.

A Hall-effect sensor enclosure that includes an array of ten Hall-effect sensors and a series of signal amplifiers has been placed between the two magnets. The Hall-effect sensors are placed at the isocenter of the two magnets to assure symmetry for the resulted MFL flaw signals. The Hall-effect sensors used in this MFL system are surface sensors and arranged to capture only the vertical component of the magnetic field leakage. The Hall-effect sensors are arranged in two layers; the near field layer that consists of seven sensors, and the far field layer (placed at 1 in from the near field sensors) that consists of three sensors. The lateral distance between each two adjacent sensors is kept at 1 in. The arrangement of the two layers of sensors allows for additional signal processing to recognize and eliminate non-defect artifacts.

The entire magnet and sensor assembly is mounted on an aluminum frame with wheels to allow moving the magnet on the surface of the cable. An encoder device is attached to one end of the frame to allow tracking of the position of the scan and subsequently it is used to identify the location of defects. The output of the sensors is connected to a data acquisition device. The data from sensors is collected and displayed in real time on a laptop computer using the LabVIEW software from the National Instrument Company (NI). The software has been designed to allow continuous display of data from all 10 sensors simultaneously or from selected sensors only. Further post processing software application has been created to allow for data analysis.

4.3 MFL Laboratory Experiments

To demonstrate the capabilities and effectiveness of the MFL system, several laboratory experiments were conducted. A 4.5 in diameter bridge cable of 8 ft long which is similar to the commonly used bridge cables was used in the laboratory. The bridge cable consists of a bundle of 19 strands, as seen in Figure 4.2 below.
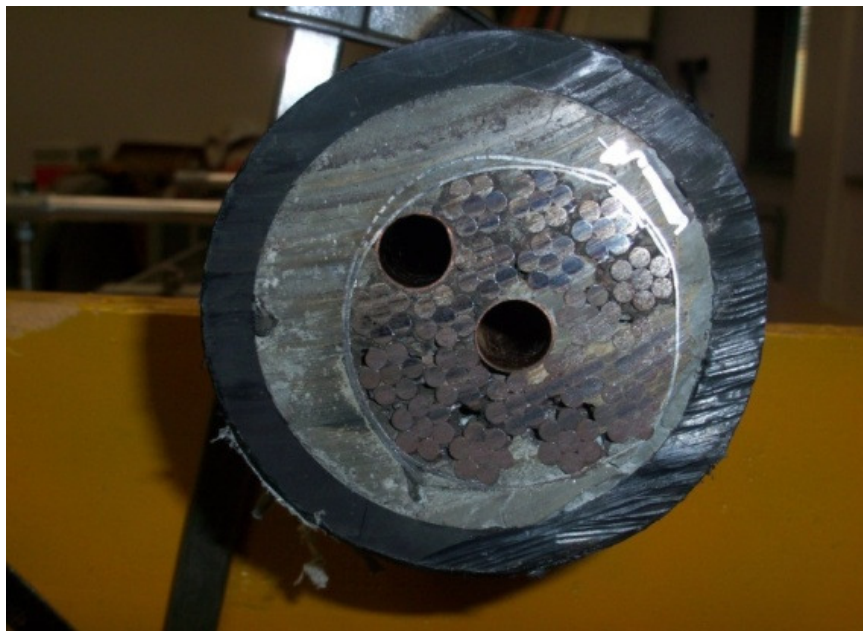
Figure 4.2 Bridge cable showing a bundle of prestressing steel strands covered with concrete grout and protective HDE cover.

Two strands, one at the edge and one at the center of the strand bundle, were replaced by two copper tubes to allow insertion of strands with pre-set flaws in the laboratory bridge cable. Several defect sizes, from a single wire fracture to a complete strand fracture, were fabricated in the inserted strands.

The experiments were carried out by scanning the surface of the cable by moving the

magnets-sensors assembly over the entire length of the cable as seen in Figure 4.3. The experiments were repeated for different inserted strands that contained different defects. In each experiment, the data from all the sensors is presented on the computer screen in real time using the system's data acquisition software and stored in a computer for post-processing.
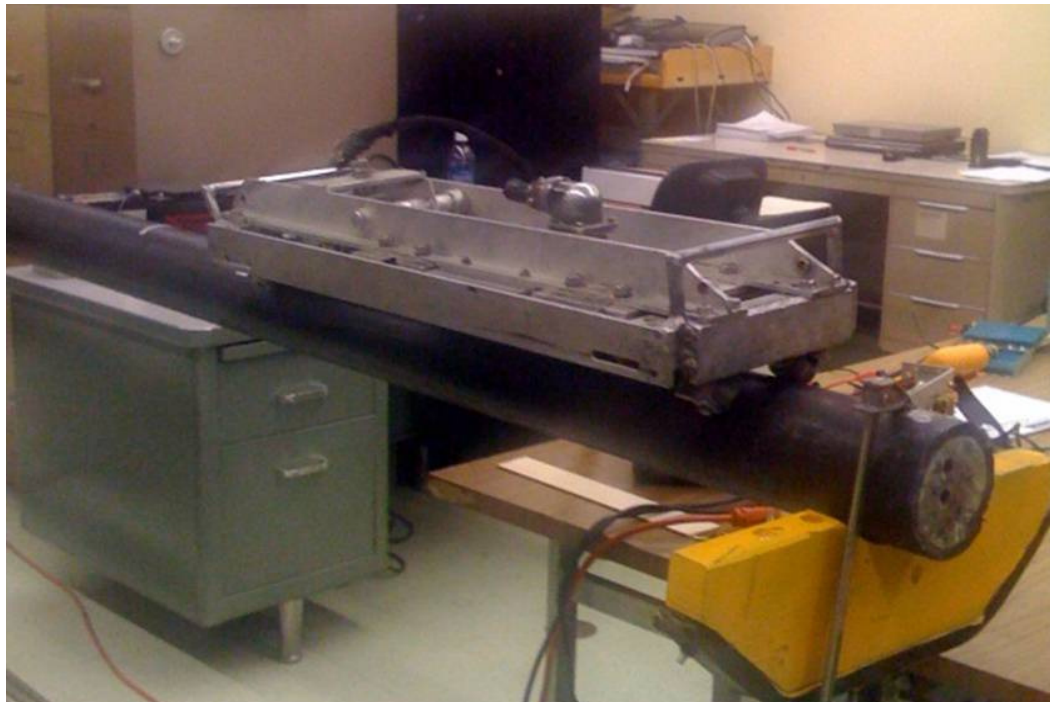
Figure 4.3 MFL system installed on a laboratory bridge cable; showing 19 stands cable, with two stands inserted in the top and center holes in the cable.

To demonstrate the sensitivity of the MFL system to the size of the defect, several experiments were conducted where defect size was varied from a single wire fracture to several broken wires in one strand. Figure 4.4 shows a strand with no defects and additional strands with 1, 2, 3, and 6 broken wires.
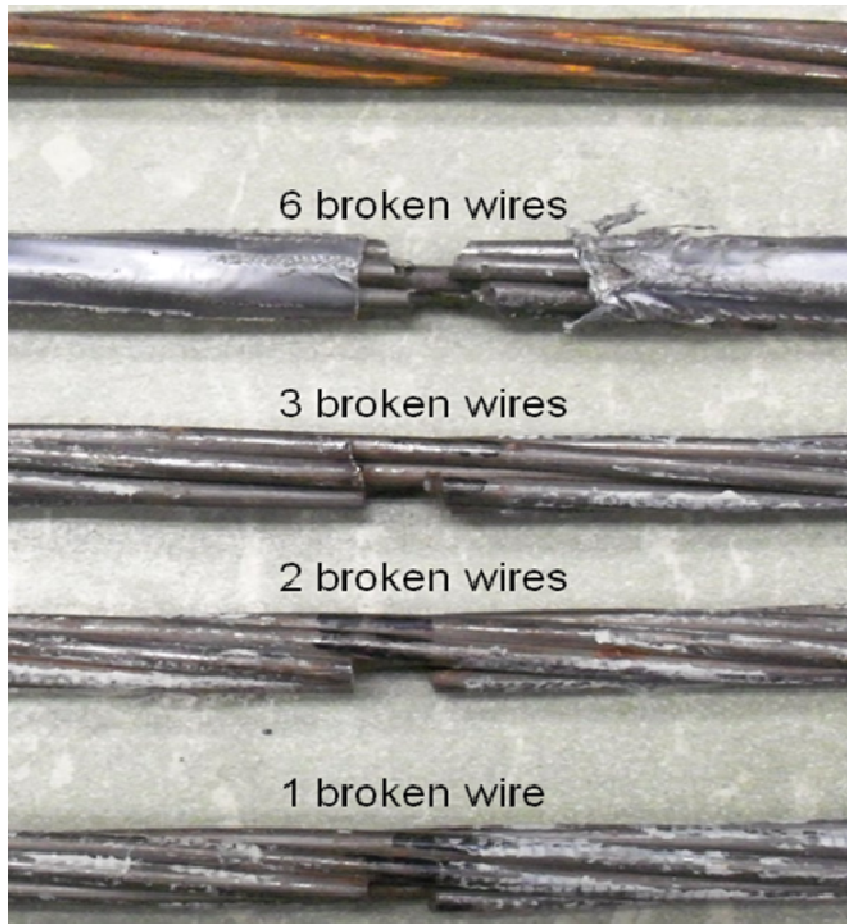
Figure 4.4 Prestressing steel strands with no flaws (top) and with different sizes of flaws.

4.4 MS Laboratory Experiments

The general block diagram for the MS system used in the experiments is shown in figure 4.5. The RF pulse is generated using a tone generator. The frequency of the RF pulse is 7.5 KHz with 220 µsec duration. The RF pulse is fed into an audio power amplifier with 350 watts of power and a frequency range from 400 Hz to 20 KHz. The maximum output current of the power amplifier is about 20A that is connected to the transmitter coil. The transmitter coil consists of a 12-gage wire wound around a steel strand with 40 turns. The coil is placed at the end of the magnet, 12 in away from the receiver coil. The receiving coil is placed at the center of the magnet in the linear region with 160 turns wound around the strand. The output of the receiving coil is connected to an amplifier device (AD620) with a signal gain of 1000 and a signal-to-noise ratio (SNR) of 85 dB. A NI data acquisition card (DAQ6024) and the LabVIEW software were used to acquire and record the data into a PC. The sampling rate used in acquiring the signal is 200 KHz for duration of about 10 seconds. The collected data is then averaged using 10 points averaging filter to improve the SNR. Figure 4.6 shows the hardware components for the MS system experiments.
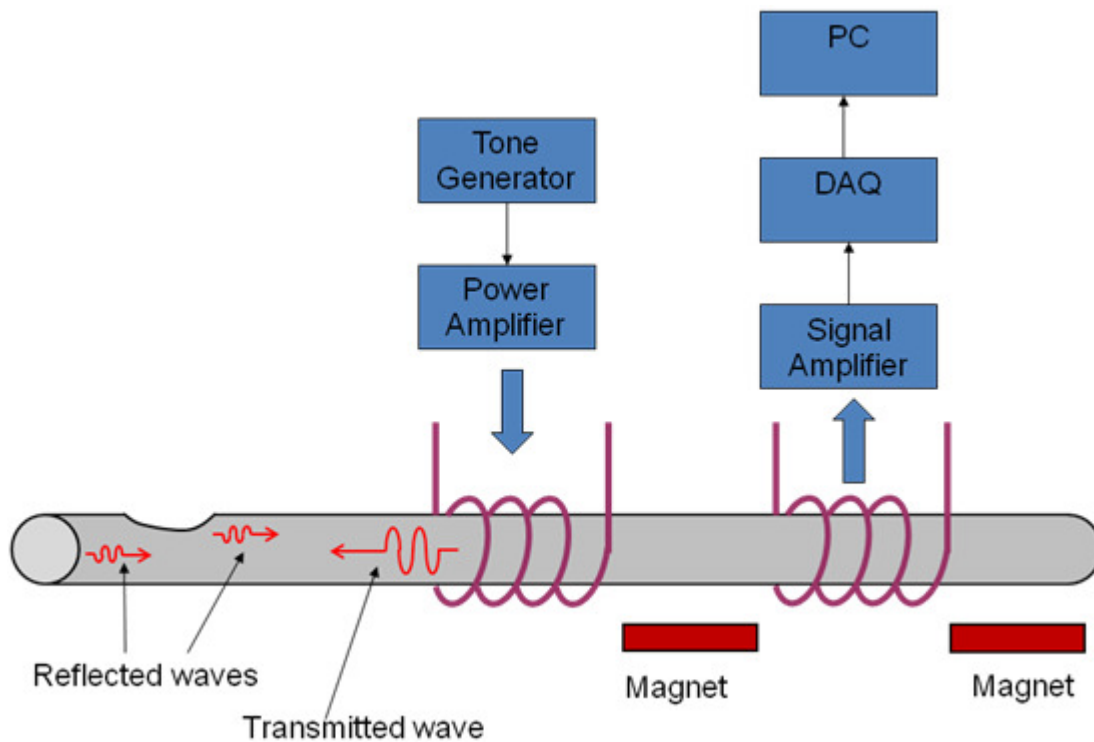
Figure 4.5 Illustration diagram for the MS experimental setup; showing, magnet pair, tone generator, RF receive coil, RF transmit coil, small signal preamplifier, power amplifier, data acquisition interface box and PC.
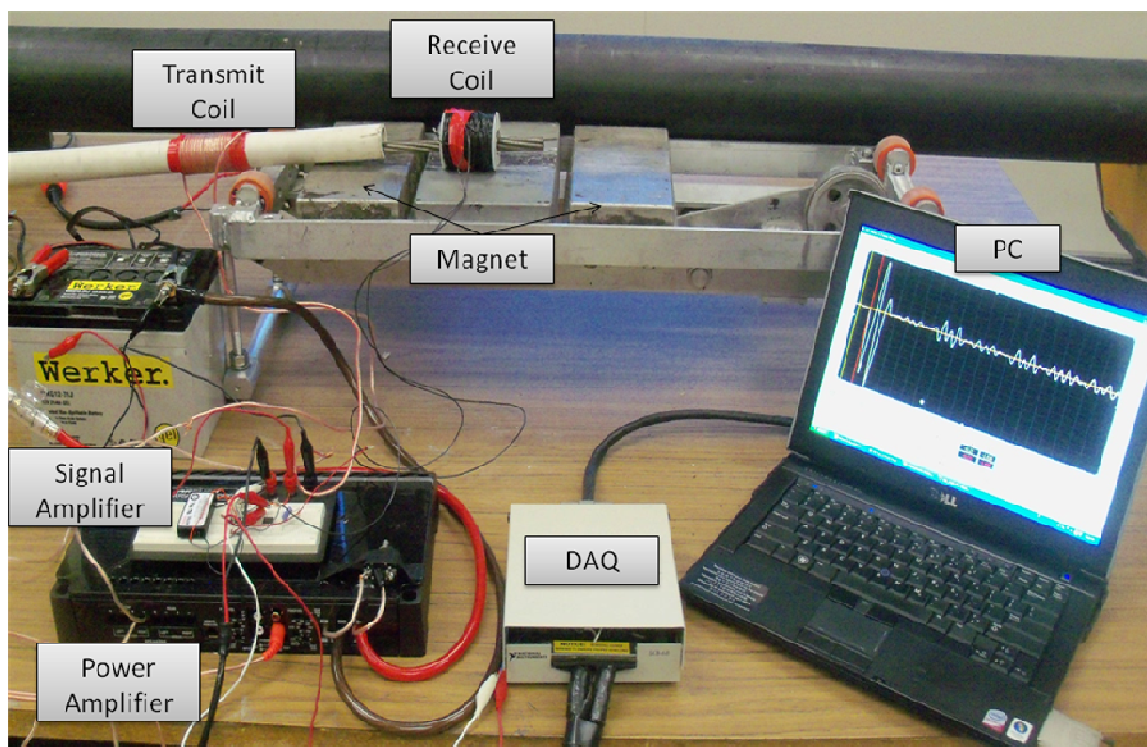
Figure 4.6 MS System Components; including, magnet, RF receive coil, RF transmit coil, small signal preamplifier, power amplifier, data acquisition interface box and PC.

In all of the experiments, the steel strands and the receiver coil were placed parallel to the direction of the magnetic field at the center of the linear region of the magnets. The location of the flaws was kept constant at 63.5 in from the center of the receiving coil in all the experiments. Figures 4.7 and 4.8 show the placement of the strands and flaws within in the laboratory setup.

The experimental setup for the MS tests included two separate setups: single strand setup and a 13 stands cable-anchorage setup. The next section provides more details on each setup.

4.4.1 Single-Strand Experimental Setup

A total of six strands were used in this setup with varying flaw sizes. All of the strands were about 10 ft long. The first strand used in the experiment was without any defects except with small amount of surface rust. This established a baseline measurement for the experiment. The second strand had one broken wire out of the seven wires that make a steel strand, the third strand had two broken wires and the fourth strand had 3 broken wires. The fifth strand had 6 broken wires. The sixth strand had fan-out wires with no flaws to examine the effect of wire fan-out. Figure 4.9 shows the strands and the size of the flaws used in the experiments.
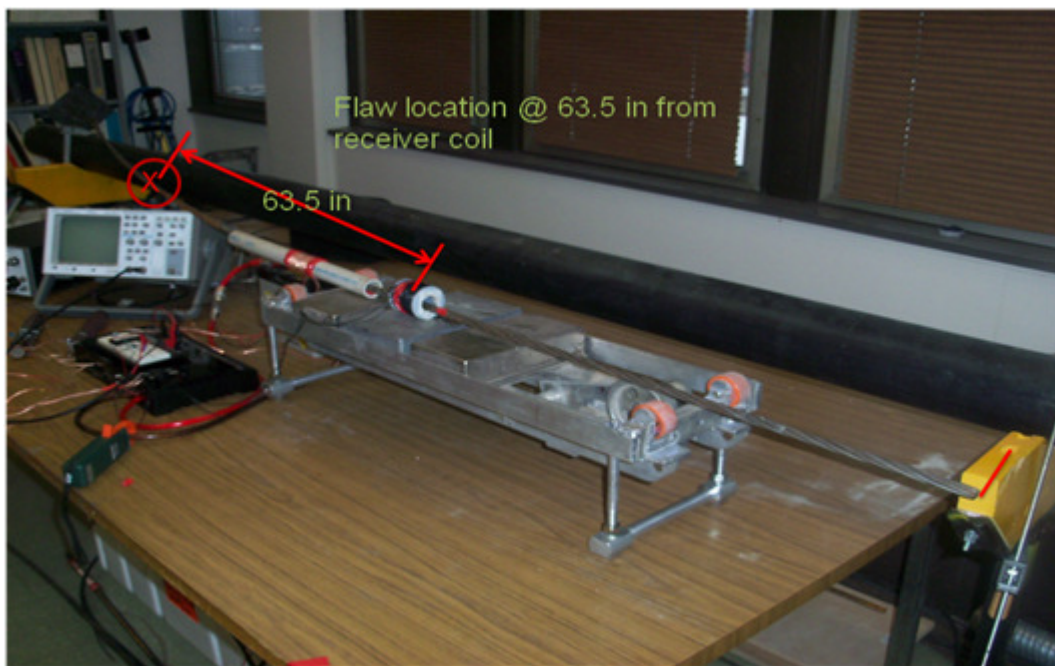
Figure 4.7 Flaw and strand placement for the MS experiments; showing a flaw location at 63.5 in from the of the receiver coil

Flaw location @ 63.5 in from receiver coil
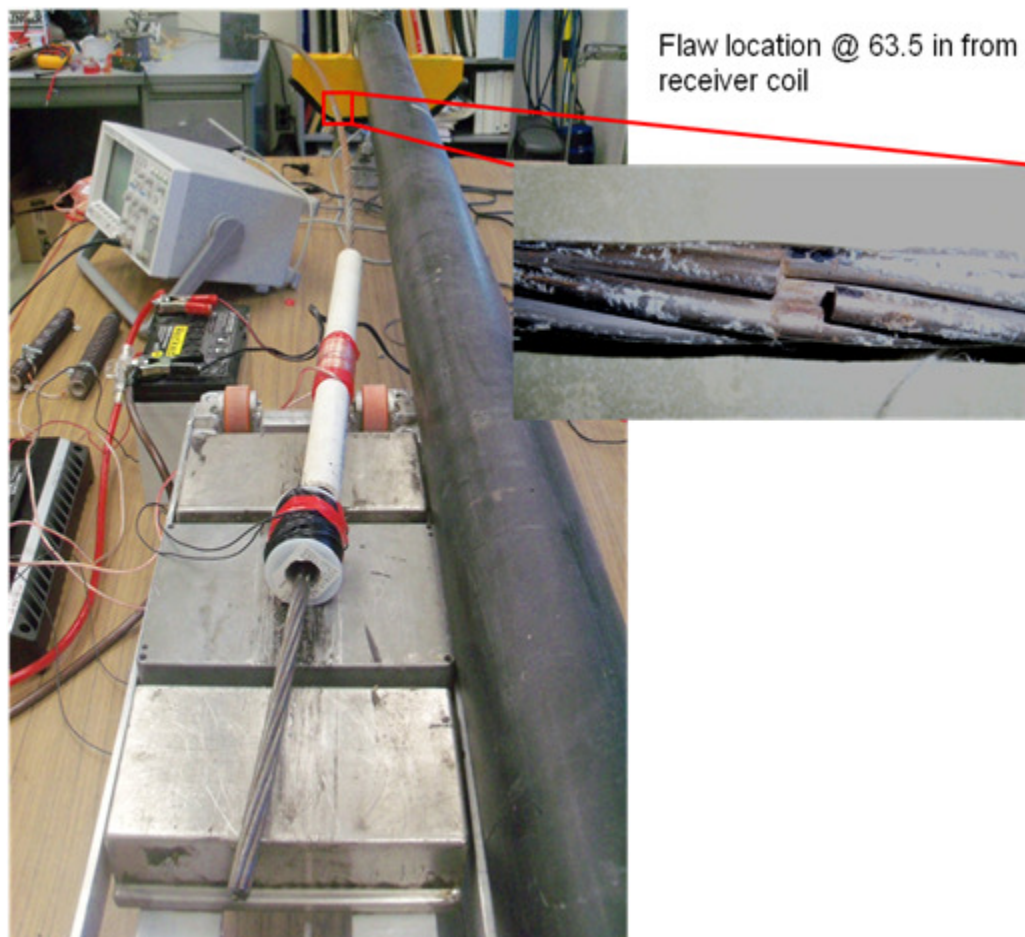
Figure 4.8 Flaw and stand placement for the MS experiments; showing 1 broken wire flaw located at 63.5 in from the receiver coil.
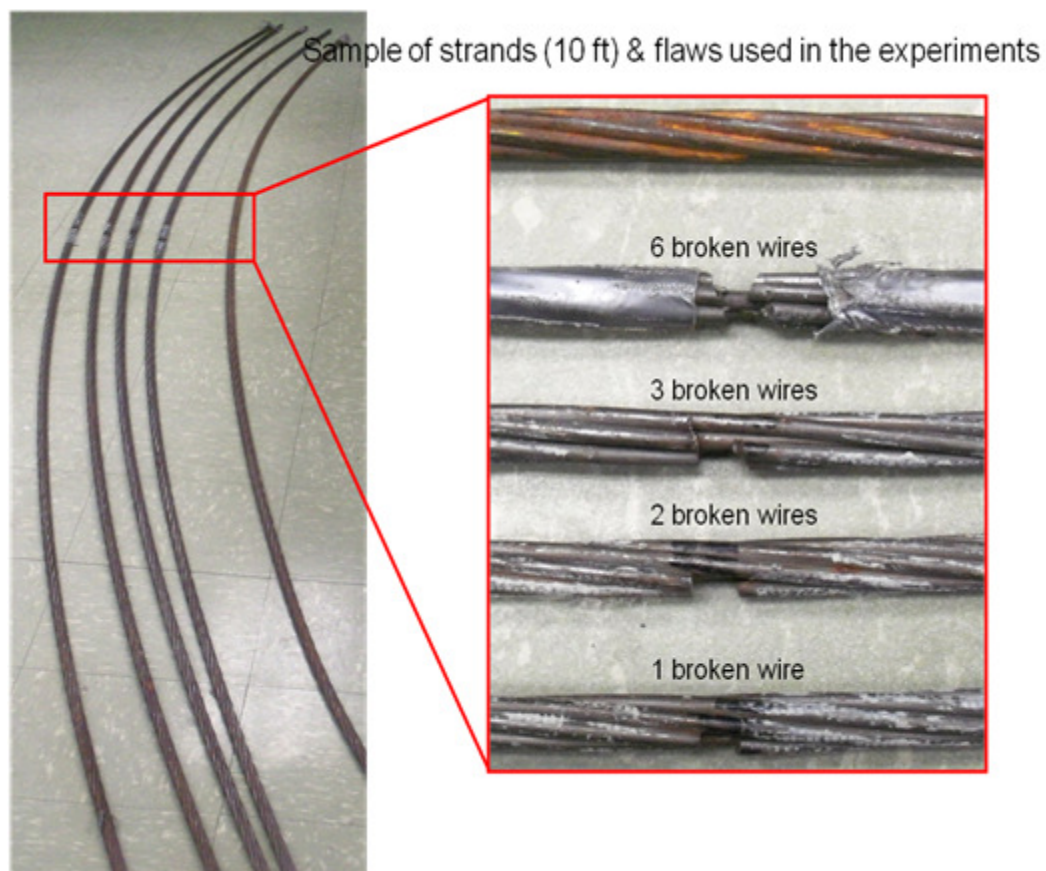
Figure 4.9 Sample of strands and flaws used in the MS experiments

4.4.2 Experiment for Cable Within the Anchorage Area

To assess the performance of the MS method to detecting defects in strands within the cable anchorage zone, a model was built as shown in figure 4.10. The model consists of a bundle of 13 strands; each strand is constructed of 7 wires. All the strands were cut at the same length of 10 ft. The strands were spread out at one end and were terminated with a wooden block. The other end of the bundle was kept together and suspended in the air. The defects were placed at 30.55 in from the transmit coil or 61.08 in from the anchorage area. The magnet was placed under the strands about 7.63 ft away from the termination block. The strand was kept at a fixed height (2.5 in) from the surface of the magnet, about the same radius of the 5 in cable-bridge shown in the figure 4.10. A transmit/receive coil was placed around the strand near the magnet. The coil diameter was fixed at 5 in. This is to ensure that the coil fits around the 5 in diameter cable. We assumed that the strands are located at the center of the cable.
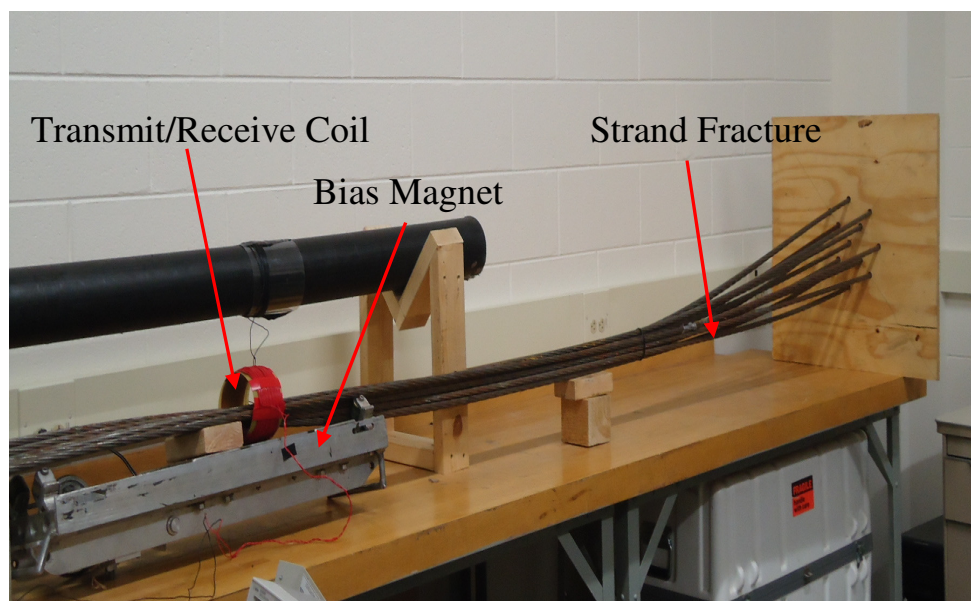
Figure 4.10 Cable-anchorage model with 13 spread out strands setup; showing bias magnet, transmit/receive coil and strand fracture location.

CHAPTER 5

RESULTS & DISCUSSION

_____

5.1 Introduction

This chapter presents the results of several experiments, using the prototype MFL system
and the cable-stayed bridge cable, to assess the capabilities and performance of the MFL
method to detect steel loss of section. The goal of the MS experiments was to assess the
feasibility and performance of the MS method in detecting steel loss of section within the
anchorage area of cable-stayed bridges.

5.2 MFL Laboratory Experiments

The magnet assembly was first mounted on top of the laboratory bridge cable and
connected to the data acquisition software. The magnet assembly was then moved to a
known starting point on the cable to establish a reference point for the start of the scan.
The experiments were carried out by inserting a strand, with known flaws, into the top or
the outer copper tube in the cable. The strand at this location was located 1.5 in from the
location of the magnetic sensors in the magnet assembly. The first inserted strand
contained seven broken wires (complete strand fracture). The strand was inserted inside
the copper tube until it reached a predetermined length for the location of the flaw. The
cable was scanned with the magnet assembly manually along the length of the cable in

searching for flaws. The magnet assembly was moved passed the location of the flaw, and then stopped at the end of the cable. When the magnet reached at the end of the cable, data acquisition was stopped and the magnet was moved back to the start point and readied for the next scan. Data was collected continuously during each scan and it was transferred to the computer where it was saved for post processing. The data from the top seven Hall-effect sensors were collected and viewed in real-time while scanning the cable. It was very clear to see how the signal from the flaw was developing as the magnet moved over the defect. When the first test was completed, the strand was removed and the second strand, with six broken wires, was inserted in the cable. Similar to the first scan, the magnet was moved over the flaw starting at the beginning of the cable from the same reference point and ending at the end of the cable -moving exactly the same distance. The rest of the scanning was performed similarly for the remaining strands with varying defect sizes. When this part of the testing at was completed, the first strand (with seven broken wires) was inserted in the center copper tube (located at 2.5 in of depth) in the cable. The strand was pushed inside the cable until it reached the predetermined flaw location, similar to the first experiment, to maintain consistent location of the flaw within the cable.

5.2.1 Effect of Seven Broken Wires at 1.5 in Depth Inside the Cable

The results of the first scan (seven broken wires in the outer copper tube) are shown in figures 5.1 and 5.2. The x-axis of the graph represents the distance the magnet travelled during the scan. The y-axis represents the amplitude of the magnetic flux that leaked outside the steel. The graph shows only the vertical components of the magnetic flux; the flat line in the graph indicates that there is no flux leakage. Any variations in the graph indicate the presence of a local disturbance of the magnetic field, and possibly an indication of the loss of section or presence of a flaw. The graphs clearly show strong variations based on the magnitude of the signal amplitude indicating the present of disturbances near that area. Comparing the location of the signal variations on the graph (x-axis) and the known location of the seven broken wires (at 1.5 ft), we can draw a clear correlation that the signal recorded was due to the seven broken wires in the strand. Furthermore, when these measurements are compared to the baseline data, it's clear that there are no signals recorded at this location; hence, the disturbances seen in the graph are due to the seven broken wires. Also, the data show that the signals recorded from all seven Hall-effect sensors vary in magnitude based on the location of each sensor. The maximum peak-to-peak magnitude (0.9V) is observed at sensor 4 which is the closest sensor to the flaw. Additionally, the graph shows that the signal amplitude decreases from sensors that are away from sensor 4 where the smallest magnitude (0.13V) is recorded at sensor 1. Also, the magnetic fluctuation decays rapidly as we move away from the location of the law.

Figure 5.1 MFL signals recorded from sensors 1 through 4 for seven broken wires. Larger signal amplitude values are resulted from sensors that are located closer to the defects, i.e., data from sensor 4 (d).

(a)

(b)

(c)

Figure 5.2 MFL signals recorded from sensors 5 through 7 for seven broken wires. Larger signal amplitude values are resulted from sensors that are located closer to defects, i.e., data from sensor 5 (a).

5.2.2 Effect of Six Broken Wires at 1.5 in Depth Inside the Cable

In this experiment the strand with seven wires broken was removed and a strand with 6 broken wires was inserted in the top or the outer copper tube in the cable. Similar to the first scan, the magnet was moved over the flaw location traveling exactly the same distance on the cable. The signals recorded for the defects of the 6-broken wire-strand are shown in figure 5.3 and 5.4. The signals from all seven sensors are almost identical to the defect signals of the seven-broken-wire strand, except that the peak-to-peak signal amplitude is lower. The data shows that the maximum signal amplitude recorded is about 0.8V; which corresponds to sensor 4 and sensor 5, as expected. Furthermore, the magnitude of the signal from sensor 4 and 5 is identical (0.8V), because the flaw is located exactly between the two sensors. The data also show that sensors 3 and 6 (which are adjacent to sensor 4 and 5 respectively) produced the next highest signal amplitude levels when compared to the signals from sensor 4 and sensor 5. It is also clear from the graphs that the signal from sensor 3 is identical to the signal from sensor 6 by symmetry. Similarly, the signals for sensor 2 and 7 are identical. However, the smallest signal recorded is from sensor 1, with a magnitude of 0.10V. This was also expected, since sensor 1 is the farthest from the location of the defects, hence it will sense much smaller magnetic field than the rest of the sensors.

(a)

(b)

(c)

(d)

Figure 5.3 MFL signals recorded from sensors 1 through 4 for six broken wires. Larger signal amplitude values are resulted from sensors that are located closer to defects, i.e., data from sensor 4 (d).

(a)

(b)

(c)

Figure 5.4 MFL signals recorded from sensors 5 through 7 for six broken wires. Larger signal amplitude values are resulted from sensors that are located closer to defects, i.e., data from sensor 5 (a).

5.2.3 Effect of Five Broken Wires at 1.5 in Depth Inside the Cable

In this experiment the strand with six broken wires was removed and a strand with five broken wires was inserted in the outer copper tube in the cable. The data for the defects of the five broken wires in the strand is shown in figure 5.5 and figure 5.6. Consistent with the previous two experiments for 7-wires and 6-wires broken strands, the maximum signal is recorded from sensors 4 and 5. As seen from the graph, the peak-to-peak magnitude of the signal for sensors 4 and 5 is also identical- about 0.7V. The signals from the rest of the sensors follow the pattern as in the previous two experiments, where sensor 1 shows the smallest magnitude of about 0.08V peak-to-peak. The symmetry between sensor 3 and 6, and 2 and 7 is also observed.

Figure 5.5 MFL signals recorded from sensors 1 through 4 for five broken wires. Larger signal amplitude values are resulted from sensors that are located closer to defects, i.e., data from sensor 4 (d).

(a)

(b)

(c)

Figure 5.6 MFL signals recorded from sensors 5 through 7 for five broken wires. Larger signal amplitude values are resulted from sensors that are located closer to defects, i.e., data from sensor 3 (a).

5.2.4 Effect of Four Broken Wires at 1.5 in Depth Inside the Cable

In this experiment the strand with five-broken-wires was removed and a strand with 4 broken wires was inserted in the outer copper tube in the cable. The data for the defects in the strand with 4-broken wire is shown in figure 5.7 and figure 5.8. Consistent with the previous results, the maximum signal is recorded from sensors 4 and 5. As seen from the graph, the peak-to-peak magnitude of the signal for sensors 4 and 5 is also identical-about 0.5V. The signals from the rest of the sensors follow the pattern as in the previous experiments, where, sensor 1 shows the smallest magnitude of about 0.05V peak-to-peak. The symmetry between sensor 3 and 6, and 2 and 7 is also observed.

(a)

(b)

(c)

(d)
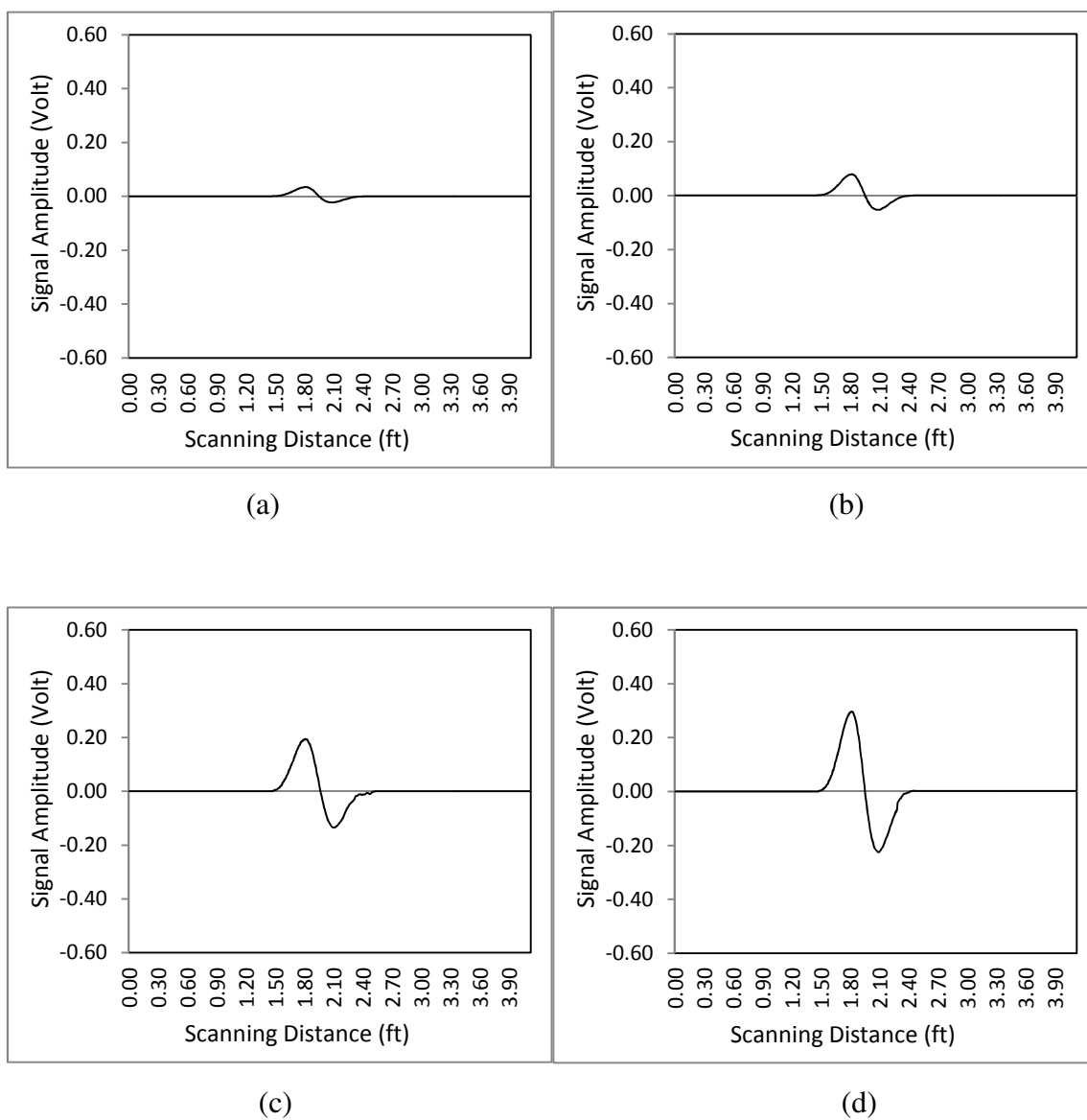
Figure 5.7 MFL signals recorded from sensors 1 through 4 for four broken wires. Larger signal amplitude values are resulted from sensors that are located closer to defects, i.e., data from sensor 4 (d).

(a)

(b)

(c)
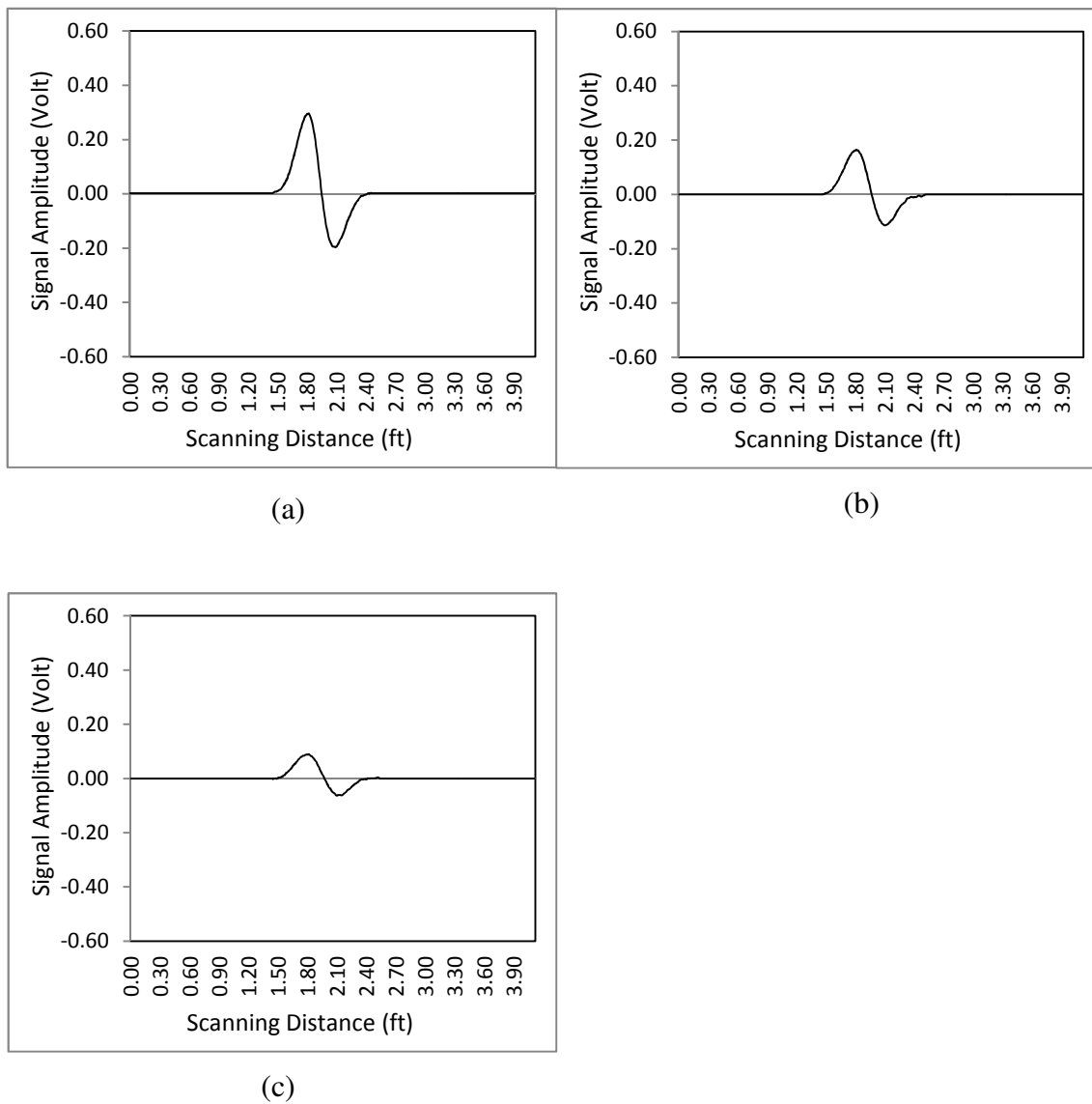
Figure 5.8 MFL signals recorded from sensors 5 through 7 for four broken wires. Larger signal amplitude values are resulted from sensors that are located closer to defects, i.e., data from sensor 3 (a).

5.2.5 *Effect of Three Broken Wires at 1.5 in Depth Inside the Cable*

The data for the defect in a strand with three broken wires are shown in figures 5.9 and figure 5.10. As seen from the graph, the peak-to-peak magnitude of the signal for sensors 4 and 5 is almost identical- about 0.35 V. The signals from the rest of the sensors follow the pattern as in the previous experiments, where, sensor 1 shows the smallest magnitude of about 0.04V peak-to-peak. The symmetry between sensor 3 and 6, and 2 and 7 is also observed.

(a)   (b)
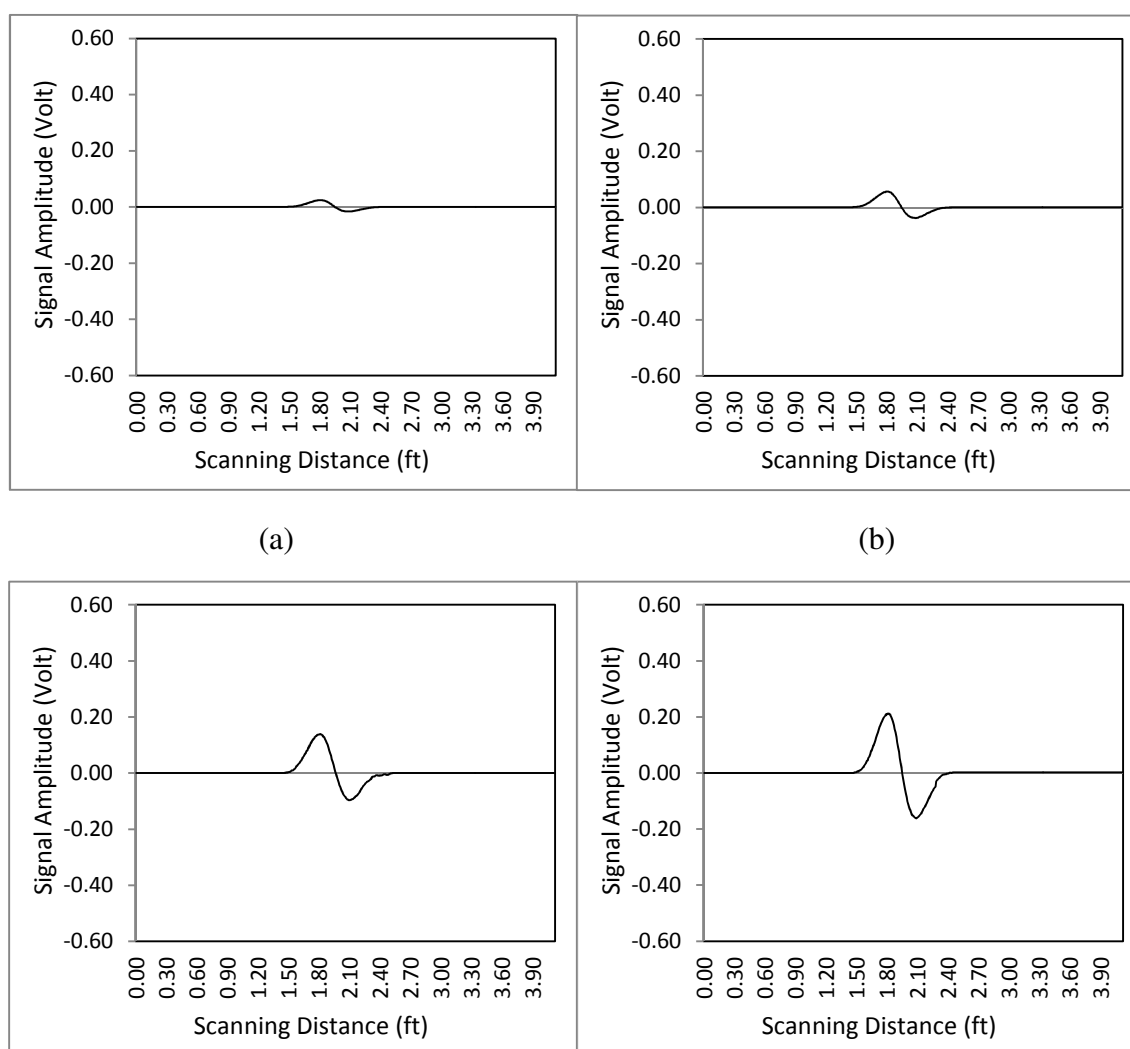
Figure 5.9 MFL signals recorded from sensors 1 through 4 for three broken wires. Larger signal amplitude values are resulted from sensors that are located closer to defects, i.e., data from sensor 4 (d).
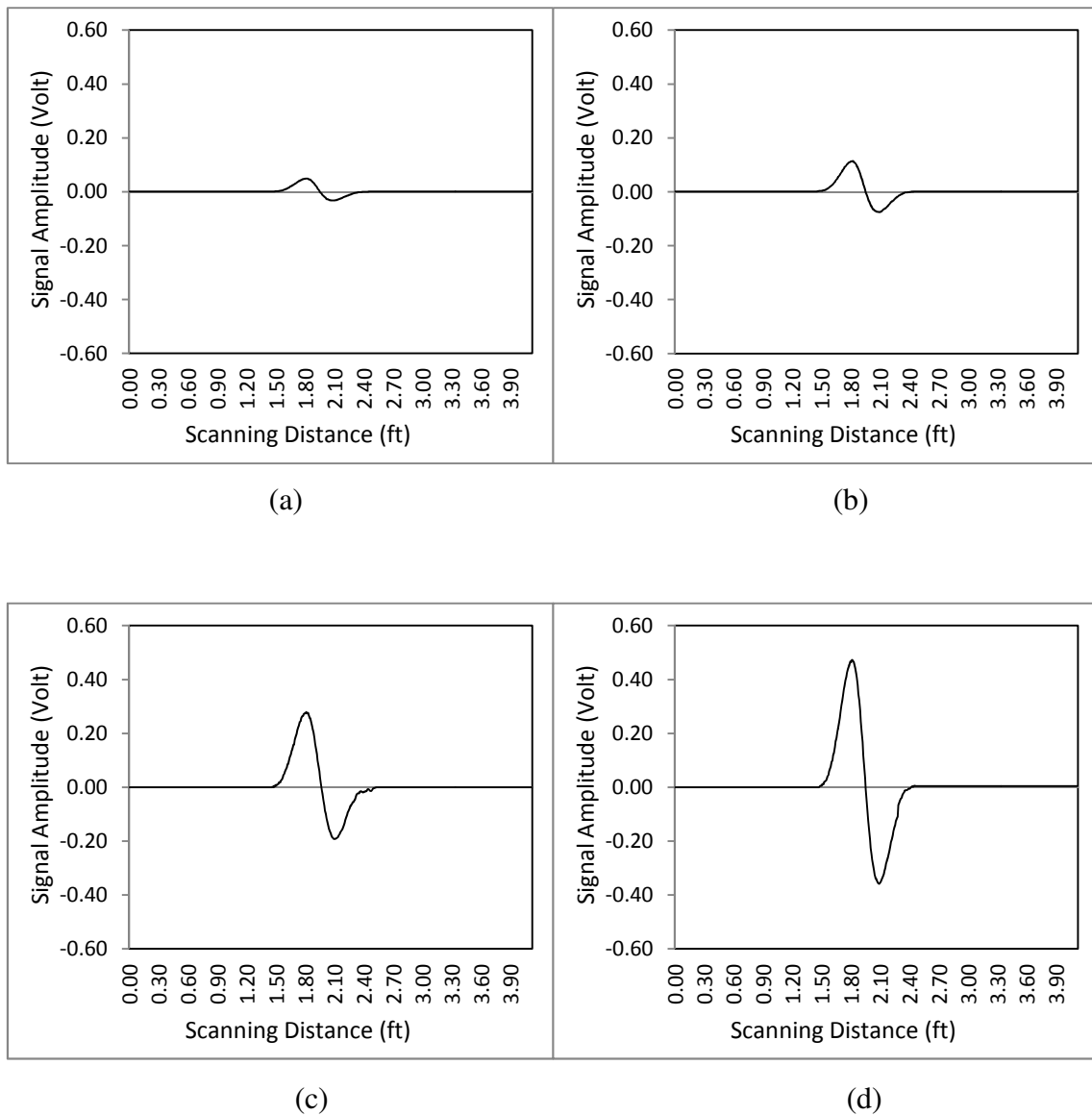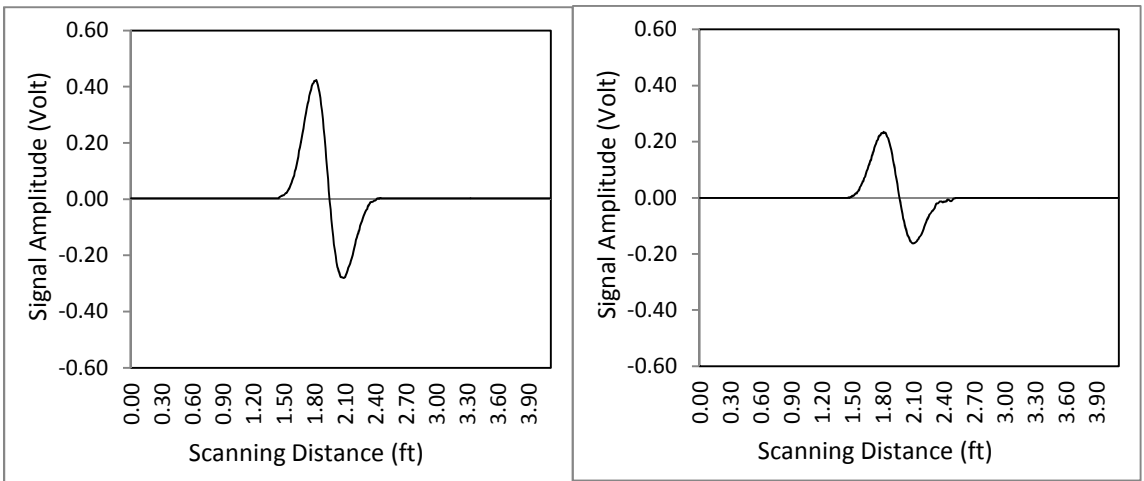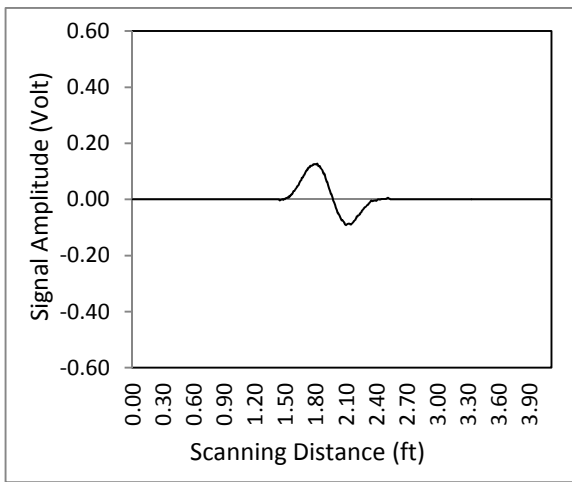
(a)

(b)

(c)
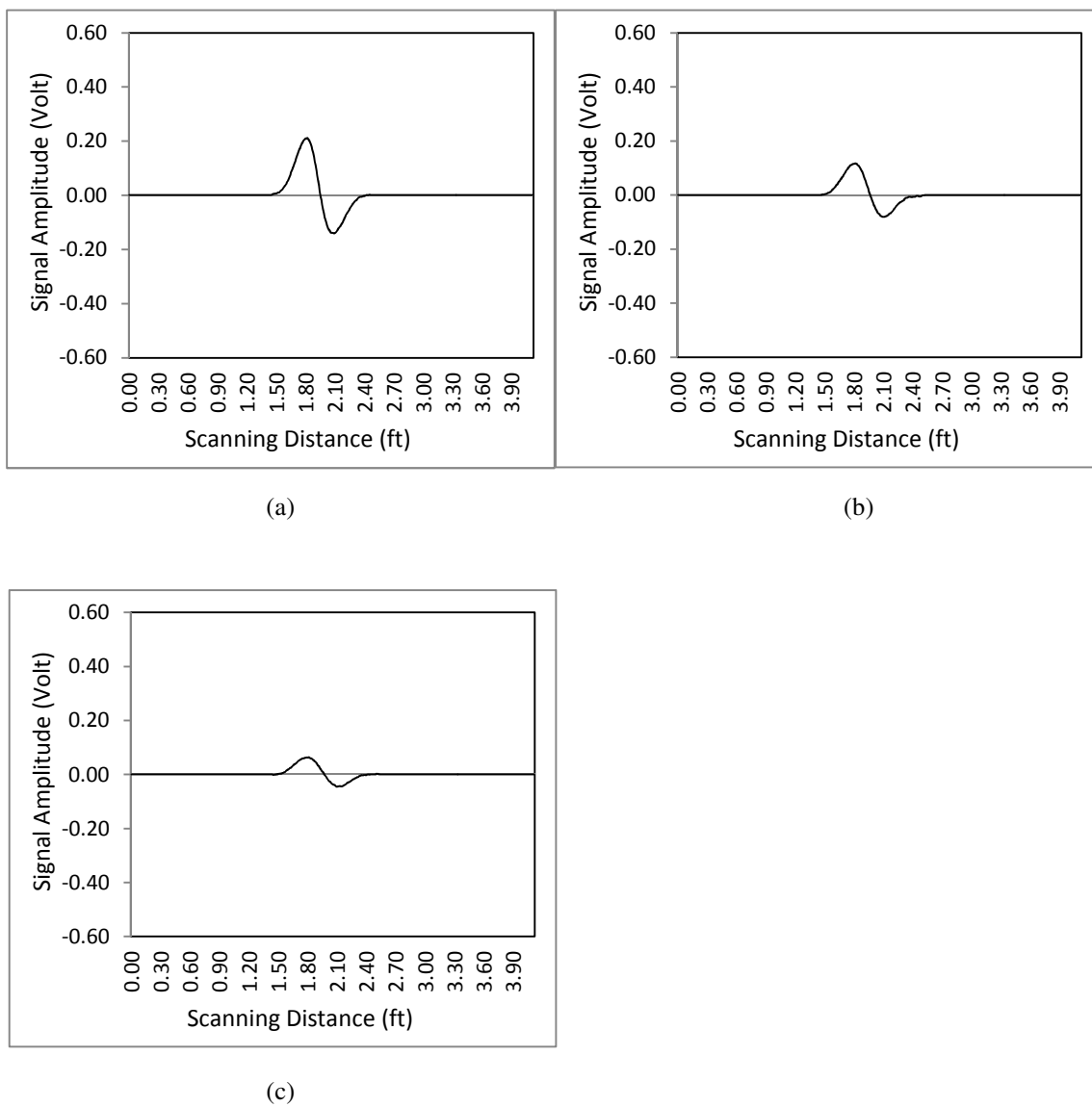
Figure 5.10 MFL signals recorded from sensors 5 through 7 for three broken wires. Larger signal amplitude values are resulted from sensors that are located closer to defects, i.e., data from sensor 3 (a).

5.2.6 *Effect of Two Broken Wires at 1.5 in Depth Inside the Cable*

The data for the defects for the two broken wires strand is shown in figures 5.11 and figure 5.12. As seen from the graph, the peak-to-peak magnitude of the signals from sensors 4 and 5 is almost identical- about 0.3V. The signals from the rest of the sensors follow the pattern as in the previous experiments, where, sensor 1 shows the smallest magnitude of about 0.03V peak-to-peak. The symmetry between sensor 3 and 6, and 2 and 7 is also observed.

(a)　　　　　　　　　　　　　　　　　　(b)

(c)　　　　　　　　　　　　　　　　　　(d)
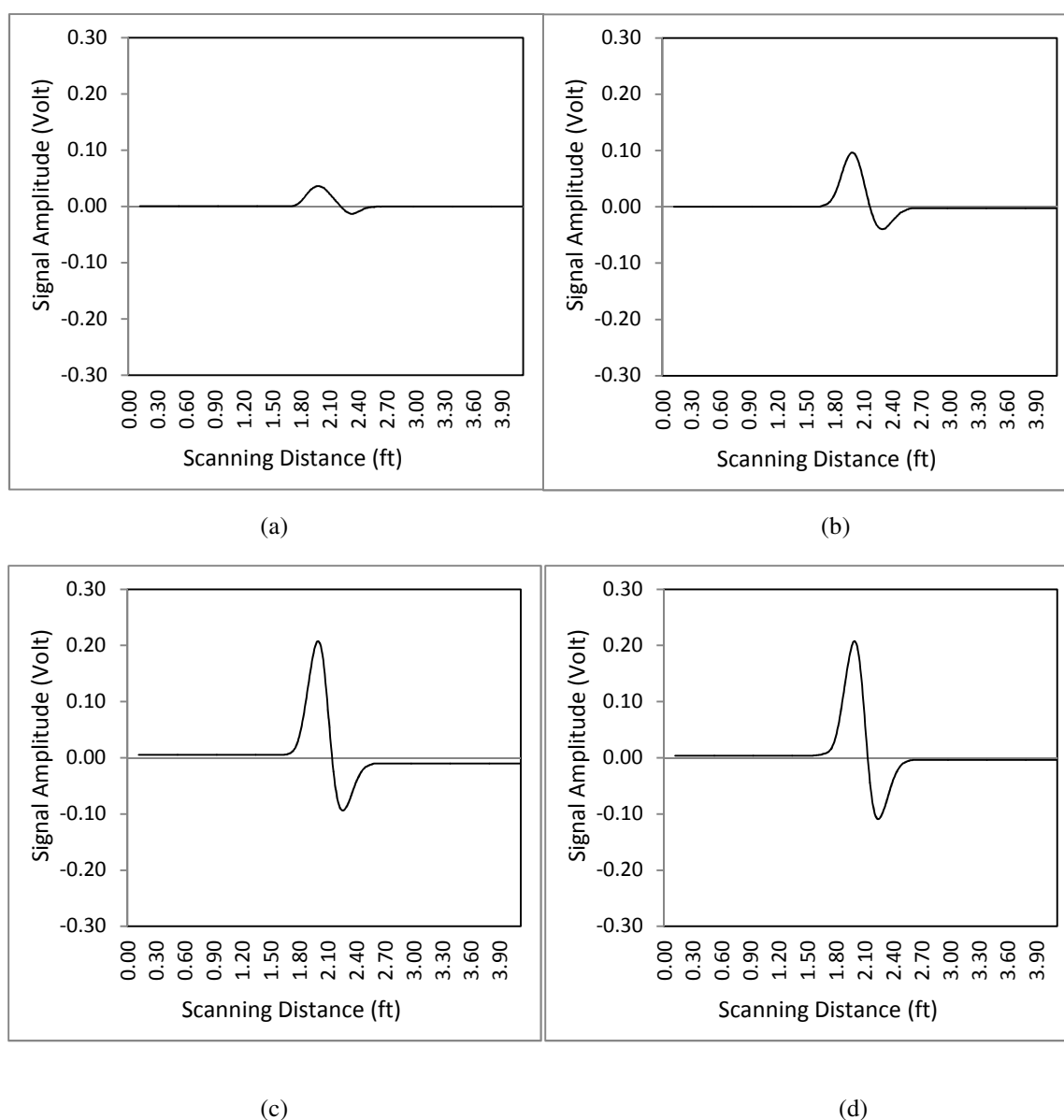
Figure 5.11 MFL signals recorded from sensors 1 through 4 for two broken wires. Larger signal amplitude values are resulted from sensors that are located closer to defects, i.e., data from sensor 4 (d).

(a)   (b)

(c)
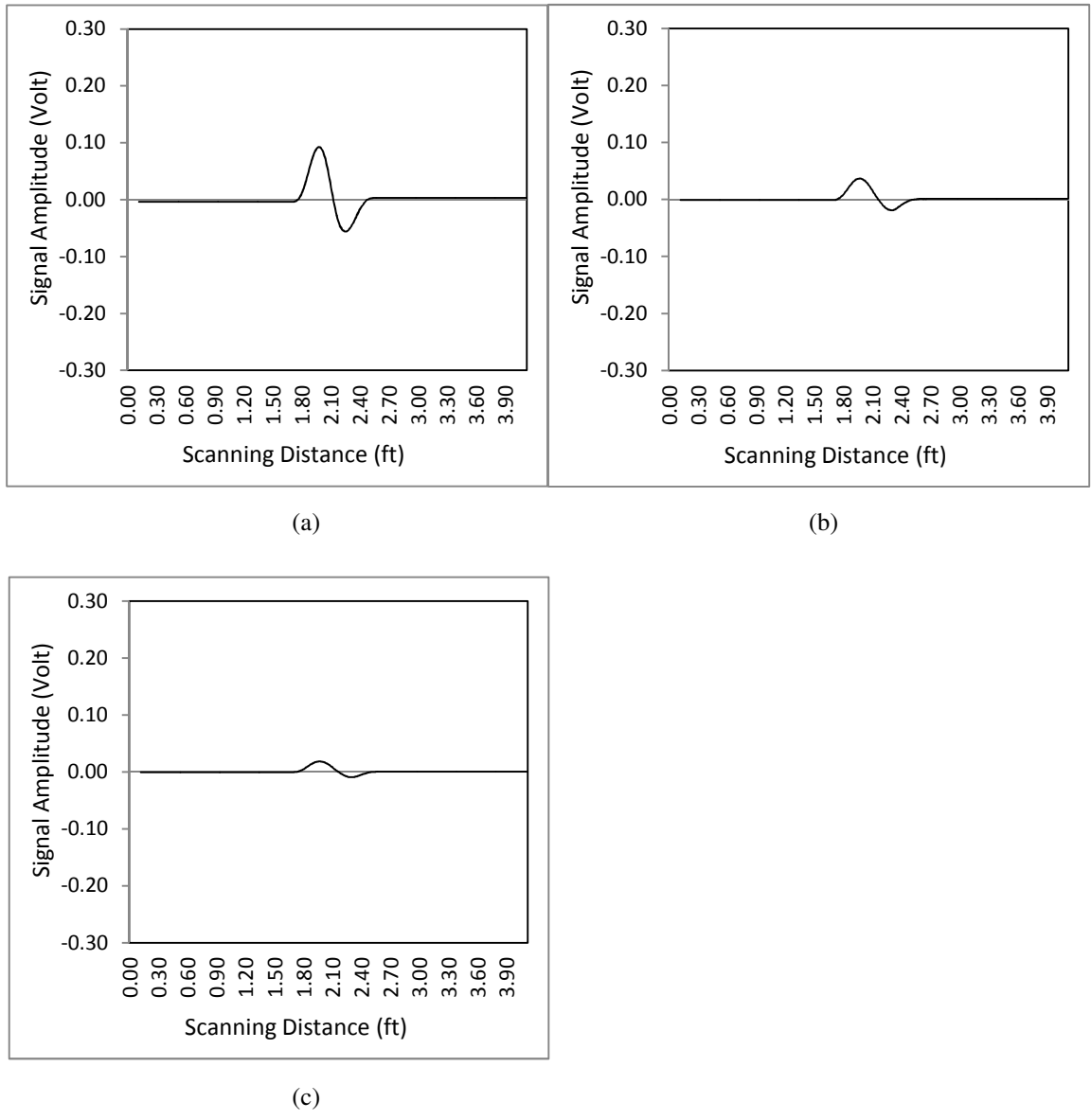
Figure 5.12 MFL signals recorded from sensors 5 through 7 for two broken wires. Larger signal amplitude values are resulted from sensors that are located closer to defects, i.e., data from sensor 3 (a).

5.2.7 Effect of One Broken Wire at 1.5 in Depth Inside the Cable

In the last experiment at 1.5 in depth a strand with 1 broken wire defect was inserted in the outer copper tube in the cable. The results for this experiment are shown in figure 5.13 and figure 5.15. As seen from the graph, the peak-to-peak magnitude of the signals for sensor 3 and 4 is almost identical -about 0.06V. This is slightly different than the results from previous experiments, which is probably due to an operating error where in moving the magnet assembly shifted slightly causing a shift in the proximity of the sensors to the flaw location. Similarly, the signals from the rest of the sensors follow the same pattern, where the smallest signal is now recorded from sensor 7 at about 0.01 V. Also, it is very clear from the graph of sensor 1 and sensor 7 that the signal is relatively very small and that it was difficult to identify the signal where the signal suffers some degradation. The results of the experiments are summarized in figure 5.15. The graph shows that the MFL system offers good response and sensitivity to the size of flaws varying from 1-broken wire to 7-broken wires in a strand.
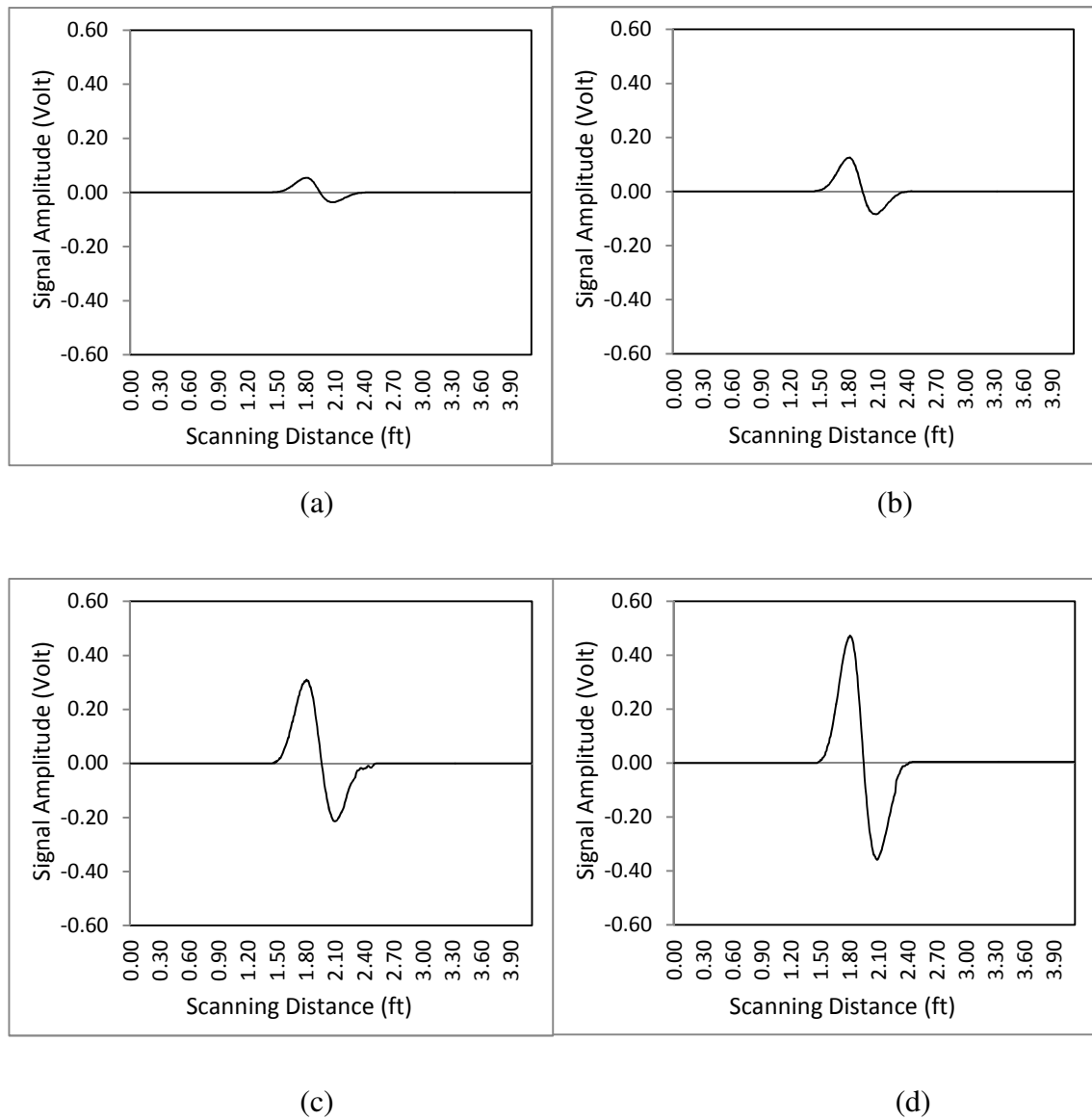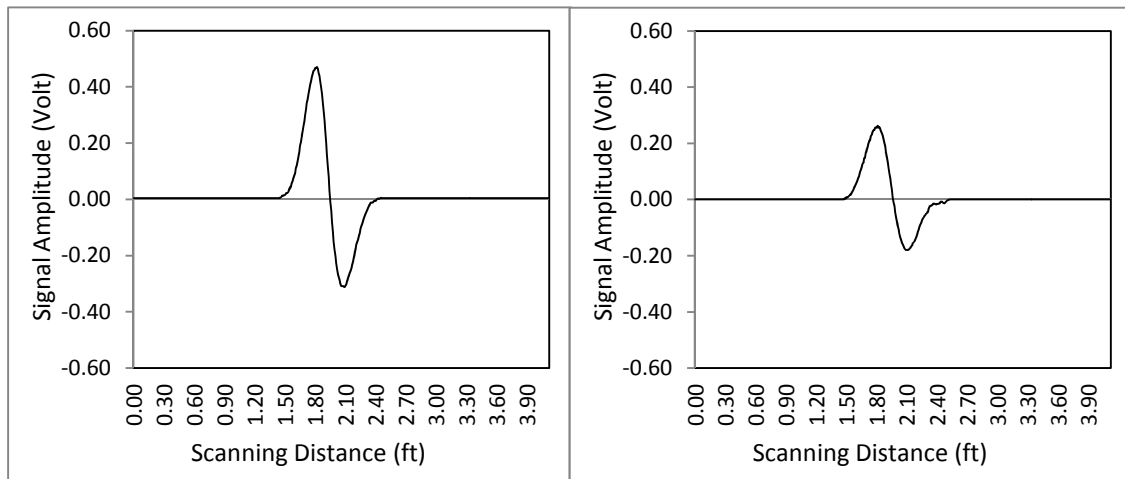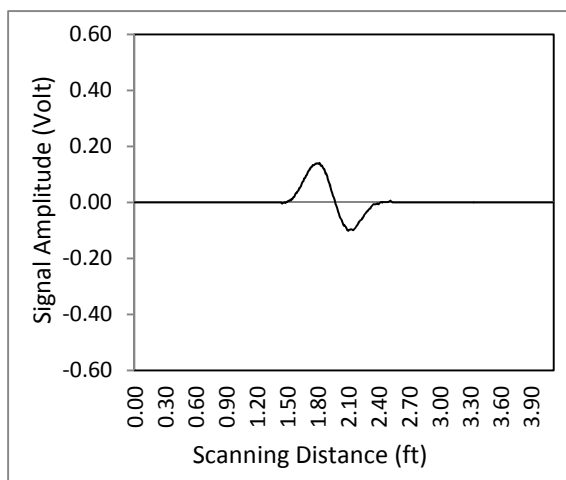
(a)

(b)

(c)

(d)
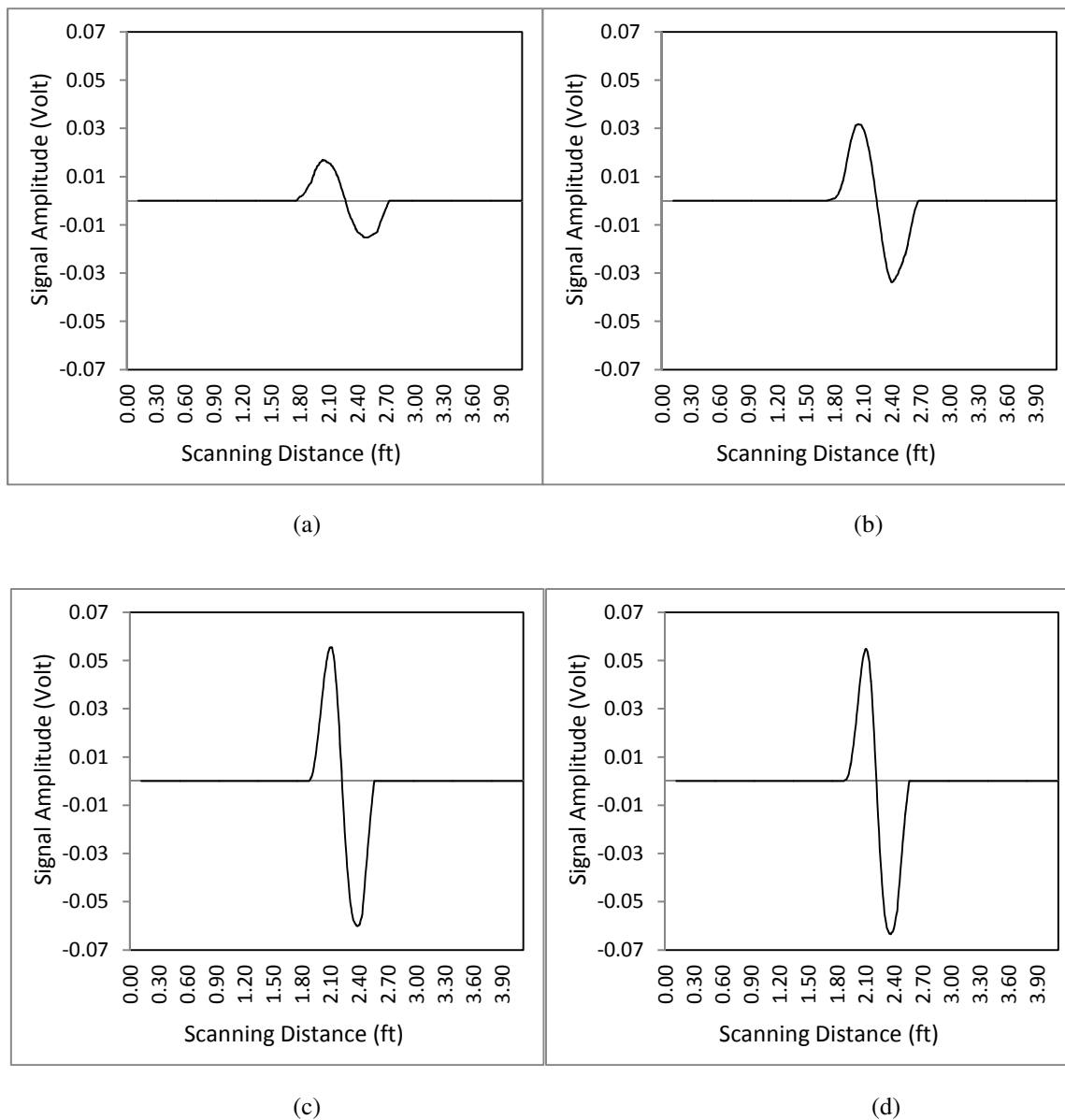
Figure 5.13 MFL signals recorded from sensors 1 through 4 for one broken wire. Larger signal amplitude values are resulted from sensors that are located closer to defects, i.e., data from sensor 4 (d).
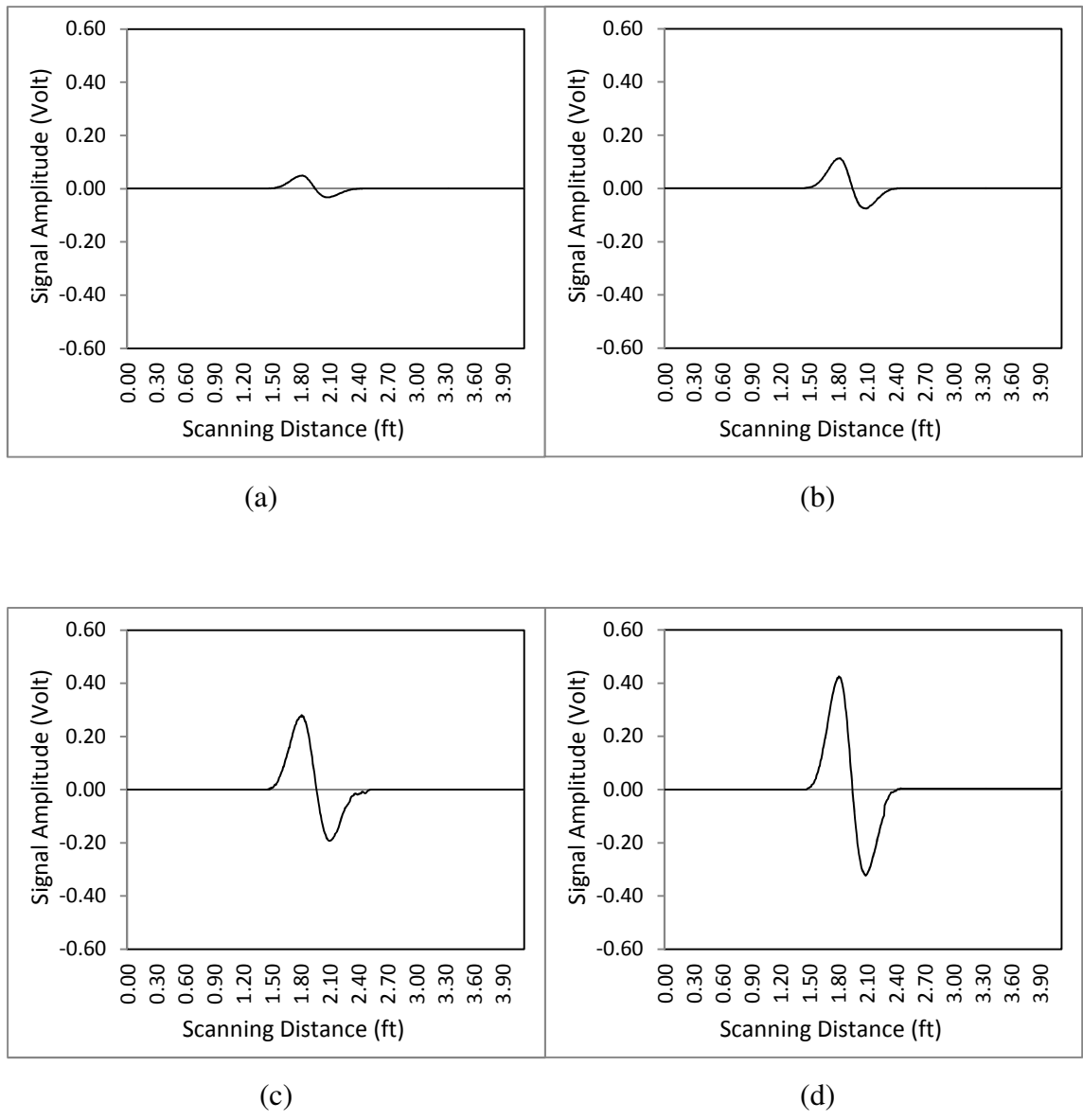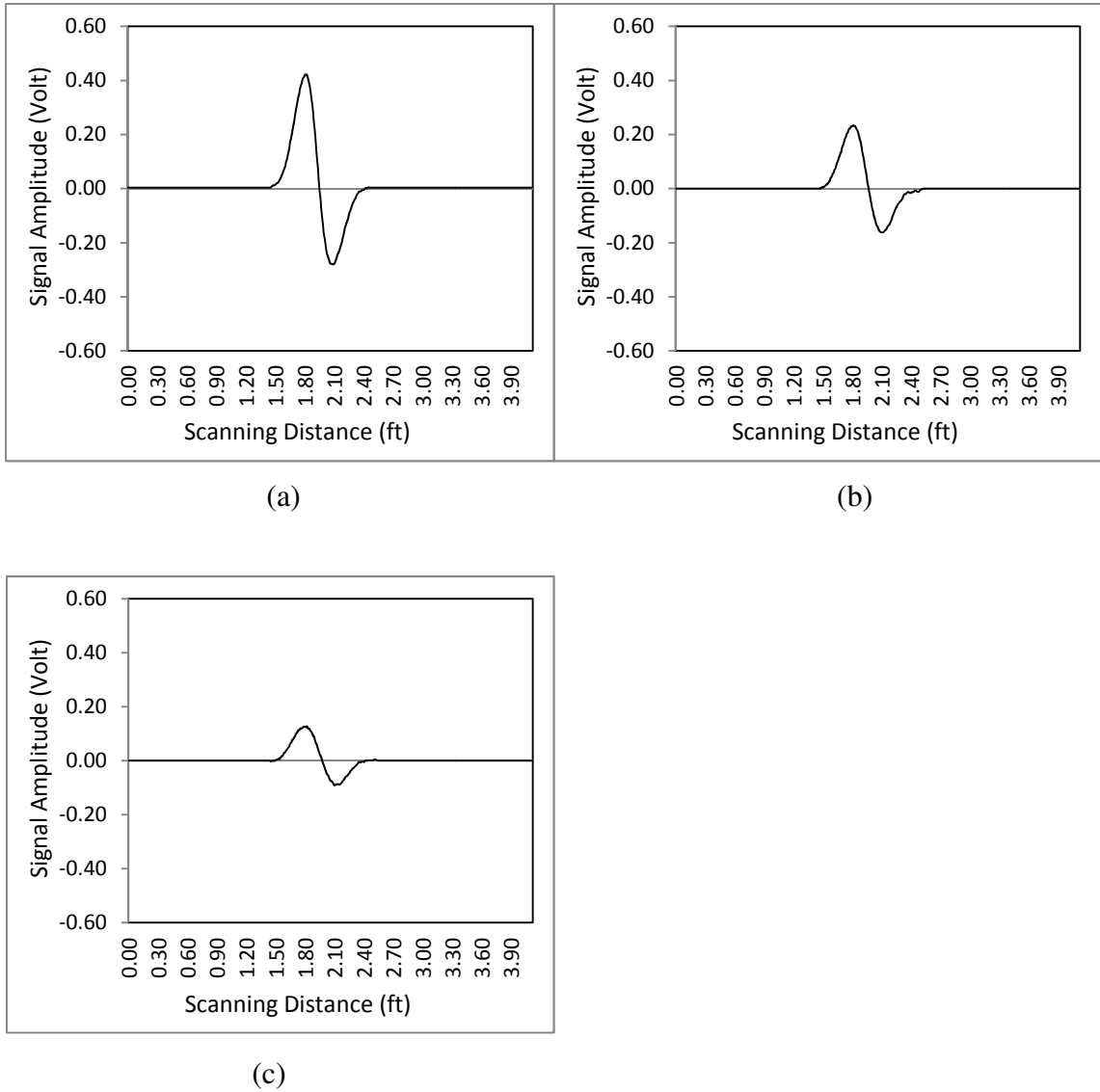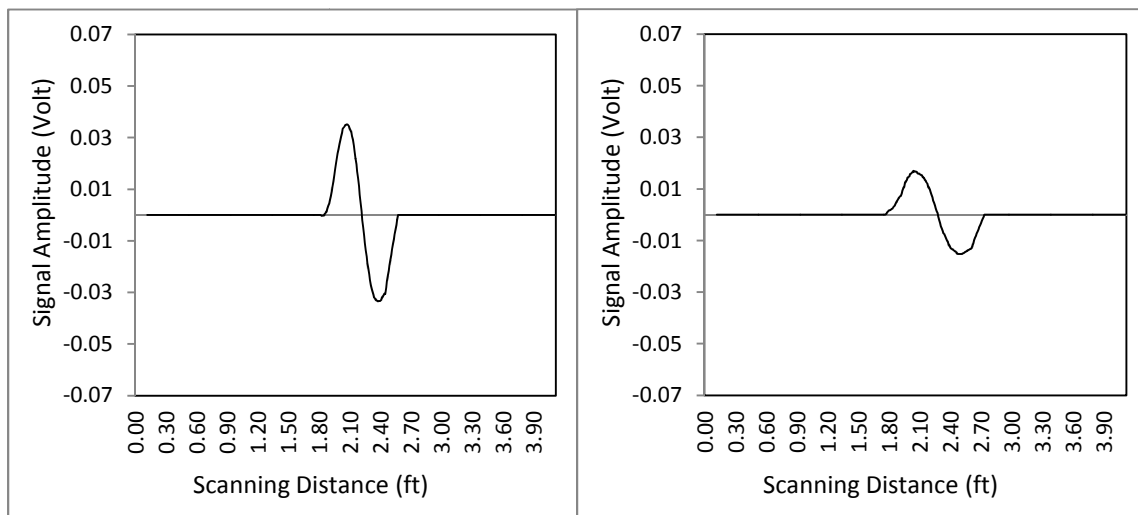
(a)

(b)
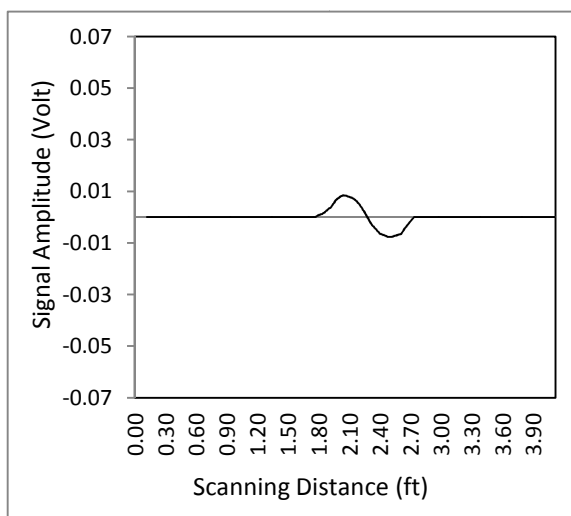
(c)

Figure 5.14 MFL signals recorded from sensors 5 through 7 for one broken wire. Larger signal amplitude values are resulted from sensors that are located closer to defects, i.e., data from sensor 3 (a).
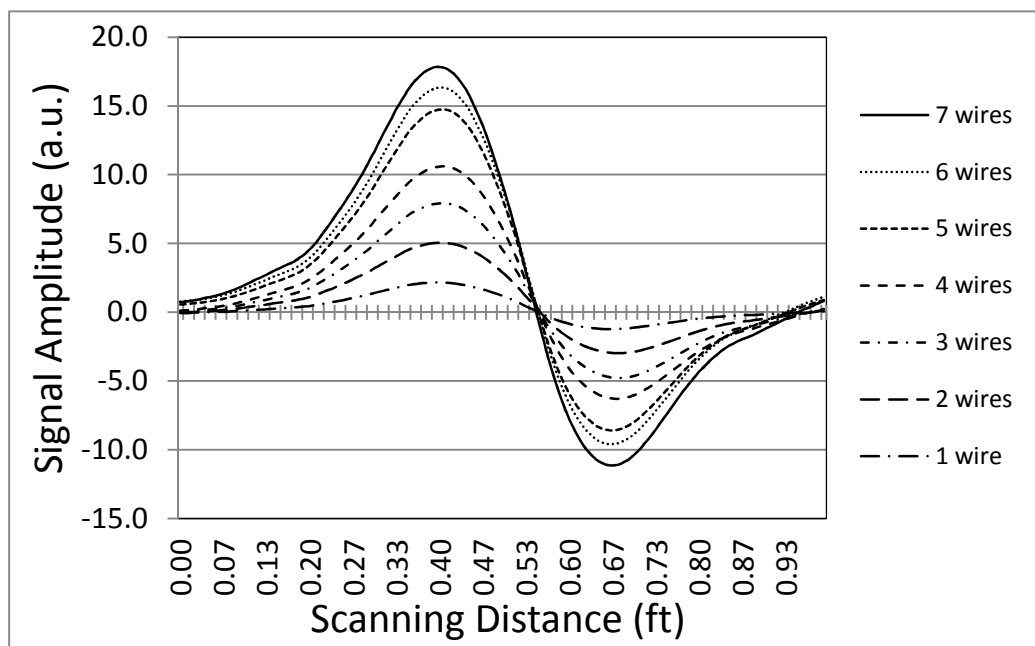
Figure 5.15 Relationship between the magnitude of the MFL signal and flaw size (number of broken wires).

5.3 MS Laboratory Experiments on Single Strand

5.3.1 Baseline Measurements with no Defect

The first experiment was conducted on a single strand with no flaws to obtain baseline measurements, as seen in figure 5.16 and figure 5.17. The horizontal scale in figure 5.16 is the time in milliseconds and the vertical scale is the signal magnitude in volts. The time scale is referenced to the start of the transmitted wave (point P), shown in the far left side of the graph. The graph shows the acquired signal taken over a 6 msec period. The reflection from the near-side end of the strand is shown at point E1 with a signal magnitude of 2.2 Vp-p. Point E2 is at reflected signal from the far-side end of the strand and E11 indicates reflections due to round trip waves initiated from the near-side end reflection. The location of the strand-end was verified by measuring the time it took for the incident wave to travel a round-trip distance from the transmitter coil to the end of the strand and back to the receiver coil. The velocity of wave propagation in the steel is assumed to be 16,978.3 ft/sec.
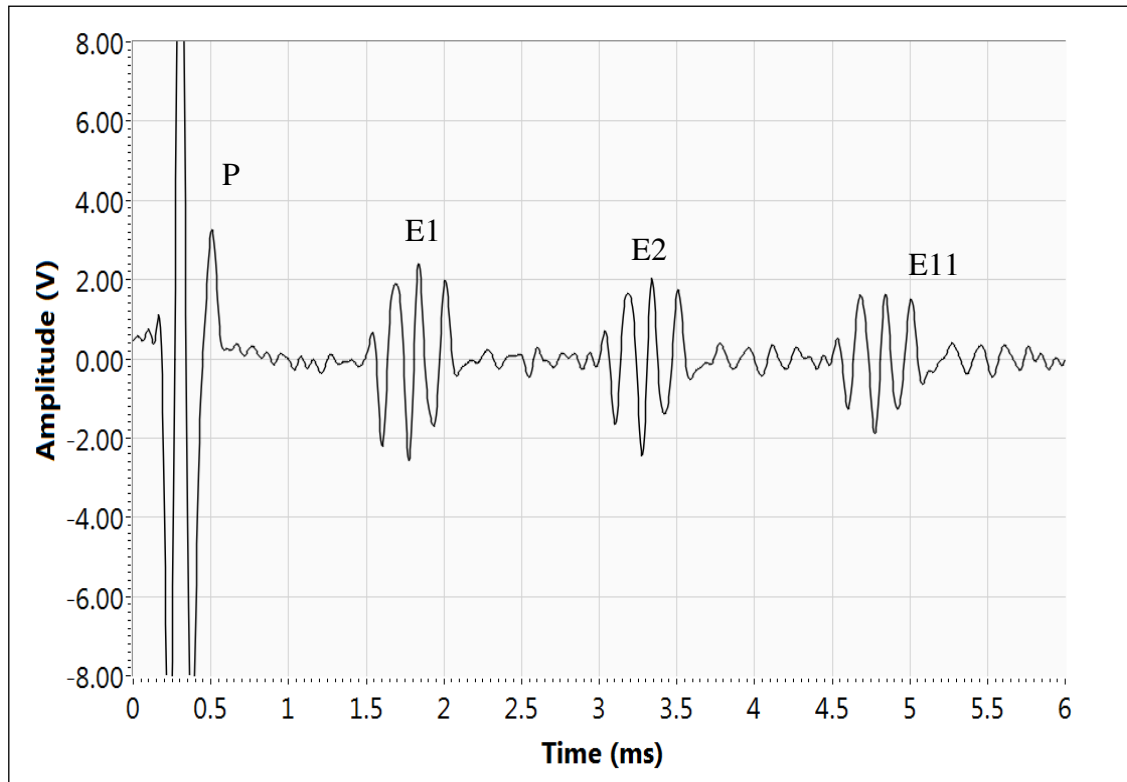
Figure 5.16 Wave reflections from the baseline strand with no flaws. P is the initial transmitted pulse, E1 is the reflection from the near-side end of the strand, E2 is the reflection from the far-side end of the strand, and E11 is at the round trip wave propagation initiated from the near-side end reflection.

Figure 5.17 A 7-wire strand with no flaws used for baseline measurements.

5.3.2 Effect of One-Broken-Wire Defect

The second experiment was conducted on a strand with one broken wire as defect. The acquired signal is shown in figure 5.18 and the defect is shown in figure 5.19. Point D1 indicates the signal reflection from the one broken wire defect. The magnitude of the signal is 0.6 Vp-p, which is slightly larger than the base line signal of 0.25 Vp-p. E1 and E2 are the signal reflections from the near-side end and the far-side end of the strand, respectively.
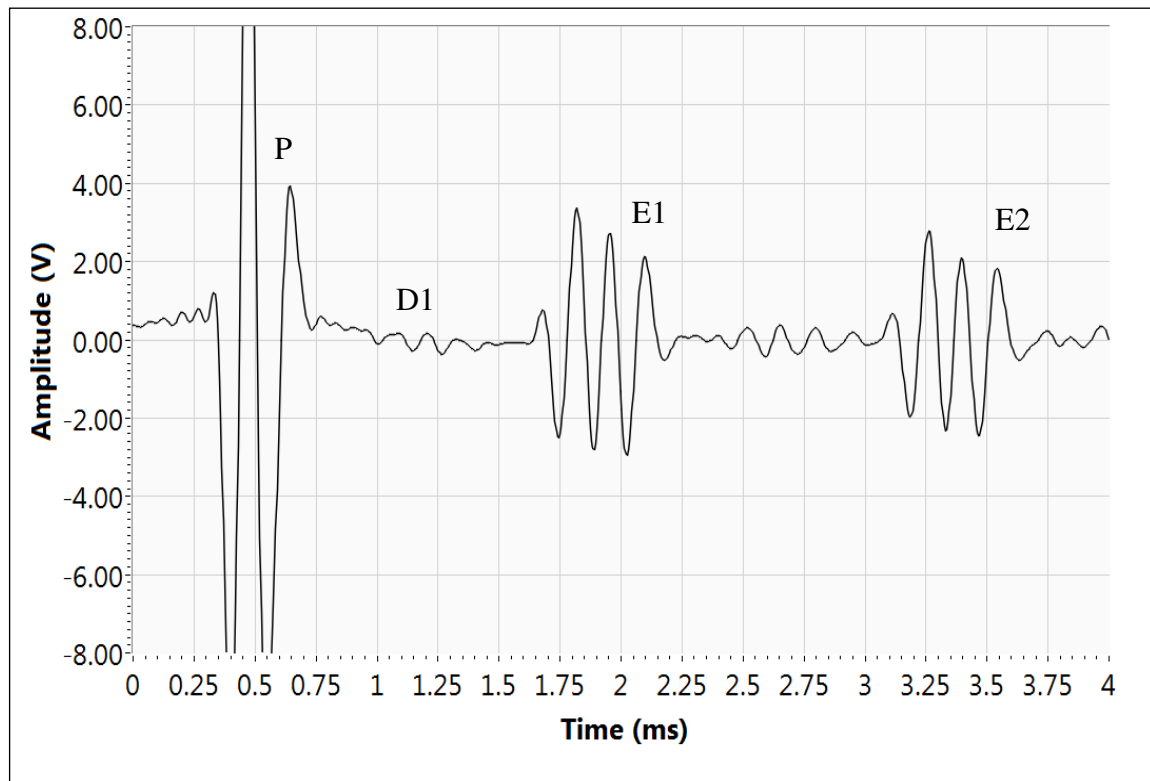
Figure 5.18 Wave reflections from the strand with one-broken-wire defect. P is the initial transmitted pulse; D1 is the signal reflection from the defect. E1 is the reflection from the near-end of the strand; E2 is the reflection from the far-end of the strand.

Figure 5.19 7-wire strand with one-broken-wire defect.

The location of the one-broken-wire defect was verified by measuring the time at D1 from Figure 5.18 and using the following equation to calculate the distance:

D=V*T

Where, D is the distance of the defect measured from the location of the transmitting coil in meters. V is the velocity of the longitudinal wave at 16,978.3 ft/sec and T is the round trip time for longitudinal wave to travel from the transmit coil to the defect in milliseconds. From figure 5.18, T is measured from the center of the defects signal (D1) to the center of the transmitted wave (P).

T=1.123-0.50=0.623 msec

D= (0.623 msec*16,978.3 ft/sec)/2=63.46 in

The calculated location of the defect (63.46 in) very well matches the physical location of the defect on the strand from the setup in figure 4.7.

5.3.3 Effect of Two-Broken-Wire Defect

The third experiment was conducted on a strand with a two-broken-wire defect. The result of the acquired signal is shown in figure 5.20 and the defect is shown in figure 5.21. Point D1 is the signal reflection from the two-broken-wire defect with a signal amplitude of 1.0 Vp-p. E1 and E2 are the signal reflections from the near-side end and the far-side end of the strand, respectively. The signal magnitude from the two-broken-wire defect is larger than the one-broken-wire defect. This is expected since the two-broken-wire defect is 100% larger than the one-broken-wire, as such, more signal is reflected from the defect. The rest of the wave continued to propagate past the defect, however, with less energy since part of the energy was reflected at the defect. Hence, E1 magnitude is slightly smaller than E1 from the one-broken-wire experiment.
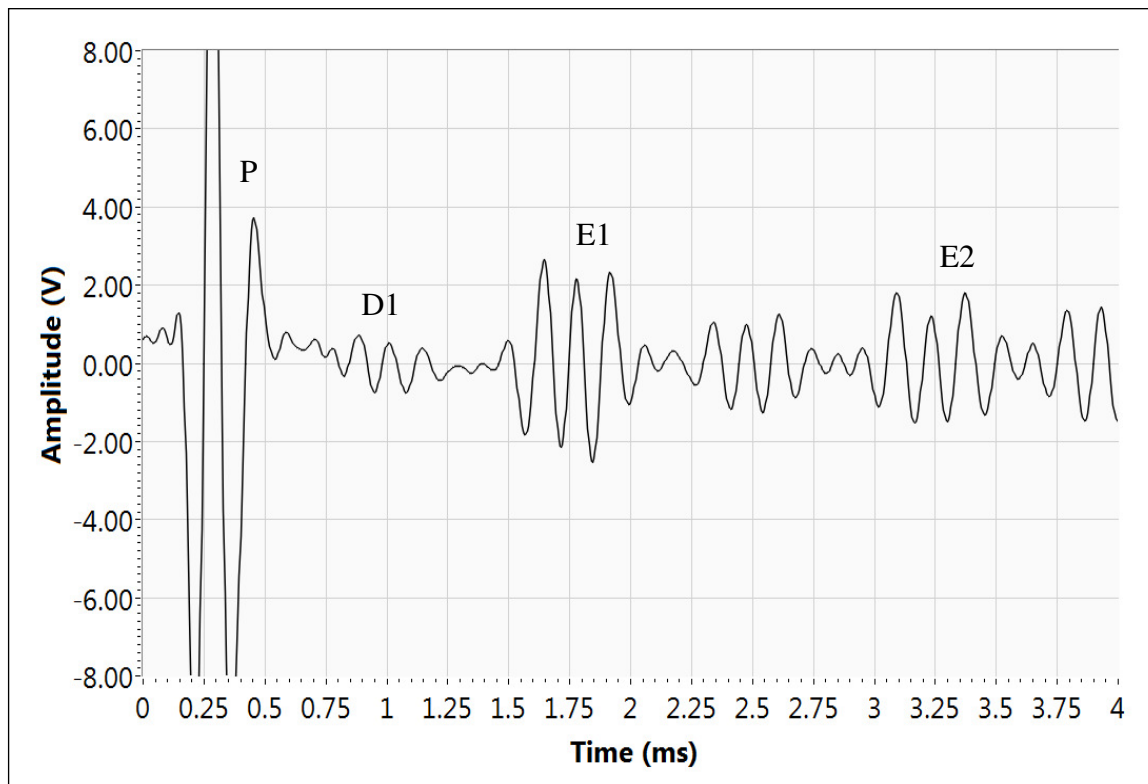
Figure 5.20 Wave reflections from the strand with two-broken-wire defect. P is the initial transmitted pulse; D1 is the signal reflection from the defect. E1 is the reflection from the near-side end of the strand; E2 is the reflection from the far-side end of the strand.

Figure 5.21 The 7-wire strand with two-broken-wire defect.

5.3.4 *Effect of Three-Broken-Wire Defect*

The 4th experiment was conducted on a strand with a three-broken wire defect. The result of the acquired signal is shown in figure 5.22 and the defect is shown in figure 5.23. Point D1 indicates the signal reflection from the three-broken wire defect with a signal amplitude of 1.8 Vp-p. E1 and E2 are the signal reflections from near-side end and far-side end of the strand, respectively. Consistent with the previous results, the magnitude of the reflected signal from the defect D1 is larger compared to two-broken-wire defect while E1 magnitude has decreased.
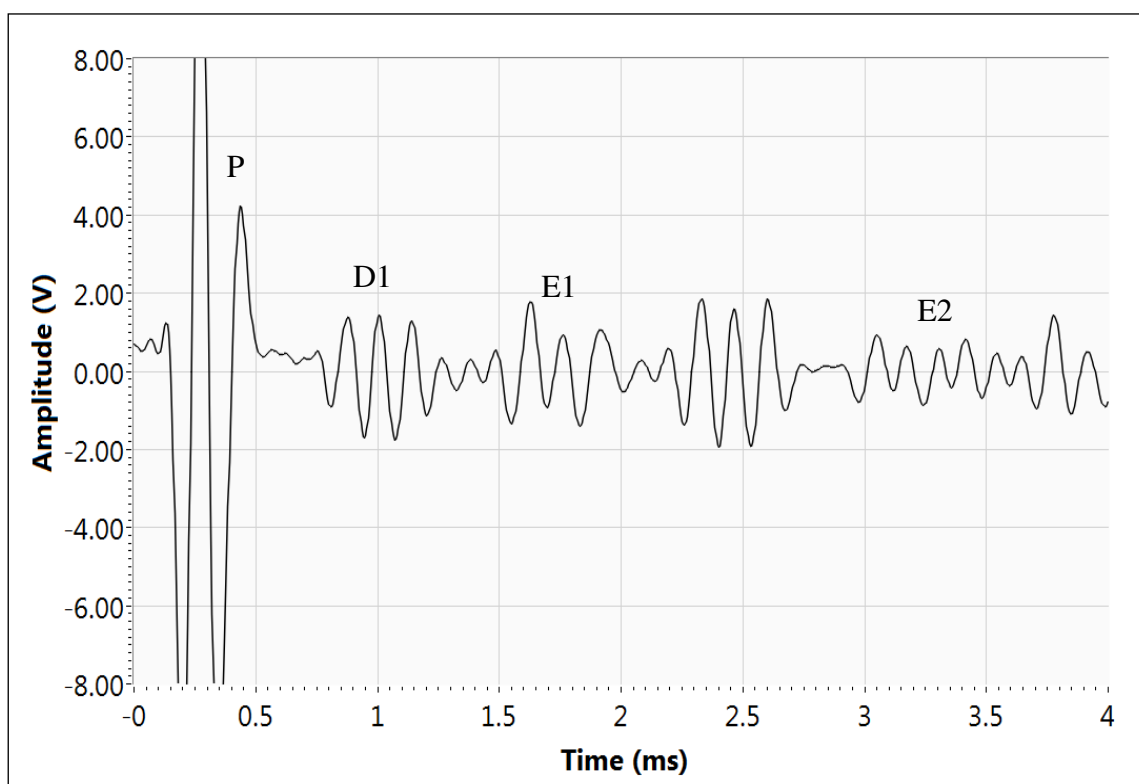
Figure 5.22 Wave reflections from the strand with the three-broken-wire defect. P is the initial transmitted pulse; D1 is the signal reflection from the defect. E1 is the reflection from the near-side end of the strand; E2 is the reflection from the far-side end of the strand.

Figure 5.23 7-wire strand with three-broken-wire defect.

5.3.5 *Effect of Six-Broken-Wire Defect*

The fifth experiment was conducted on a strand with a six-broken wire defect. The result of the acquired signal is shown in figure 5.24 and the defect is shown in figure 5.25. Point D1 indicates the signal reflection from the six-broken-wire defect with a signal of 4.0 Vp-p. E1 and E2 are the signal reflections from near-side end and far-side end of the strand, respectively. The data shows that the majority of the wave was reflected from the six-broken wire defect while a small portion of the transmitted signal propagated to the far-end of the strand.
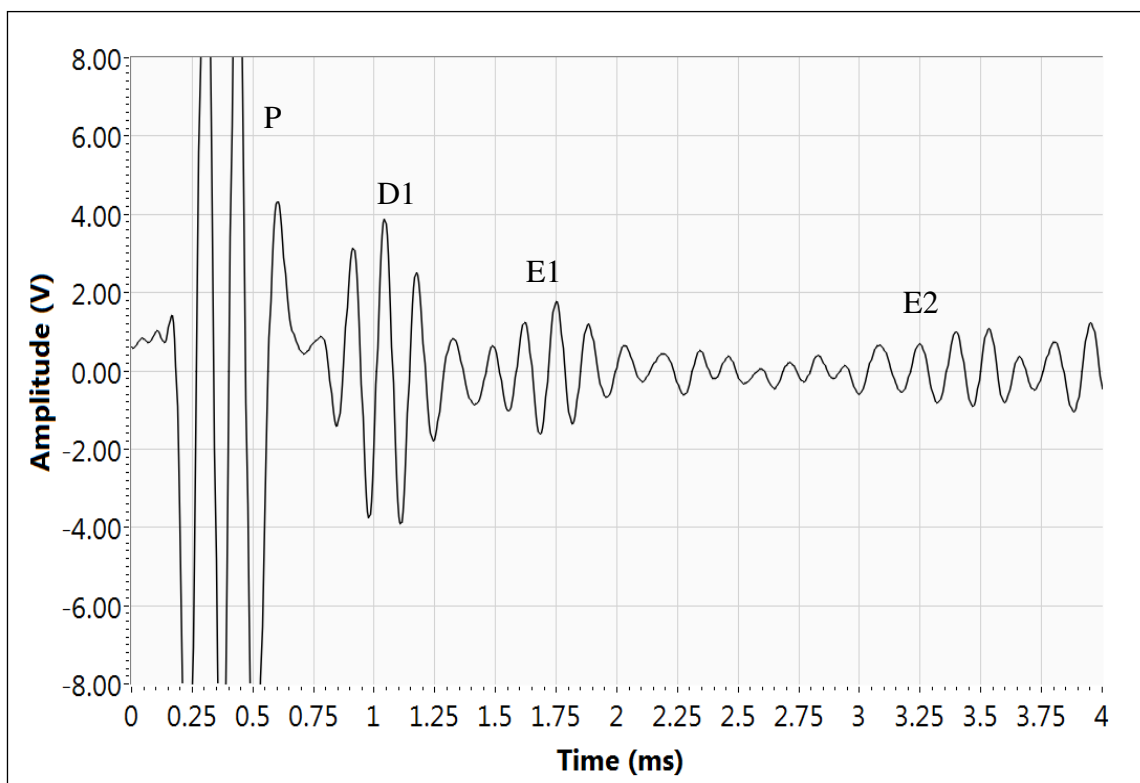
Figure 5.24 Wave reflections from the strand with the six-broken-wire defect. P is the initial transmitted pulse; D1 is the signal reflection from the defect. E1 is the reflection from the near-side end of the strand; E2 is the reflection from the far-side end of the strand.

Figure 5.25 7-wire strand with six-broken-wire defect.

The amplitude values for the reflected signals from the experiments were plotted as shown in figure 5.26. The graph shows that the amplitude of the reflected signal is proportional to the size of the defect (or the number of broken wires). This verifies that the system is responsive to the size of the defect and is capable of detecting defects with varying sizes.

Volt P-P

Number of broken wires
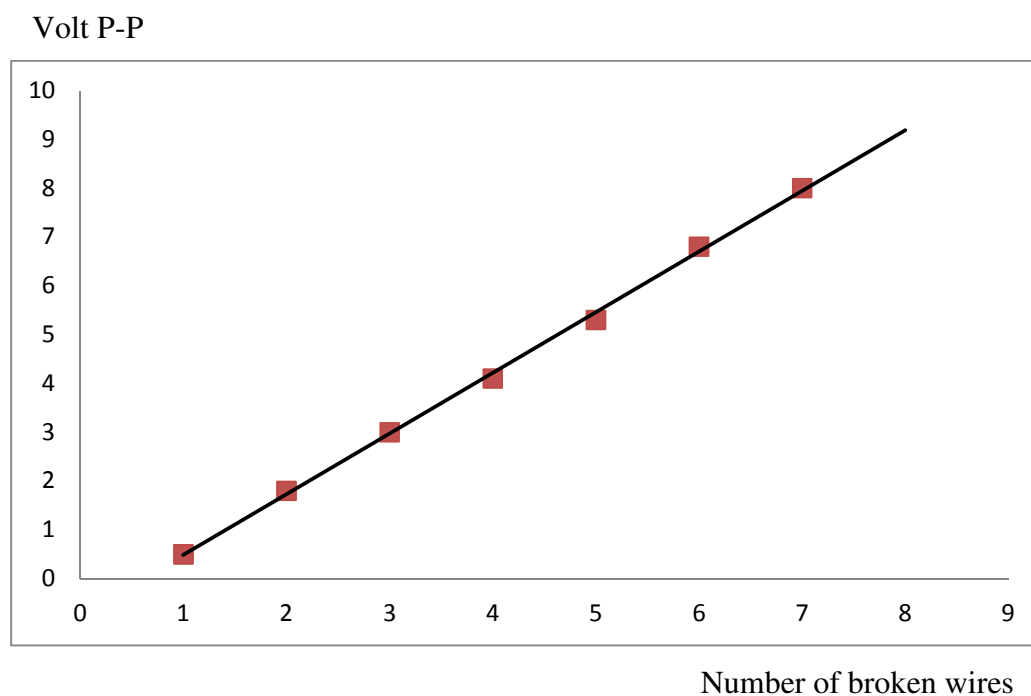
Figure 5.26 Graph to demonstrate the relationship between the magnitude of the reflected signal and the size of the defect.

5.4 MS Lab Experiments on Simulated Anchorage Area

5.4.1 Baseline Measurements with no Defects

The first experiment was conducted on the 13-strands anchorage model with no flaws to obtain baseline measurements, as seen in figure 5.27. The graph shows the acquired signal over a 1.5 msec period. The horizontal scale is the time in milliseconds and the vertical scale is the signal amplitude in volts. The time scale is referenced to the start of the transmitted wave (point P), shown in the far left side of the graph. The reflection from near-side end of the strand is shown at point E1 with signal amplitude of 11.0 Vp-p. The reflection from the far-side end of the cable is not shown here, since the defects are placed between the transmitting coil and the near-side end of the cable. Figure 5.28 shows the 13-strands spread out and anchored to a wooden termination plate to simulate the real cable anchorage area.
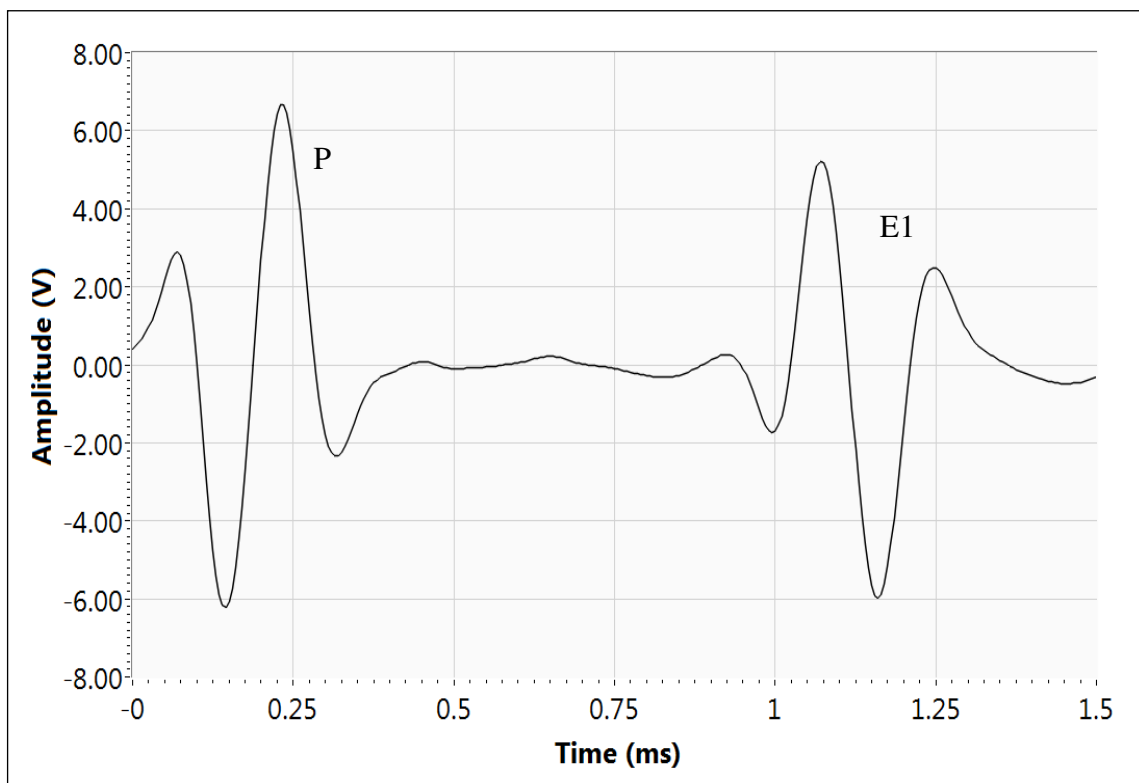
Figure 5.27 Wave reflections from the 13-strands anchorage area no defects (baseline measurements). P is the initial transmitted pulse; E1 is the reflection from the near-side end of the cable at the anchorage area.

Figure 5.28 13-fan-out strands anchorage area.

5.4.2 *Effect of One-Broken Strand Defect*

The second experiment was conducted on the cable within the anchorage area with a one-broken-strand defect. The acquired signal is shown in figure 5.29 and the defect is shown in figure 5.30. Point D1 is the signal reflection from the one-broken-strand defect. The magnitude of the signal is 0.9 Vp-p, which is slightly larger than the base line signal of 0.5 Vp-p. E1 indicates the signal reflections from near-side end of the cable in the anchorage area. E1 signal amplitude is 9.5 Vp-p, which is slightly lower than the amplitude from the base-line measurements. Similar to the single-strand experiments, this is expected because a part of the transmitted waves was reflected at the defect and the rest of the waves propagated to the end of the cable in the anchorage area.
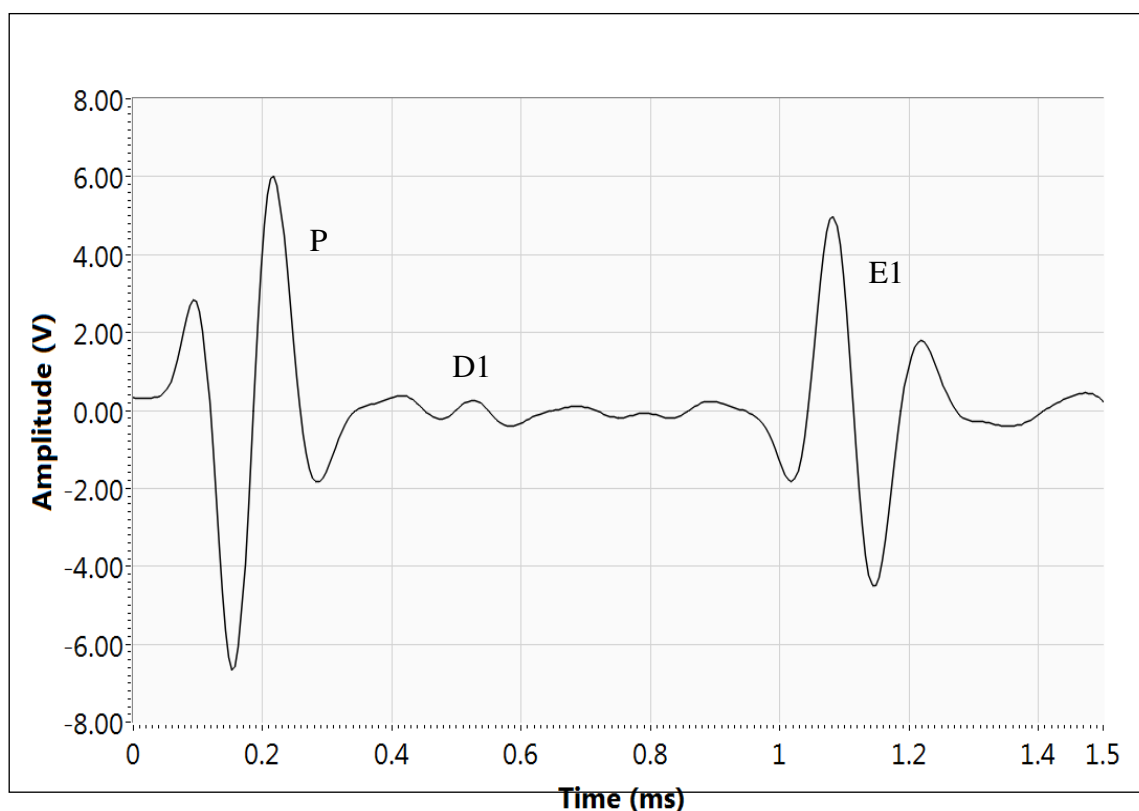
Figure 5.29 Wave reflections from the 13-strands anchorage area with one-broken-strand defect. P is the initial transmitted pulse; D1 is the signal reflection from the defect. E1 is the reflection from the near-side end of the cable

Figure 5.30 One-broken strand defect at the anchorage area**.**

The location of the one-broken-strand defect was verified by measuring the time at D1 from Figure 5.29 and using the following equation to calculate the distance:

D=V*T

Where, D is the distance of the defect measured from the location of the transmit coil in meters. V is the velocity of the longitudinal wave 16,978.3 ft/sec and T is the round trip time for longitudinal wave to travel from the transmitting coil to the defect in milliseconds. From figure 5.29, T is measured from the center of the defects signal (D1) to the center of the transmitted wave (P).

T = 0.50-0.20 = 0.30 msec

D = (0.30 msec*16,978.3 ft/sec)/2 = 30.55 in

The calculated location of the defect (30.55 in) matched very well with the physical location of the defect (30.55 in) within the anchorage area from the setup in figure 4.10.

Similarly E1 was verified to be the reflection from the anchorage area by measuring the time between P and E1 from figure 5.29 and repeat the distance calculations as follows:

T = 1.10 - 0.20 = 0.90 msec

D = (0.90 msec*16,978.3 ft/sec)/2 = 7.64 ft

The calculated location for E1 (7.64 ft) matched very well with the physical location of the anchorage area from the setup in figure 4.10.

5.4.3 Effect of Two-Broken-Strand Defect

The 3rd experiment was conducted on the anchorage area with a two-broken-strand defect. The acquired signal is shown in figure 5.31. Point D1 indicates the signal reflection from the three-broken-strand defect. The magnitude of the signal is 1.8 Vp-p, which is slightly larger than the signal reflection from on-broken-strand defect of 0.9 Vp-p. E1 is the signal reflections from near-side end of the cable within the anchorage area. E1 signal amplitude is 8.8 Vp-p, which is slightly lower than that from the base-line measurement. Similar to the single-strand experiments, this is expected because a part of the transmitted wave was reflected at the defect and the remaining part of the waves propagated to the end of the cable within the anchorage area.
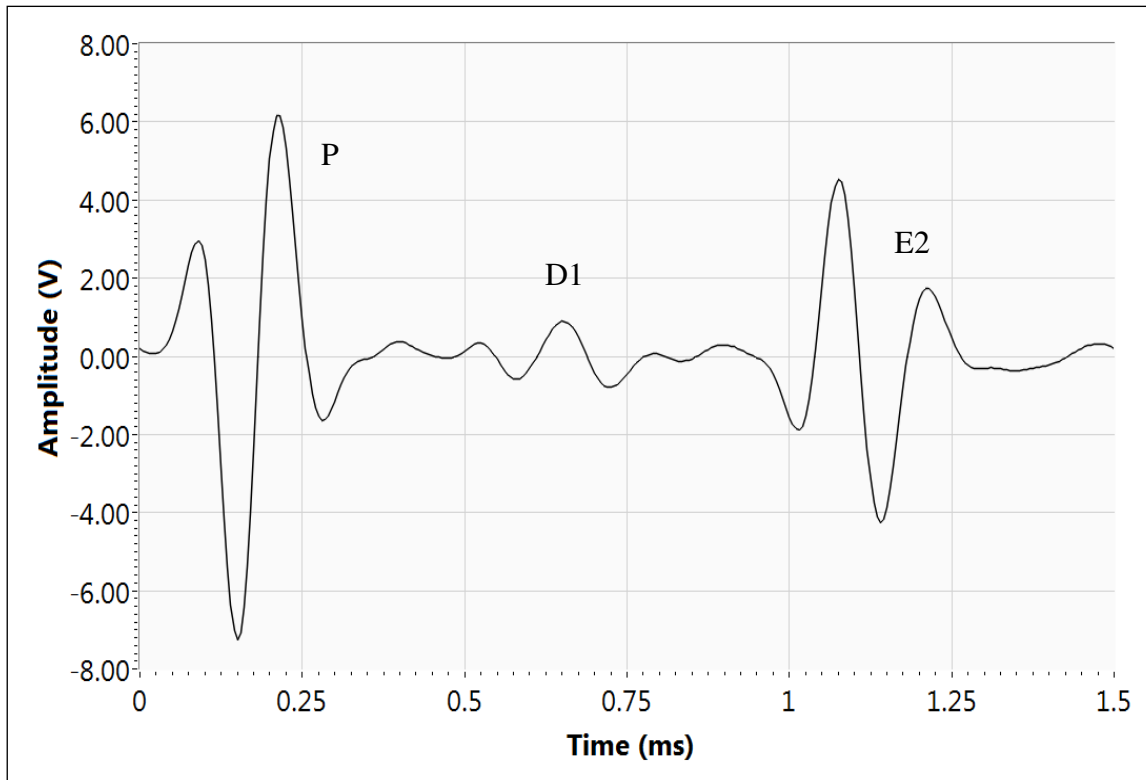
Figure 5.31 Wave reflections from the 13-strands anchorage area with two-broken strand defect. P is the initial transmitted pulse; D1 is the signal reflection from the defect. E1 is the reflection from the near-side end of the strand

5.4.4 Effect of Three-Broken-Strand Defect

The 4rd experiment was conducted on cable within the anchorage area with a three-broken-strand defect. The acquired signal is shown in figure 5.32. Point D1 indicates the signal reflection from the three-broken-strand defect. The magnitude of the signal is 2.6 Vp-p, which is slightly larger than the signal reflection from the two-broken-strand defect of 0.1.8 Vp-p. E1 indicates the signal reflections from the near-side end of the cable within the anchorage area. E1 signal magnitude is 8.4 Vp-p, which is slightly lower than that from the measurement for the two-broken-strand defect. Similar to the single-strand experiments, this is expected because a part of the transmitted wave was reflected at the defect and the remaining part of the waves propagated to the end of the cable within the anchorage area.
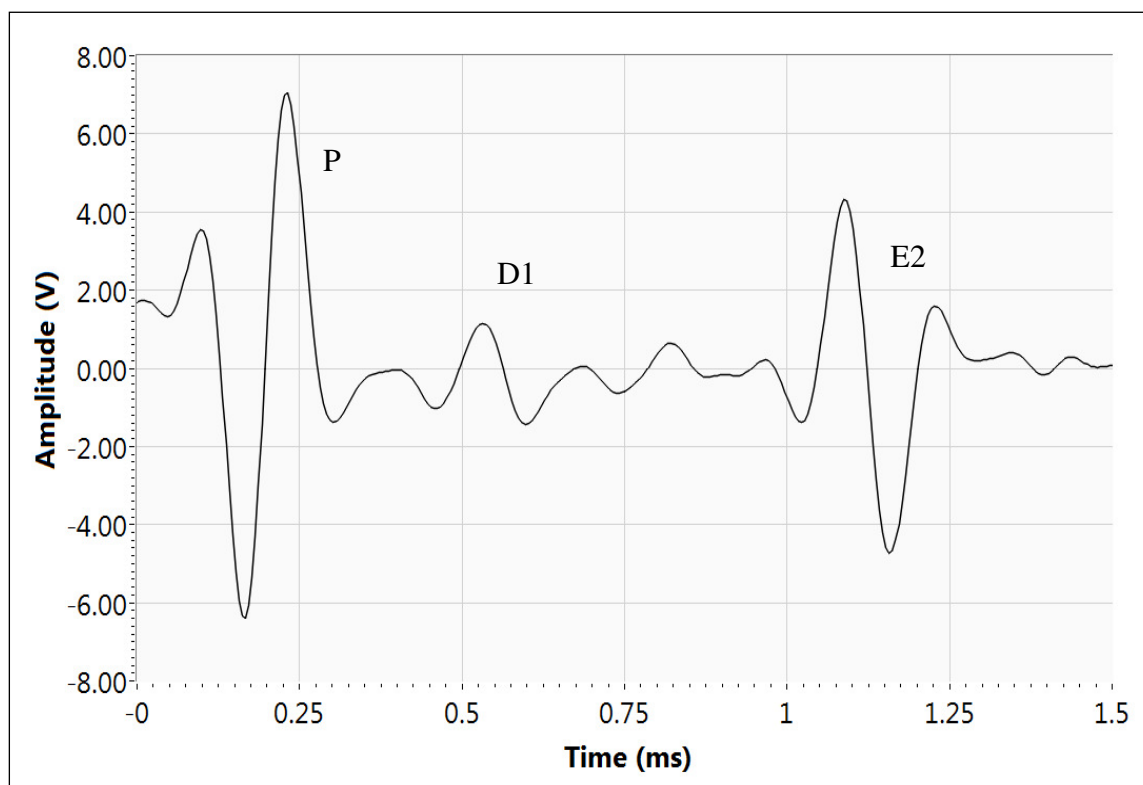
Figure 5.32 Wave reflections from the 13-strand anchorage area with three-broken-strand defect. P is the initial transmitted pulse; D1 is the signal reflection from the defect. E1 is the reflection from the near-side end of the strand

The experimental results in the previous sections have shown that the MFL method is capable of detecting loss of section due to corrosion defects of varying sizes. The results on a real cable have shown that the MFL is capable of detecting corrosion defects inside the cable; the defects range from a single broken wire to several broken wires. Considerable success has been achieved in detecting steel defects from a single broken wire to seven broken wires (full strand fracture), particularly at the surface of the steel (about 1.5 in. depth from the surface of the cable). However, limited success has been achieved in detecting defects at the center of the steel cable, limited to detecting the 7 broken wires defect only. This suggests increasing the strength of the magnetic field to ensure that sufficient flux lines reach to the center of the cable or using magnetic sensors with higher sensitivity. Also, the prototype MFL system was built based on flat rectangular magnets and, unfortunately, it can only cover a portion of the circumference of the cable. As such, it is necessary to rotate the magnets around the cable and repeat the scans for the entire length of the cable several times to cover the full volume of the cable. The experiments were carried out on single isolated defects (defects that are far from each other). However, when defects were very close to each other, it was difficult to visually distinguish the MFL signal for each individual defect. For example, the presence of a large defect next to relatively small defect may mask the signal from the small defect, which may alter the shape of the signal of the large defect. This may suggest the need for more sophisticated signal processing or pattern recognition techniques to improve defect detectability.

To verify the accuracy of the mathematical model of the MFL signal discussed in chapter 3, the MFL signals obtained from the different sizes of defects were compared to the mathematical model. The comparison showed that signal shape from the defects is in agreement with the mathematical model. An example of MFL signal acquired from one of the tests and the signal obtained from the mathematical model from equation (3.2) is shown in Figure 5.33.
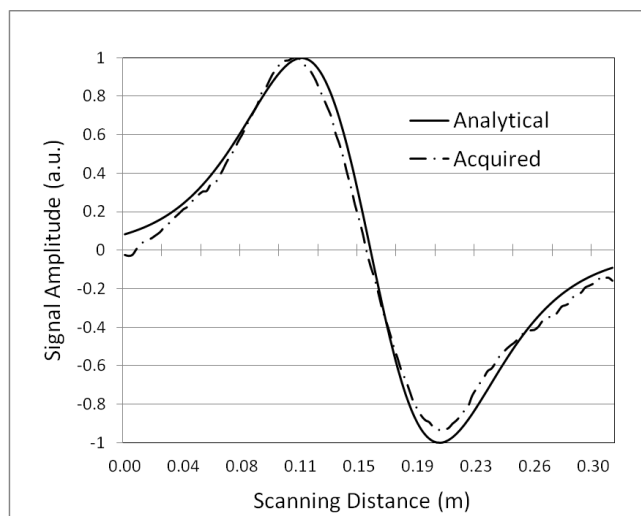
Figure 5.33 Acquired MFL signal and predicated signal based on the mathematical model in equation (3.2).

Also, comparing the shape of the MFL signal obtained from different sizes of defects, but the same type (cylindrical), shows that the shape of the signal is very similar; the peak-to-peak magnitude of the signal and the peak-to-peak distance is slightly different, but the overall shape of the signal is almost identical. This suggests that the MFL is capable of producing a unique shape of signal that is unique to the shape of the defects.

Similar to the MFL experiments, a considerable success using the MS method has been achieved in detecting steel defects from a single broken wire to seven broken wires on one strand sample. The MS results showed clearly the reflections from the end of the wire/strand as well as the reflections from the defects. The MS experiments carried out on a similar anchorage area of 13 strands showed that the MS is capable of detecting steel defects from a single to several broken strands. However, it was difficult to visually distinguish the signal reflection from the near-end of the cable and signal reflected from defects that are very close to the end of the cable. This may suggest increasing the frequency of the transmitted signal to improve spatial resolution. However, increasing the frequency may increase the signal attenuation considerably due to skin-depth effect; if a conductor is carrying an alternating current, the current tends to flow at the surface of the conductor and the magnitude of the current decrease exponentially with the conductor depth. The results from the experiments have also showed that no significant attenuation of the transmitted signal has been observed. This is not necessarily the case in a real cable; steel in a real anchorage area of a cable is usually covered with grout or oil type of material. The MS signal interaction at the boundary of the material and the steel could have significant attenuation effect, especially if the transmitter coil of the MS system is placed far away from the anchorage area. The MS signals obtained showed signal reflections from the defects and the anchorage area side of the cable, but it also showed the signal reflections from the far end of the cable. On a real cable this may not necessarily be the case, as the far end of the cable is further away from the anchorage area. However, the presence of defects on the far side of the cable may result in signal reflections that appear on the MS data. This makes it difficult to distinguish the location of the defect and may lead to miscalculation of the exact location of the defect. As such, a

more sophisticated arrangement of the transmitter coil is necessary to control the directivity of the MS signal (i.e., allow the MS signal to be transmitted in the direction of the anchorage area, while inhibiting the signal from travelling in the opposite direction). Also, comparing the shape of the MS signal obtained from different sizes of defects, but same type (cylindrical), it's clear that the shape of the signal is very similar and related to the transmitted signal; the peak-to-peak magnitude of the signal and the peak-to-peak time is slightly different, but the overall shape of the signal is almost identical. This may suggest that the MS is capable of producing a unique shape of signal that is unique to the shape of the defects. When the number of transmitted pulses was increased from one to multiple pulses, an increase in transmitted energy was observed; however, the spatial resolution suffered considerably, as seen Figure 5.24.

To verify the accuracy of the mathematical model of the MS signal discussed in chapter 3, the MS signals obtained from the different sizes of defects were compared to the mathematical model. The comparison showed that the signal shape from the defects is in agreement with the mathematical model. An example of an MS signal acquired from one of the tests and the signal obtained from the mathematical model from equation (3.14) is shown in Figure 5.34.
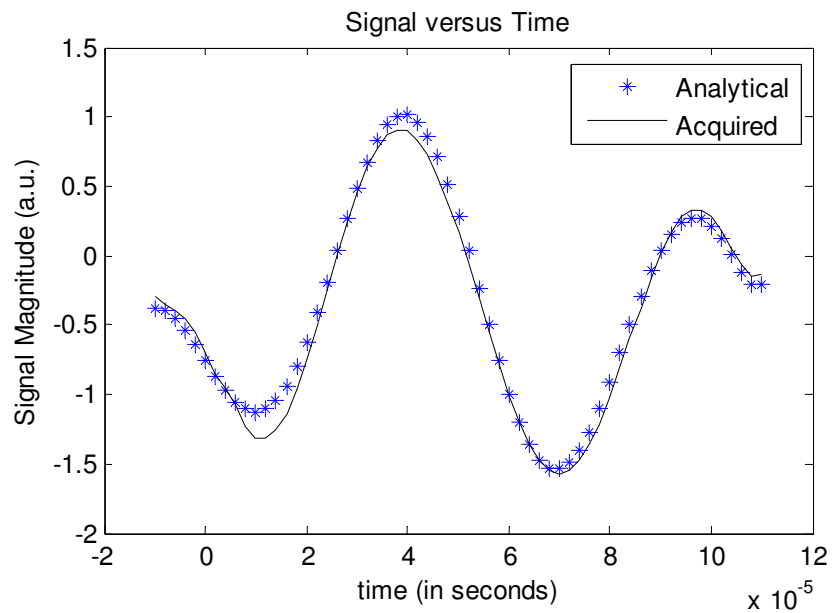
Figure 3.34 Acquired MS signal and predicated signal based on the mathematical model in equation (3.14).

The results from the MFL experiments and MS experiments have been compared to

similar type of work [30, 46-51, 79, 80, 81, 82] and the results are in agreement.

However, the magnitudes of signals obtained are different due to difference in setup and

system parameters.

CHAPTER 6

PROPOSED SYSTEM DESIGN

6.1 Introduction

As shown in the previous chapter, a considerable level of success can be achieved in detecting steel defects using the Magnetic Flux Leakage (MFL) and the Magnetostrictive (MS) methods. A prototype MFL system based on a set of flat rectangular magnets was used in this study to perform the required experiments. However, the flat magnets can only cover a portion of the circumference of the cable. As such, it is necessary to rotate the magnets around the cable and repeat the scans for the entire length of the cable several times to cover the full volume of the cable. This is not practical in the field, especially for long bridge cables, where the length of the main cable may exceed 1,400 ft. To address this limitation, a new design layout for the magnet and sensors is proposed in this chapter. Also, proposed in this chapter is a system design that integrates both the MFL and the MS methods.

6.2 Proposed System Design

The proposed system design is based on using circular magnets that encapsulate the cable with Hall-effect sensors that are arranged along the circumference of the cable, as seen in figure 6.1. The magnets will not only provide a complete coverage of the circumferences of the cable, but it will also provide a uniform magnetic field as well. Also, the shown arrangement of the Hall-effect sensors will provide a 360° field of view for the detection

of magnetic flux fluctuations due to the presence of defects in the cable. The circular magnets will not only provide the static magnetic field needed for the MFL method, they will also serve as the bias magnets that are needed for the MS method. Similarly, the Hall-effect sensors could have a dual-use, where they can detect both the MFL and MS signals.
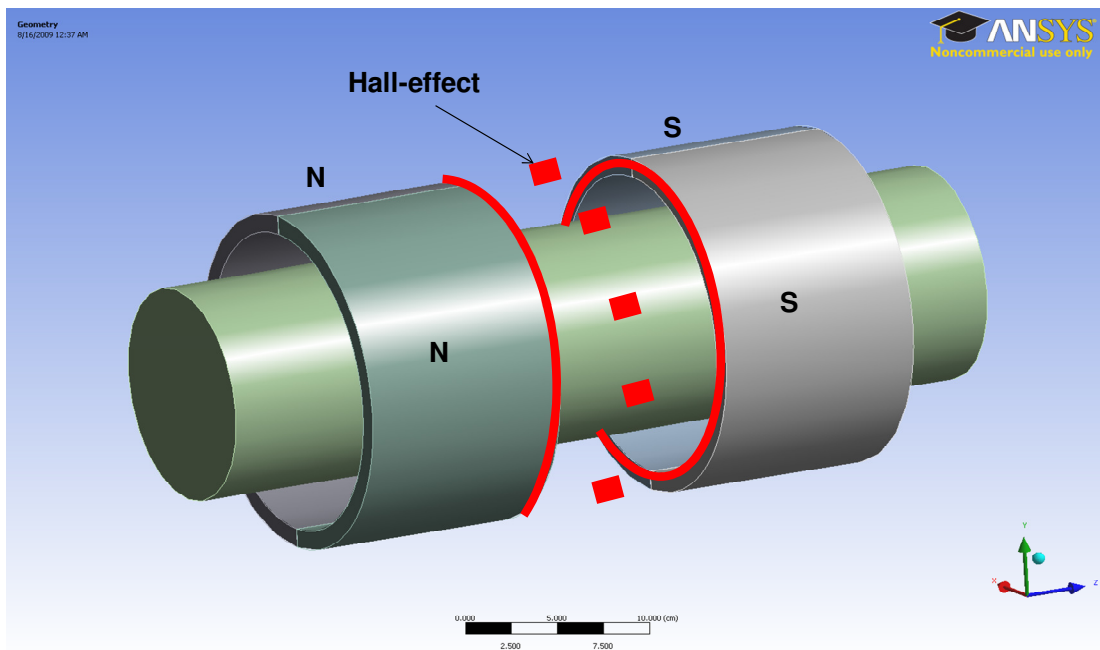
Figure 6.1 Integrated MFL/MS System; arrangement of MS coils and Hall-effect sensors with the circular magnets

6.3 Proposed Circular Magnets Design

The permanent magnets assembly of the proposed system in this research consists of two main parts: two pairs of half-circular magnets and a cylindrical steel sleeve that connects the magnets together, as seen in figure 6.2 The proposed magnets geometry is intended to wrap around the steel cable for practical operation and optimal magnetization of the bridge cables.
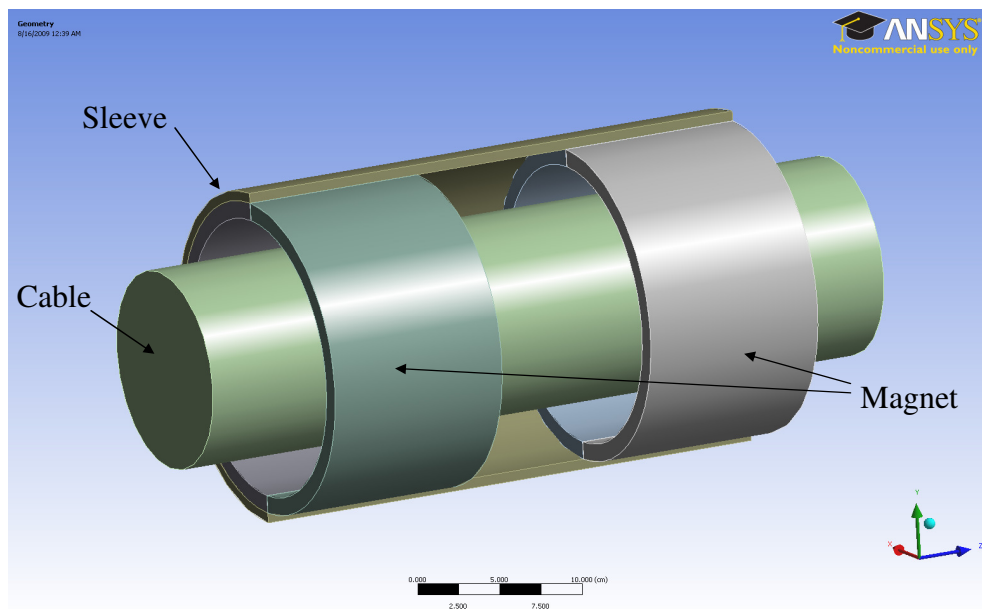
Figure 6.2 Permanent Circular Magnets Layouts.

This arrangement and orientation of the magnets provide the best continuous and uniform coverage of the magnet field around the bridge cables and an optimal linearity of the magnetic flux inside the cables. Each adjoining pair of magnets have the same magnetization polarity. The second pair of magnets has a similar arrangement, but with

an opposite magnetization direction to the first pair. In other words, the magnetization direction in the first pair of magnets is such that the north pole is at the inner surface and the south pole is at the outer surface of the magnets. The second pair of magnets has an opposite polarity, where the south pole is at the inner surface and the north pole is at the outer surface of the magnets. With this arrangement, the magnetic flux direction is oriented and concentrated in the Z-direction (i.e. inside the cable along the longitudinal direction). Each half-circular magnet will be made of N4516 Grade Magnetic Neodymium Iron Boron Nd-Fe-B material. The B-H curve for the proposed magnets is shown in Figure 6.3 [21]. B is the magnetic flux density in Guass (G) and H is the magnetic field strength measured in Orestad (Oe).
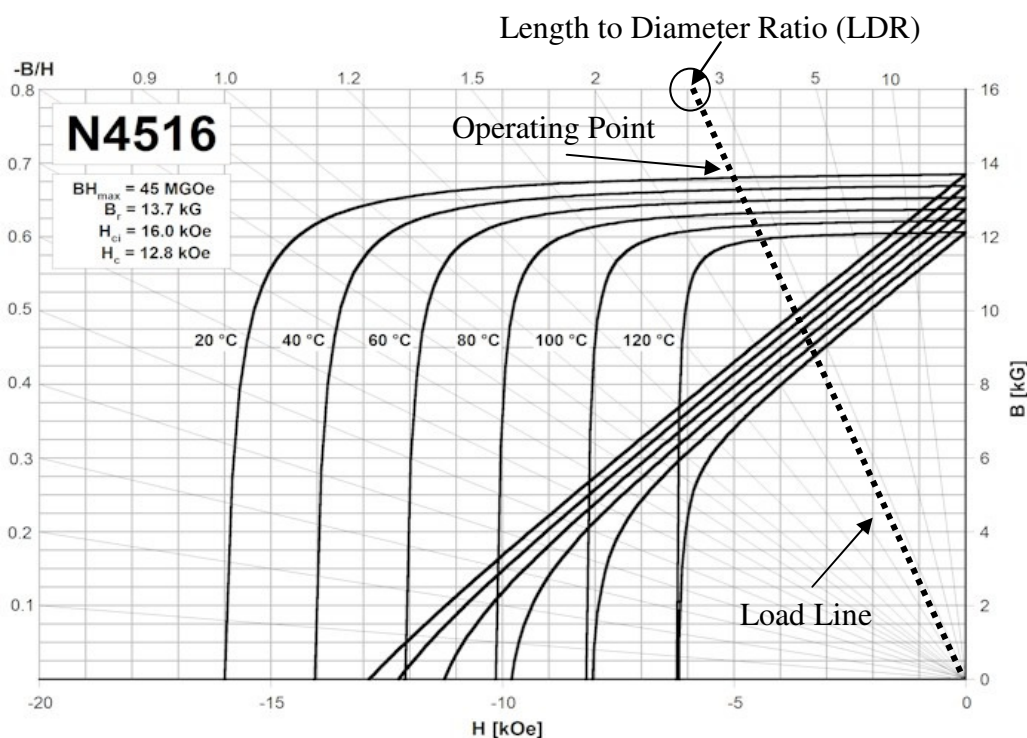
Figure 6.3 Typical H-B curves for the permanent magnets proposed in this study

The above B-H curve clearly demonstrates that the relationship between the B and H is not a linear one and that the performance of the magnets differs based on the environmental conditions, such as the temperature. The calculated H and B values for the system is approximately 5,000 Oe and 14,000 G respectively, based on the operating point and load line of the system, as shown in figure 6.3. The working point is the point on the BH curve where the values of B and H correspond to the actual working condition of the magnet. The load line is drawn starting from the origin of the BH curve and ending at the operating point. The length-to-diameter ratio (LDR) of the magnet is used to establish the load line and operating point. Operating temperature of 68° F is assumed. The length-to-diameter ratio of the system is calculated as follows:

LDR= L/D = 13 in/4.5 in = 2.89

Where,

L = the length of the magnet system (in)

D = the diameter of the magnet system (in)

The conceptual design of the magnets is shown in Figure 6.4. Factors that have been taken into consideration for the system design are size, weight, strength, layout and workflow, such that an optimal design can be achieved. Also, the design included provisions to ensure that a homogenous induced magnetic field could be achieved at any time inside the bridge cable between the two magnet pairs. This is important, as it allows accurate measurements of the magnetic field variations due to the presence of defects in the bridge cables.
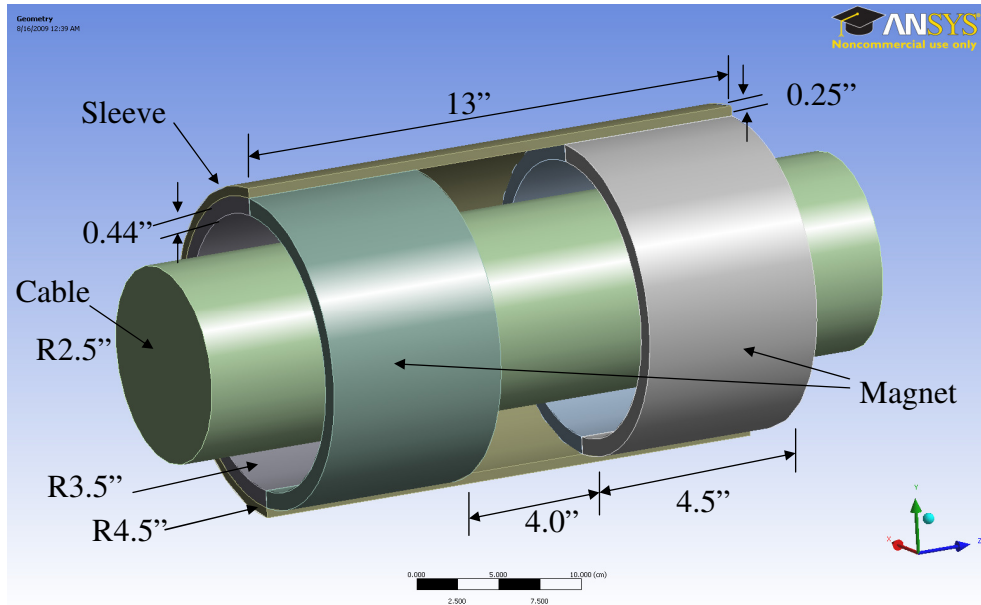
Figure 6.4 Conceptual design of the magnet

The proposed MFL system design was achieved based on performing a numerical simulation using the ANSYS finite element software. The simulation modeling is based on assuming closed circular-magnets arranged around the steel cable with a steel sleeve. No gap has been included in the model between the edges of the magnet pieces. During the actual system assembly a small gap at the edges of the magnets may be present as mechanical devices and hinges will be used to bring together and hold the magnet pieces in place. ANSYS is a commercially available software suite that is used for modeling and analyzing engineering problems based on the Finite Element analysis method. The software is capable of performing different types of analyses such as electromagnetic, static magnetic, structural stress, thermal, fluid, and other types.

The geometric models for the MFL system were created in AutoCAD for ease of use and editing. The models were then imported to ANSYS for static magnetic field analysis.

Figures 6.5 to 6.11 show the results of the numerical analysis for the proposed MFL system based on using lightweight permanent magnets. Figures 6.9 to 6.11 show homogenous magnetic field density (B) of 6,800 G within the field of view (FOV) of the magnets. FOV is the area between the magnets where magnetic field is homogenous (variations in the B values is less than 10%). The B value (6,800 G) is calculated based on averaging the maximum and minimum values of the field, within the FOV.
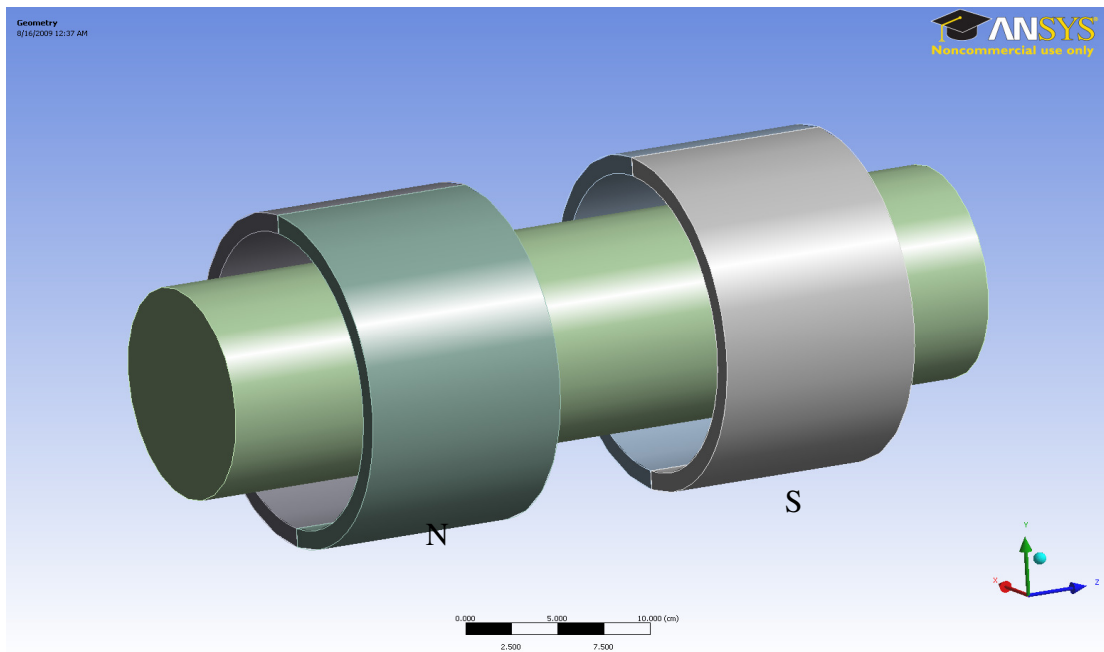
Figure 6.5 Magnets without the sleeve and showing magnetization direction
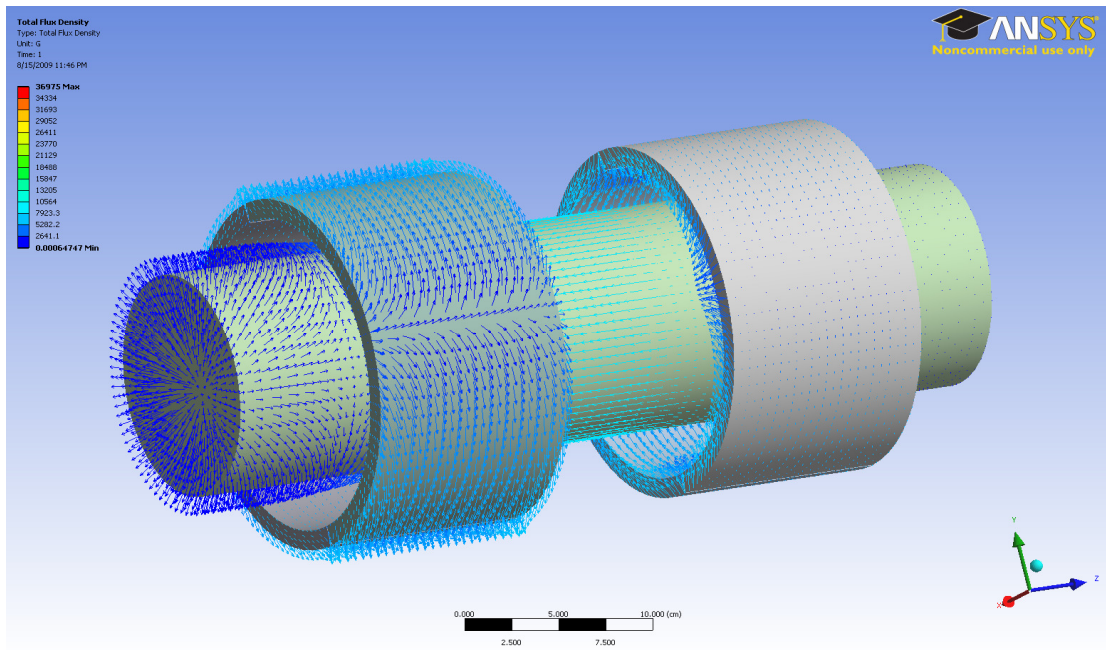
Figure 6.6 Magnets; showing the flow direction for the magnetic flux (B)
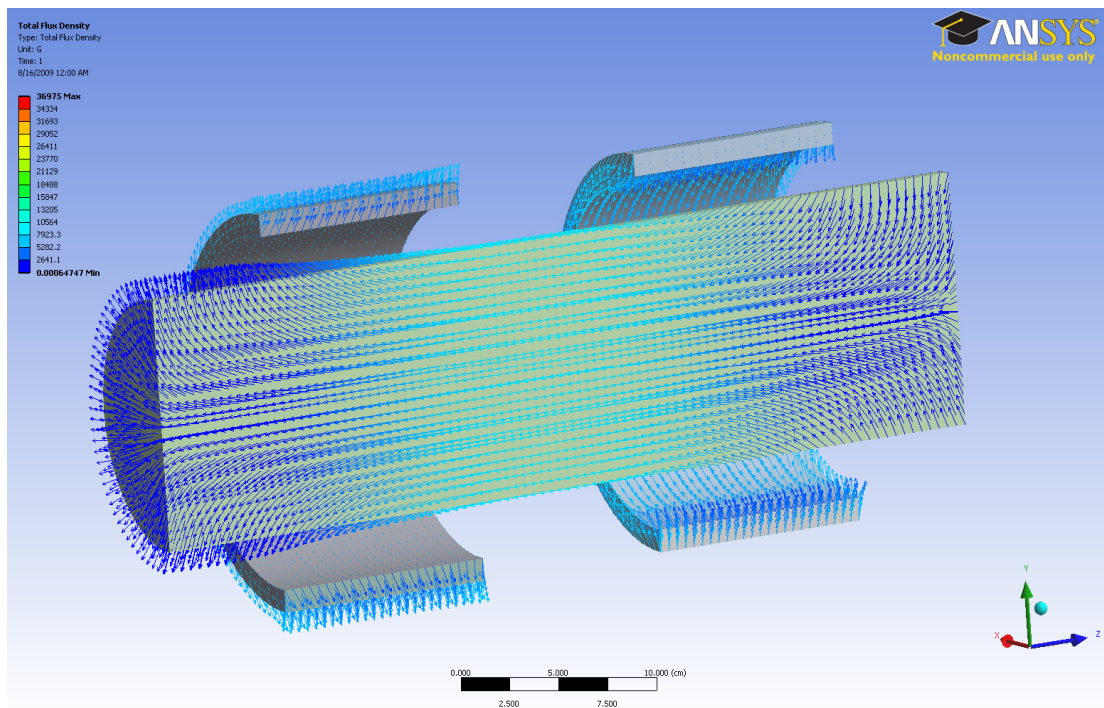
Figure 6.7 Magnets; showing the direction of the magnetic flux (B) inside the cable along the longitudinal direction
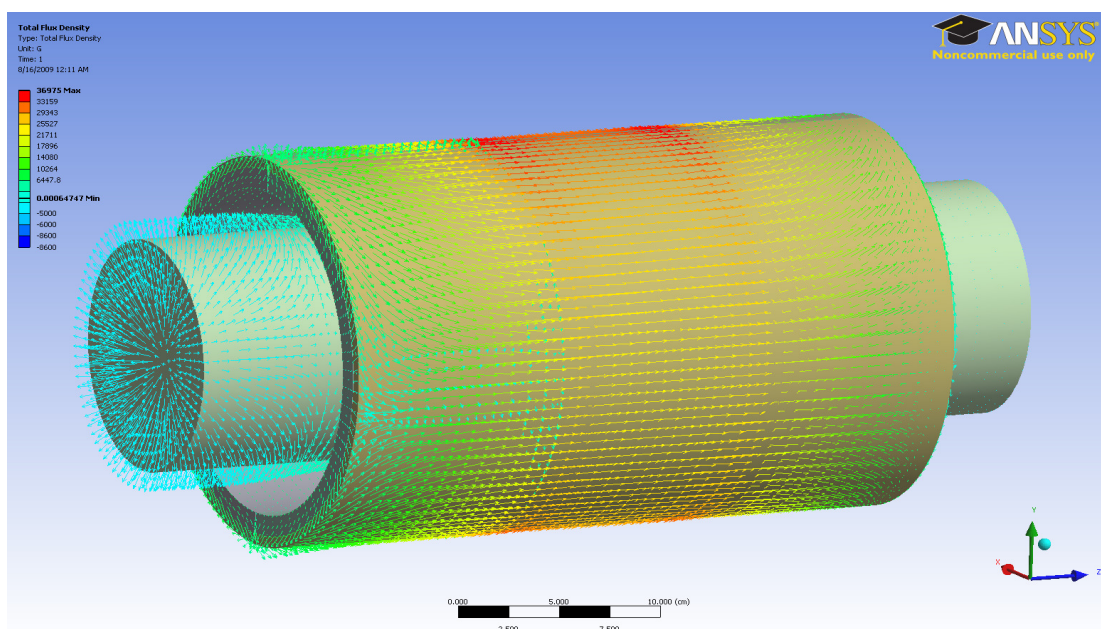
Figure 6.8 Magnets; showing the direction of the magnetic flux (B) on the surface of the sleeve
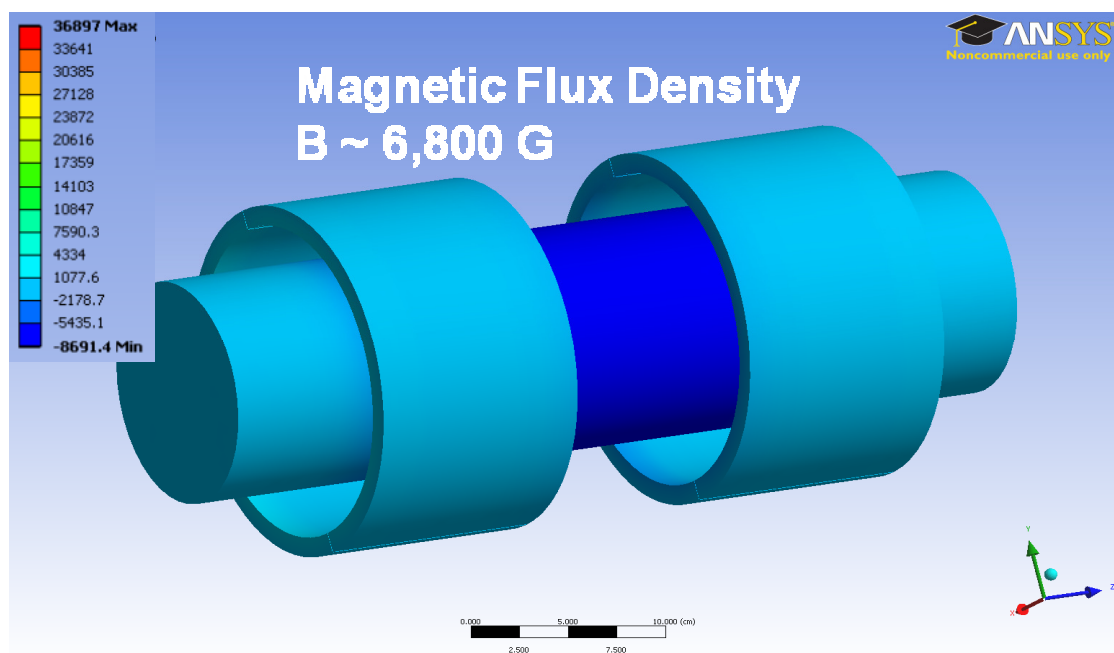
Figure 6.9 Magnets; showing the total flux density (B). The B value (6,800 G) is calculated based on averaging the maximum and minimum values of the field, within the FOV.
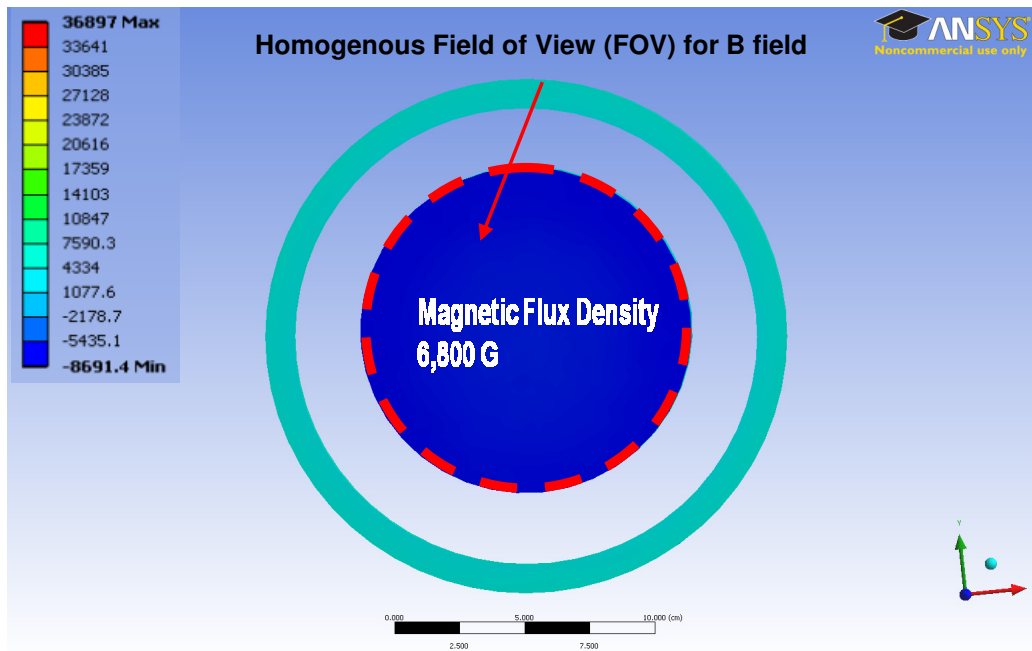
Figure 6.10 Magnets; showing homogeneity of the magnetic flux (B) in the Z direction, within the field of view - cross sectional view is shown
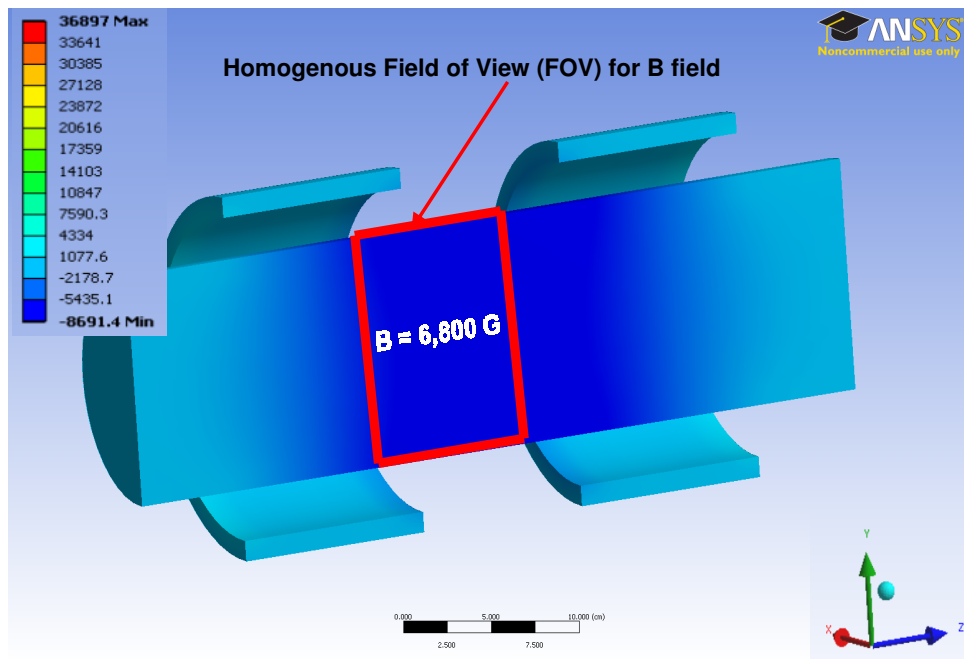
Figure 6.11 Magnets; showing homogeneity of the magnetic flux (B) in the Z direction, within the field of view - longitudinal sectional view is shown

The flaws in the steel cable have been modeled as cross-sectional losses of the steel core with different diameter as seen in Figure 6.12 and 6.13. These modeled flaws have been used to simulate physical losses of section in the steel cable. They have also been used to analyze the magnitude of the magnetic flux generated due to the presence of these flaws in the steel. The results were used to determine various design parameters and performance requirements for the sensors to detect magnetic flux leakage due to the presence of defects in steel cables.
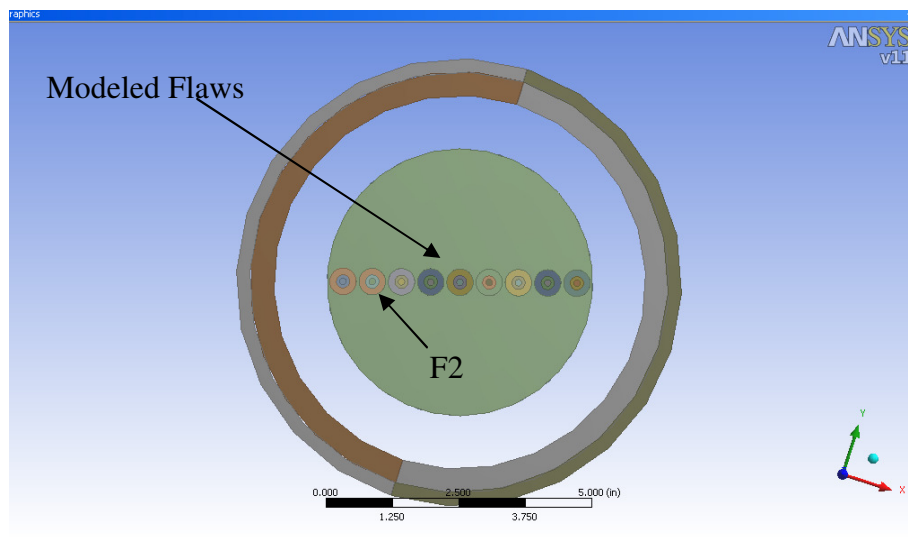
Figure 6.12 Magnets; showing different sizes of flaws and locations inside the cable-cross sectional view is shown
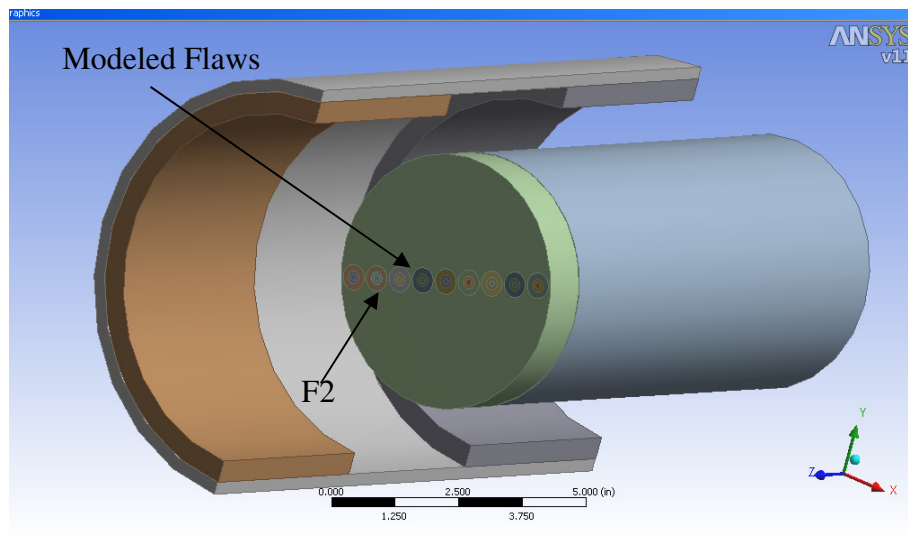
Figure 6.13 Magnets; showing different sizes of flaws and locations inside the cable-longitudinal sectional view is shown

The numerical simulation results for 7-wire broken strand, 5-wire broken strand, 3-wire broken strand and 1-wire broken strand modeled flaws are shown in Figures 6.14-6.17 respectively. The location of the flaw (F2 labeled on Figures 6.12 and 6.13) has been kept at 1.5 in depth from the surface of the cable. The analyses show that the maximum magnetic flux density for 7-wire broken strand flaws is 18.21 G. The maximum magnetic flux density for 5-wire broken strand flaw is 14.13 G. Figure 6.16 shows the flux density for 3-broken wire flaw with maximum magnitude of 7.06 G. The result of the simulation for 1-broken wire shows magnetic flux density with 1.2G maximum magnitude. Performance gain of using the proposed system over the flat magnets has been calculated. The magnetic flux density for 7-broken wire obtained in chapter 5, Figure 5.1(d), has been calculated using known system electronic signal gain and sensitivity of the Hall-effect sensor as follows:

Hall-effect sensor sensitivity = 10 uV/G

The electronic circuit gain (signal amplification) = 14000

Maximum signal amplitude from Figure 5.1 (d) = 0.9 V

The magnetic flux density can be calculated as follows:

Flux density = signal amplitude (V)/[signal gain/Hall-effect sensor sensitivity (uV/G)]

Flux density = 0.9 V/[14000/(10 uV/G)] = 6.43 G

Performance gain = 18.21 G/6.43 G= 2.83

The proposed system provides performance gain by a factor of 2.83, which is expected to provide better sensitivity to detect smaller flaws.
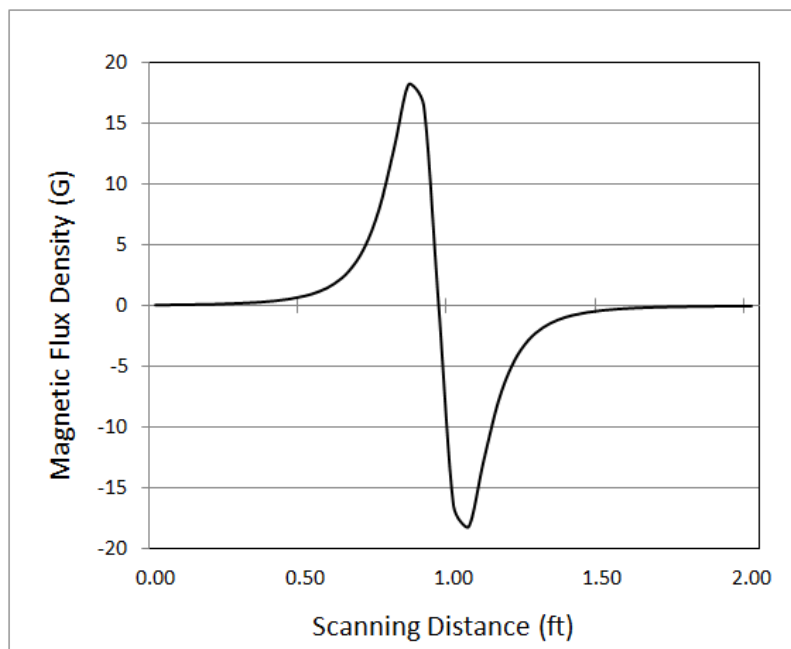
Figure 6.14 Magnetic flux density of MFL signal for 7-wire broken strand
simulated flaw
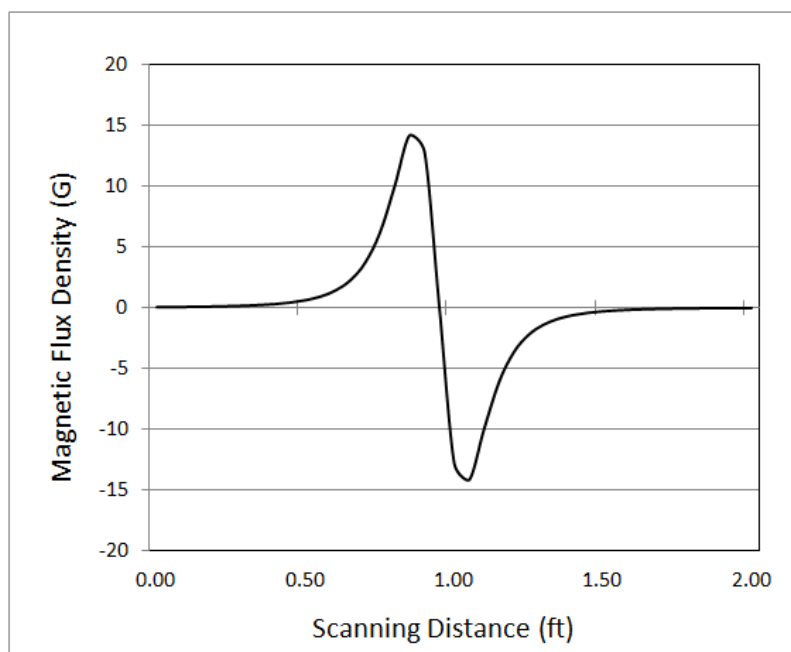
Figure 6.15 Magnetic flux density of MFL signal for 5-wire broken strand
simulated flaw
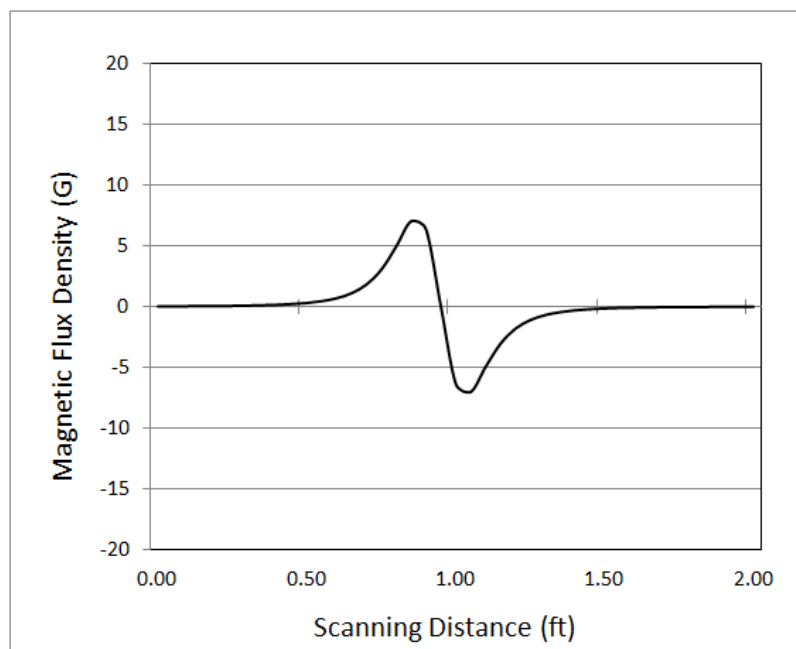
Figure 6.16 Magnetic flux density of MFL signal for 3-wire broken strand
simulated flaw
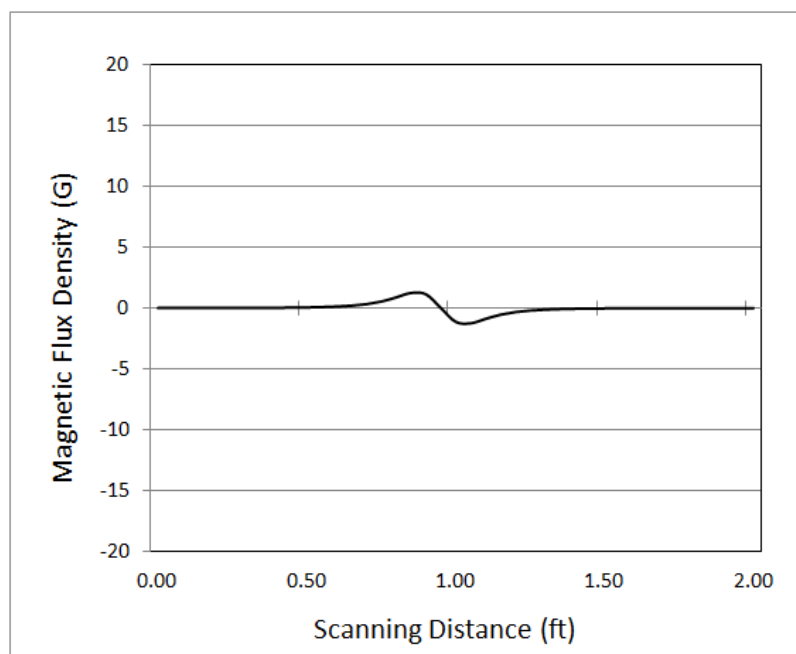
Figure 6.17 Magnetic flux density of MFL signal for 1-wire broken strand
simulated flaw

6.4 Proposed MS System Design

The high level block diagram and the system components of the proposed MS system are shown in figure 6.18. The MFL/MS system installation on the cable is shown in figure 6.19. In this setup, an electrical wire wound around the bridge cable is used as a transmit/receive coil. The oscillator function is to generate the RF electrical excitation signal with the desired frequency, magnitude and duration. The signal is then fed to a power amplifier. The amplifier is used to drive the transmit/receive coil. The RF switch function is to route the excitation RF pulse to the transmit/receive coil during the transmission state and to route the signal reflections from the cable during the receive state. The received signals are routed through the receive chain (a pre-amplifier, data acquisition hardware in a laptop) to amplify, filter and improve the signal-to-noise ratio (SNR). A pre-amplifier is a small electronic device that boosts the amplitude of a small electrical signal several times and it is usually placed near the source of the electrical signal to reduce the effects of electrical interference and noise background. SNR is a measure of signal strength relative to a background noise. SNR is usually measured in decibels (dB) according to the following:

$$SNR = 20 \log_{10}(V_s/V_n)$$

Where V_s *is the magnitude of the measured electrical signal and* V_n *is the magnitude of the noise background.*

Another option for receiving the RF signal from the cable is to use the Hall-sensors proposed in the MFL system. The Hall-effect sensors are arranged in a circular fashion around the contour of the magnets with dual functionality; detecting signals from the MFL system when the system is used on the main cable of the bridge and detecting signal

reflections in the MS system when the system is used to inspect the cable within the anchorage area.
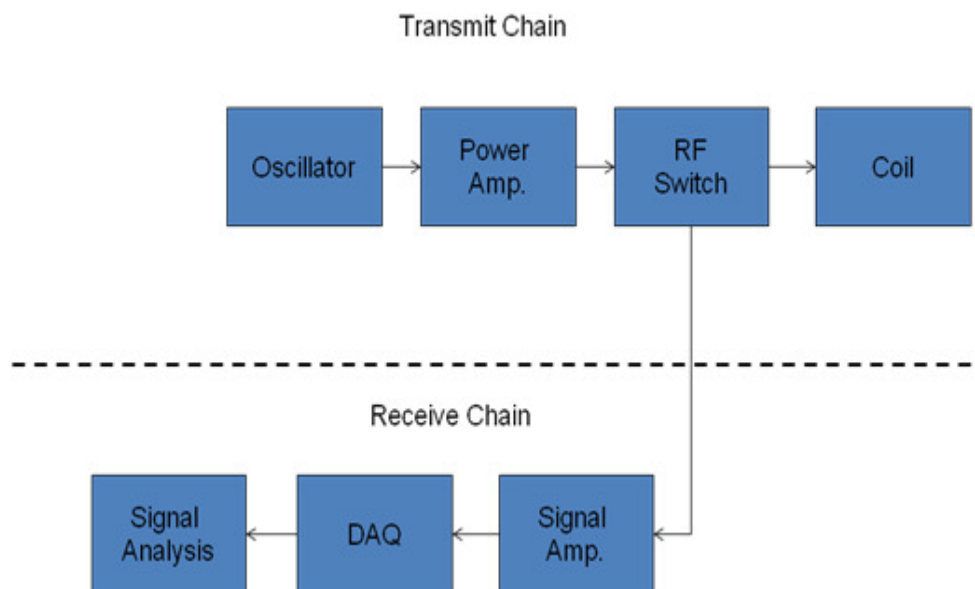
Figure 6.18 MS System Block Diagram
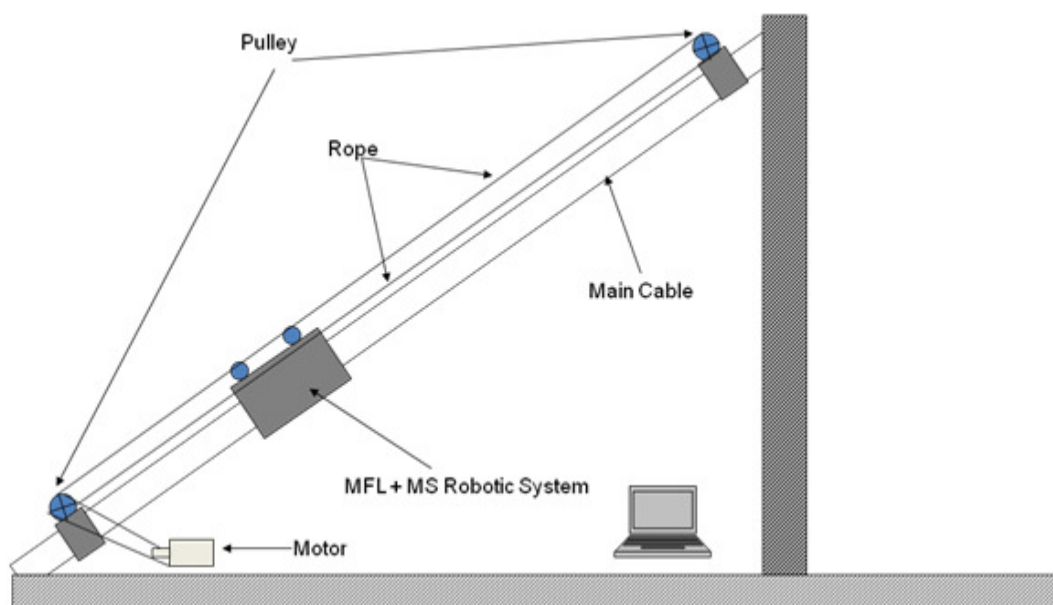
Figure 6.19 System installation on a cable of Cable-Stayed Bridges

The numerical analyses have shown that a uniform magnetic field of about 6,800G could be achieved using the proposed design with a minimum size (13 in length, 9 in diameter) and weight (50 Ib) to maintain a practical design. Additionally, hinges can be used to connect the two halves of the magnet, as shown in Figure 6.20. The hinges facilitate opening and closing the magnet, while installing it on the cable. The hinges also provide a means to lock the magnet. Once the magnet is secured on the cable a system of pulleys, ropes and a motor can be used to move the magnets along the entire length of the cable during inspection using the MFL method. The system can be placed at the end of the cable to use the MS method to inspect the cable-anchorage area.
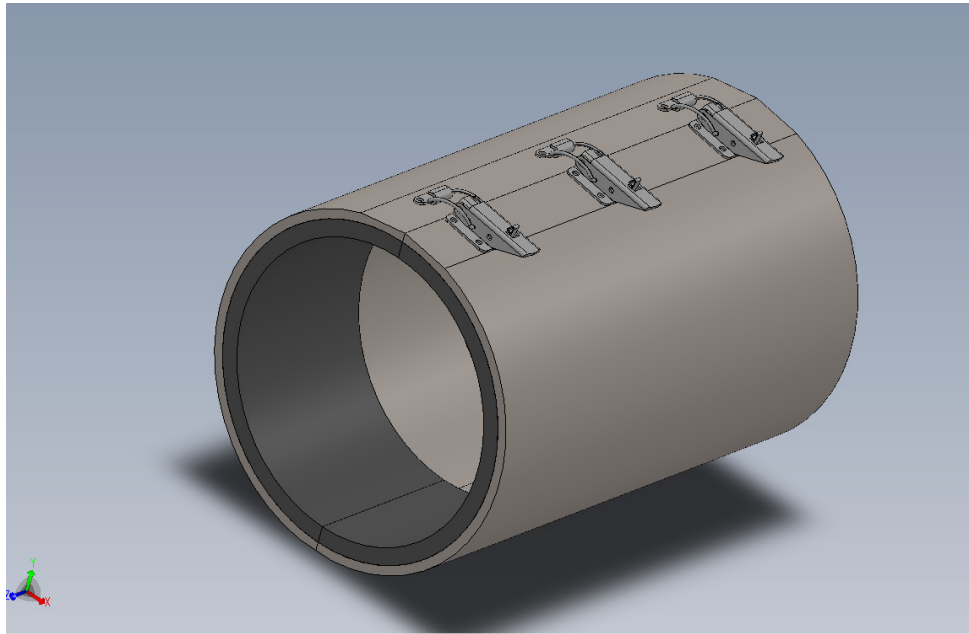
Figure 6.20 Proposed System: magnets are connected using hinges to allow opening and locking the magnet on the cable.

CHAPTER 7

CONCLUSION and RECOMMENDATIONS for FUTURE WORK

7.1 Summary of Objectives and Achievements

The research presented in this thesis is motivated by the need to design a non-destructive evaluation system based on Magnetic Flux Leakage (MFL) and Magnetostrictive (MS) methods to detect steel loss of section, i.e., from corrosion, in cables of cable-stayed and other types of bridges. It is necessary to be able to detect complete fractures, partial fractures and loss of section due to corrosions in bridge cables. It is also necessary to be able not only to inspect the entire free length of the bridge cables, but also to be able to inspect the cable length within the anchorage area. As such, this thesis has demonstrated the feasibility of using the MFL and MS techniques to detect loss of section in bridge cables and has provided a proposed design for a non-destructive evaluation system based on the combined MFL and MS techniques. The proposed design will enable bridge engineers to perform complete inspection of the bridge cables for both the free length and for the cable length within the anchorage area. The proposed MFL method uses permanent magnets wrapped around the cable to magnetize the steel inside the cable. The system uses Hall-effect sensors to detect fluctuations in the magnetic field that are due to loss of section in steel cables, such as broken wires and sectional losses due to corrosions.

The MFL system will be moved along the free length of the main cable of the bridge or scanning the cable for section losses due to fracture of corrosion. This will allow for inspection of the entire free length of the cable except in the anchorage area since the cable is embedded within concrete and it is not accessible. Accordingly, the MS method, is used for the inspection of the cable within the anchorage region. The MS method introduces a guided wave into the cable within the anchorage area while monitoring wave reflections from the cable end as well as from any section losses due to corrosion or fracture.

7.2 Magnetic Flux System

The use of MFL method has been studied and evaluated for detecting section losses in the bridge cables through experimental work as shown in chapters 4 and 5. A prototype model of the MFL system has been used. The prototype model includes a pair of permanent magnets, a mechanical frame and a Hall-effect sensing unit. Also, data acquisition hardware for signal amplification and conditioning has been developed. Furthermore, data acquisition software for real-time acquisition and post-processing analysis has been developed. A grouted 5-inch diameter bridge cable that consists of pre-stressing strands has been used for the MFL experiments to evaluate the system performance. The experimental results are shown in chapter 5. The results have shown that the MFL technique is capable of detecting corrosion-related defects (section loss) inside the cable. These include a single broken wire within one strand to several broken strands. Considerable success has been achieved in detecting steel section losses from a single broken wire to 7 broken wires (or a complete strand fracture), particularly when the section loss is in a strand near the outer surface of the cable (or within about 1.5 in

from the surface of the cable). However, successful section loss detection at the center of the steel cable has been limited seven broken wires. The current MFL system built based on flat rectangular magnets can only cover a portion of the circumference of the cable. As such, it is necessary to rotate the magnets around the cable and repeat the scans for the entire length of the cable several times to cover the full volume of the cable. This is not practical in the field, especially for long span bridges where the length of each bridge cable may exceed 1,400 ft. To address this limitation, a new design has been proposed in chapter 6. The new design is based on using two pairs of cylindrical magnets that encapsulate the cable with Hall-effect sensors that are arranged around the circumference of the cable. It is important for the new magnet design be able to penetrate the entire cross section of the cable and be able to provide uniform magnetic field. Several physical models were studied using numerical analysis and several trade-offs have been made to propose a practical design layout. The final results of the numerical analysis are provided in chapter 6. The numerical analyses have shown that a uniform magnetic field of about 6,800G could be achieved using the proposed design with a minimum size (13 in length, 9 in diameter) and weight (50 Ib) to maintain a practical design. Additionally, hinges can be used to connect the two halves of the magnets, as shown in Figure 6.20. The hinges facilitate opening and closing the magnet while installing it on the cable. The hinges also provide a means to lock the magnet. Once the magnet is secured on the cable a system of pulleys, ropes and a motor can be used to move the magnets along the entire length of the cable during inspection using the MFL method.

7.3 Magnetostrictive System

The use of the MS method has been studied and evaluated for detecting cable section losses in the anchorage area through experimental work as provided in chapters 4 and 5. A prototype model was built that was comprised of transceiver coils, power amplifiers, preamplifiers and signal conditioning circuits. Transmitter/receiver coils were designed and built to send and receive guided waves/pulses within the cable. An RF amplifier was built and used to amplify the RF signal from a wave generator before transmitting the RF pulses. Also, preamplifiers and data acquisition hardware were developed to acquire and amplify the reflected pulses. Further, the data was viewed on a laptop computer for real-time inspection and it was stored for further processing. Several test samples were created to aid in evaluating the MS method. These included an 8-foot single steel strand (7-wires), simulated anchorage-area using a single strand, simulated anchorage-area using 13 strands and an 8 ft bridge cable. The RF pulse magnitude, number of cycles and frequency of the RF pulse were studied. The experimental results in chapter 5 have shown that the MFL method is capable of detecting section losses due to corrosion in a single strand and multiple strands in the free length of bridge cables. The MS technique demonstrated that it could clearly detect reflections from the end of the wires/strands as well as the reflections from the fabricated section losses in wires and strands. The MS experiments carried out on the simulated anchorage-area of 13 strands showed that the MS is capable of detecting steel section losses from a single to several broken strands. However, it was difficult to visually distinguish between the pulses that were reflected from the ends of the strands/cables and those from reflections caused by section losses that were located near the end of the cable.

7.4 Future Work

This thesis demonstrated the feasibility of using MFL and MS methods for detecting steel section losses in bridge cables. The results of both methods are very encouraging. However, the two methods can be further examined and the research can be further enhanced. For future work it is proposed to investigate the use of RF pulses with higher frequencies to improve inspection resolution, hence, detecting smaller section losses that are located near the end of the cables within the anchorage-area. However, other research has shown that increasing the RF pulse frequency will introduce challenges with increasing signal attenuation. It is also proposed to investigate the effect of section losses that are located nearby on the overall signal detection, in particular when a small defect is located near a large defect. Furthermore, the use of advanced signal processing techniques, such as correlation analysis and pattern recognition, may aid in a more effective signal interpretation that can improve inspection results. A prototype system should be built based on the proposed design and tested on real bridge structure to demonstrate the effective use of the system for bridge cable inspection.

REFERENCES

[1] Florida Department of Transportation (FDOT) Report, "Post-tensioned Bridges", Topic No. 700-000-000, Section 10.7, October 21, 2004.

[2] A G Lichtenstein, "The Silver Bridge Collapse Recounted", TRB, Journal of Performance of Constructed Facilities, vol.7, p. 249-261, 11-1993.

[3] P. C. Ken, J. C. Nicholas, and W. Glenn, "Health Monitoring of Civil Infrastructures," Smart Materials and Structures, pp. 483, 2003.

[4] A. David, "Repairs without Rivets," in Scientific American Magazine, November 2007.

[5] R. Woodward, F. Williams, "Collapse of the Ynys-Y-Gwas bridge, West Glamorgan," proceedings of the institutional of Civil Engineering, vol.84, pp.635-669, 1988.

[6] D. Parker, "Pacific Bridge Collapse Throws Doubt on Repair Method," *New Civil Engineer*, pp.3-4, 1996.

[7] D. Parker, "Tropical Overload," *New Civil Engineer*, pp.18-21, 1996.

[8] Don E. Bray, Redoeric K. Stanley, Nondestructive Evaluation: A Tool in Design, Manufacturing, and Service, Revised Edition, CRC Press.

[9] Peter J. Shull, *Nondestructive Evaluation: Theory, Techniques, and Applications*, 2002 edition, Marecl Dekker.

[10] Charles J. Hellier, *Handbook of Nondestructive Evaluation*, 2001 edition, McGraw-Hill.

[11] Josef Krautkrämer, Herbert Krautkrämer, *Ultrasonic Testing of Materials*, 3rd edition, Spring-Verlog.

[12] Andrew Webb, *Introduction to Biomedical Imaging*, 2003 edition, Wiley-Interscience.

[13] M. G. Ali, A. R. Maddocks, "Evaluation of Corrosion of Prestressing Steel in Concrete Using Non-destructive Techniques", GHD Pty Ltd, Sydney.

[14] Leeming, M B, Lane, J S and Wade, P J, "Post-tensioned Bridge Investigation - The Way Forward", *Construction/Repair*, pp 193-197.

[15] Stain, R T and Dixon, 5, "Inspection of Cables in Post-tensioning Bridge - What Techniques are Available", *Construction/Repair*, January/February 1994, pp 297-300.

[16] Williams, H T and Hulse, M E, "From Theory to Field Experience with Inspection of Post-tensioned Bridges", *Construction/Repair*, pp 199-202.

[17] Nagi, M and Whiting, D, "Corrosion of Prestressed Reinforcing Steel in Concrete Bridges: State-of-the-Art", *Concrete Bridges in Aggressive Environments*, SP-15 1, ed. Weyers, R E, pp 17-41.

[18] Anon, "Inspection of Prestressing Cables in Bridges", *Indian Concrete Journal*, February 1987, Vol 61, No. 2, pp31-33.

[19] Oral Buyukozturk, "Imaging of Concrete Structures", *NDT & E International* 1998, Vol. 31, No.4 pp. 233-243.

[20] Price, W. I. J., "Highway Bridge Inspection: Principles and Practices in Europe", TABSE Symposium, Washington, 1982, Vol 38, pp 15-29.

[21] Martz, H E, Schneberk, D J, Roberson, G P and Monteiro, P J, "Computerized Tomography Analysis of Reinforced Concrete", *ACT Materials Journal*, May/June 1993, pp 259-264.

[21] Hillemeier, B, "New Methods in the Rehabilitation of Prestressed Concrete Structures", IABSE Symposium, Lisbon, 1989, Vol 57/1, pp 3 11-316.

[22] Flohrer, C. and Bernhardt, B., "Detection of Prestressed Steel Tendons Behind Reinforcement Bars, Detection of Voids in Concrete Structures - A Suitable Application for Radar Systems", International Conference on NDT in Civil Engineering, April, 1992, Vol 1, pp 227-234.

[23] Cheng, C. and Sansalone, M., "Effects of Impact-Echo Signals Caused by Steel Reinforcing Bars and Voids Around Bars", *ACT Materials Journal*, September/October, 1993, pp 421-434.

[24] Lin, Y. and Sansalone, M., "Detecting Flaws in Concrete Beams and Columns Using the Impact-Echo Method", *ACT Materials Journal*, July/August, 1992, pp 3 94-405.

[25] Pratt, D. and Sansalone, M., "Impact-Echo Interpretation Using Artificial Intelligence", *ACI Materials Journal*, March/April, 1992, pp 178-187.

[26] Carino, N.J. and Sansalone, M., "Detection of Voids in Grouted Ducts Using the Impact Echo Method", *ACT Materials Journal*, May/June, 1992, pp 296-303.

[27] Petersen, C. G., "Impact Echo Testing of the Injection of a Post-Tensioned Cable Steel Duct", *Report -German Instruments A/S*, September, 1993.

[28] Robert, J. L. and Brachet-Rolland, M., "Survey of Structures by Using Acoustic Emission Monitoring", IABSE Symposium, Washington, 1992, Vol 39, pp 33-38.

[29] Schupack, M., "Evaluation of Corrosion in Bonded and Unbonded Post-Tensioned Structures., How to make Today's Repairs Durable for Tomorrow", March 21, 1998, Houston, Texas.

[30] Steber, G. R., Ghorbanpoor, A. and Shew, T. E., "Magnetic Field Disturbance Signal Processing", Proceeding of IEEE Conference, 1989, Vol. 2, pp. 474-479.

[31] Ghorbanpoor, A. and Shew, T. E., "Detection of Flaws in Bars and Cables in Concrete Bridge Structures", *Transportation Research Record*, 1989, No. 1211, pp. 84-91.

[32] Gimmel, B., "Magnetoelastic Force Measurement in Prestressed Concrete", TABSE Symposium, Lisbon 1989, Vol. 57/1, pp. 329-334.

[33] Scheel, H. and Hillemeier, B., "Capacity of the Remnant Magnetism Method to Detect Fractures of Steel in Tendons Embedded in Prestressed Concrete", *NDT and E International*, 1997, Vol. 30, No.4, pp. 211-216.

[34] Fontana, M. G., "Corrosion Engineering", McGraw-Hill Book Company, 1986.

[35] Feliu, 5, Gonzales, J. A., Andrade, C. and Rz-Maribona, I., "Errors Introduced in the Guard Ring Device in the Onsite Measurement of Rebar Corrosion Rates", Corrosion of Reinforcement in Concrete, *Elsevier Applied Science*, 1990, pp. 293-302.

[36] John, D. G., Eden, D. A., Dawson J. L. and Langford, P. E., "Corrosion Measurements on Reinforcing Steel and Monitoring of Concrete Structures", Corrosion-87, Paper No. 136, San Fransisco, California.

[37] Green, W. K., "Electrochemical and Chemical Changes in Chloride Contaminated Reinforced Concrete Following Cathodic Polarization", Master of Science Dissertation, UTVHST, November 1991.

[38] Suresh Bapu, R. H., Nayak, N. U., Srividya Rajagopalan, C., Srinivasan, 5., Rengaswamy, N. S. and Mahadeva Iyer, Y., "Monitoring of Corrosion of Prestressing Steel Cables in Prestressed Concrete Bridges", Transactions of the SAEST, 1988, Vol. 23, No. 2-3, pp. 203-206.

[39] American Society for Testing Materials, "Standard Test Method for Half-Cell Potentials of Reinforcing in Concrete", ASTM Standards C876-80 and C876-87.

[40] Naish, C. C., Harker, A. and Carney, R. F. A., "Concrete Inspection: Interpretation of Potential and Resistivity Measurements", Corrosion of Reinforcement in Concrete, Elsevier Applied Science, 1990, pp. 314-332.

[41]. Escalante, E., "Effectiveness of Potential Measurements for Estimating Corrosion of Steel in Concrete", *Corrosion of Reinforcement in Concrete*, Elsevier Applied Science, 1990, pp. 28 1-292.

[42] Daniels, D., "Surface-Penetrating Radar", *Electronics and Communication Engineering Journal*, IEEE, 1996.

[43] Martz, H. E., Schneberk, D. J., Roberson, G. P. and Monteiro, P. J., "Computerized Tomography Analysis of Reinforced Concrete", *ACT Materials Journal*, May/June 1993, pp. 259-264.

[44] Carino, N., "The impact-Echo Method: An Overview", *NIST*

[45] M. Huang, L. Jiang, P. Liaw, C. Brooks, R. Seeley, D. Klarstrom, "Using Acoustic Emission in Fatigue and Fracture Materials Research", JOM, Nov. 1998, Vol. 50, No.11., http://www.tms.org/pubs/journals/JOM/9811/Huang/Huang-9811.html#ToC5.

[46] A. Ghorbanpoor, R. Borchelt, M. Edwards, and E. Abdel Salam, "*Magnetic-Based NDE of Prestressed and Post-Tensioned Concrete Members–The MFL System"*, Federal Highway Administration, Publication No. FHWA-RD-00-026, May 2000.

[47] A. Ghorbanpoor, G. R. Steber, and T. E. Shew, *"Evaluation of Steel in Concrete Bridges: The Magnetic Filled Disturbance (MDF) System"*, Federal Highway Administration, Publication No. FHWA-SA-91-026, May 1991.

[48] E. Abdelsalam, "Corrolation Analysis of Flaw Signal Detected by the MFD System", Master's thesis, University of Wisconsin-Milwaukee, December, 1998.

[49] Steber, G. R., Ghorbanpoor, A. and Shew, T. E., "Magnetic Field Disturbance Signal Processing", Proceeding of IEEE Conference, 1989, Vol. 2, pp. 474-479.

[50] Ghorbanpoor, A. and Shew, T. E., "Detection of Flaws in Bars and Cables in Concrete Bridge Structures", Transportation Research Record, 1989, No. 1211, pp. 84-91.

[51] "Magnetic Flux Leakage is Powerful New Force in Bridge Inspection", Engineering News-Record, *Equipment Tracks & Trends*; Vol. 244, No. 11; Pg. 35, March 20, 2000.

[52] S. Hoole, "Artificial Neural Networks in the Solution of Inverse Electromagnetic Field Problems," *IEEE Trans. Magn.*, Vol. 29, No. 2, pp.1931–1934, Mar. 1993.

[53] R. Sikora, T. Chady, and J. Sikora, "Neural Network Approach to Crack Identification," Int. J. Appl. Electromagn. Mech., Vol. 9, No. 4, pp.391–398, 1997.

[53] P. Ramuhalli, L. Udpa, and S. Udpa, "Neural Network Algorithm for Electromagnetic NDE Signal Inversion," in Electromagnetic Nondestructive Evaluation (V). Amsterdam, The Netherlands: IOS, 2001, pp. 121–128.

[54] R. Schifini and A. C. Bruno, "Experimental Verification of a Finite Element Model Used in a Magnetic Flux Leakage Inverse Problem," J. Phys. D: Appl. Phys., Vol. 38, No. 12, pp. 1875–1880, Jun. 2005.

[55] Z. Chen, G. Preda, O. Mihalache, and K. Miya, "Reconstruction of Crack Shapes from the MFLT Signals by Using a Rapid Forward Solver and an Optimization Approach," IEEE Trans. Magn., Vol. 38, No. 2, pp. 1025–1028, Mar. 2002.

[56] M. Yan, S. Udpa, S. Mandayam, Y. Sun, P. Sacks, and W. Lord, "Solution of Inverse Problems in Electromagnetic NDE Using Finite Element Methods," IEEE Trans. Magn., Vol. 34, No. 5, pp. 2924–2927, Sep. 1998.

[57] C. Mandache and L. Clapham, "A Model for Magnetic Flux Leakage Signal Predictions," J. Phys. D: Appl. Phys., Vol. 36, No. 20, pp. 2427–2431, Oct. 2003.

[58] D. Minkov, J. Lee, and T. Shoji, "Study of Crack Inversions Utilizing Dipole Model of a Crack and Hall Element Measurements," J. Magn. Magn. Mater., Vol. 217, No. 1, pp. 207–215, Jul. 2000.

[59] D. Minkov and T. Shoji, "Method for sizing of 3-D Surface Breaking Flaws by Leakage Flux," NDT&E Int., Vol. 31, No. 5, pp. 317–324, 1998.

[60] C. Edwards and S. B. Palmer, "The Magnetic Leakage Field of Surface Breaking cracks," J. Phys. D: Appl. Phys., vol. 19, no. 4, pp. 657–673, Apr. 1986.

[61] A. Joshi, L. Udpa, S. Udpa, and A. Tamburrino, "Adaptive Wavelets for Characterizing Magnetic Flux Lleakage Signals from Pipeline Inspection," IEEE Trans. Magn., vol. 42, no. 10, pp. 3168–3170, Oct. 2006.

[62] P. Ramuhalli, L. Udpa, and S. S. Udpa, "Electromagnetic NDE Signal Inversion by Function-Approximation Neural Networks," IEEE Trans. Magn., Vol. 38, no. 6, pp. 3633–3642, Nov. 2002.

[63] P. Ramuhalli, L. Udpa, and S. S. Udpa, "Neural Network-Based Inversion Algorithms in Magnetic Flux Leakage Nondestructive Evaluation," J. Appl. Phys., Vol. 93, No. 10, pp. 8274–8276, May 2003.

[64] W. Bandler, R. M. Biernacki, S. H. Chen, P. A. Grobelny, and R. H. Hemmers, "Space Mapping Technique for Electromagnetic Optimization," IEEE Trans. Microw. Theory Tech., Vol. 2, No. 12, pp. 2536–2544, Dec. 1994.

[65] J. W. Bandler, Q. S. Cheng, D. H. Gebre-Mariam, K. Madsen, F. Pedersen, and J. Søndergaard, "EM-Based Surrogate Modeling and Design Exploiting Implicit, Frequency and Output Space Mappings," in IEEE MTT-S Int. Microw. Symp. Dig., Philadelphia, PA, Jun. 2003, pp. 1003–1006.

[66] J. W. Bandler, Q. S. Cheng, S. A. Dakroury, A. S. Mohamed, M. H. Bakr, K.Madsen, and J. Søndergaard, "Space mapping: The State of the Art," IEEE Trans. Microw. Theory Tech., Vol. 52, No. 1, pp. 337–361, Jan. 2004.

[67] D. Echeverria and P. W. Hemker, "Space Mapping and Defect Correction," CMAM The International Mathematical Journal Computational Methods in Applied Mathematics, vVol. 5, No. 2, pp. 107–136, 2005.

[68] J. W. Bandler, S. Koziel, and K. Madsen, "Space Mapping for Engineering Optimization," SIAG/Optimization Views-and-News Special Issue on Surrogate/Derivative-Free Optimization, Vol. 17, No. 1, pp. 19–26, 2006.

[69] S. Koziel, J. W. Bandler, and K. Madsen, "A Space-Mapping Framework for Engineering Optimization: Theory and Implementation," IEEE Trans. Microw. Theory Tech., Vol. 54, No. 10, pp. 3721–3730, Oct. 2006.

[70] R. K. Amineh, S. Koziel, N. K. Nikolova, J. W. Bandler, and J. P. Reilly, "A Space Mapping Methodology for Defect Characterization from Magnetic Flux Leakage Measurements," IEEE Trans. Magn., Vol. 44, No. 8, pp. 2058–2065, Aug. 2008.

[71] R. Maryam, R. Amineh, S. Koziel, N. Nikolova, J. Reilly, "Sizing of 3-D Arbitrary Defects Using Magnetic Flux Leakage Measurements," IEEE Trans. Magn., Vol. 46, no. 4, Apr. 2010.

[72] Viktorov, I. A., 1967, Rayleigh and Lamb Waves—Physical Theory and Applications, Plenum Press, New York, NY.

[73] Achenbach, J. D., 1984, Wave Propagation in Elastic Solids, North-Holland Publishing Co., New York, NY.@3# Miklowitz, J., 1978, The Theory of Elastic Waves and Waveguides, North Holland Publishing Co., New York, NY, pp. 409–430; 1984, North-Holland Series in Applied Mathematics and Mechanics, eds., H. A. Lauwerier andW. T. Koiter.

[74] Kino, C. S., 1987, Acoustic Waves: Devices, Imaging and Digital Signal Processing, Prentice Hall Inc., N.J.

[75] Auld, B. A., 1990, Acoustic Fields and Waves in Solids, Vol. 1 and 2, Second edition.; Kreiger Publishing Co., FL.

[76] Graff, K. F., 1991, Wave Motion in Elastic Solids, Dover Publications Inc., New York.

[77] Nayfeh, A. H., 1995, Wave Propagation in Layered Anisotropic Media With Applications to Composites, North-Holland, Elsevier Science B. V., The Netherlands.

[78] Rose, J. L., 1999, Ultrasonic Waves in Solid Media, Cambridge University Press.

[79] R. Christen, A. Bergamini, M. Motavalli, "Three-Dimensional Localization of Defects in Stay Cables Using Magnetic Flux Leackage Methods" JNE, Vol. 22, No. 3, September 2003

[80] A. Bergamini, "Non-destructive testing of stay cables: Field application in South East Asia" http://www.empa.ch/abt116

[81] A. Bergamini, "Nondestructive testing of stay cables", Proceedings IABSE Conference on suspended bridges, Seoul, Korea, 2001

[82] H. Kwan, A. Holt, "Feasibility of under-lagging corrosion detection in steel pipe using the magnetostrictive sensor technique" NDT & E international, Vol. 28, No 4, pp. 211-214, 1995

[83] Jiang Xu *, Cheng Cheng, Xinjun Wu and Anran Ben , "A Magnetic Flux Leakage and Magnetostrictive Guided Wave 7 Hybrid Transducer for Detecting Bridge Cables ", Sensors 2011, 11, 1-x manuscripts; doi:10.3390/s110x0000x

CURRICULUM VITAE

Emad Abdelsalam

Education

	Ph.D., Engineering University of Wisconsin – Milwaukee, Milwaukee, WI
	Parallel Magnetic Resonance Imaging, RF Coils, Signal and Image Processing, Medical systems and Instrumentation and None–destructive Evaluation Methods
1996 -1998	M.S., Electrical Engineering University of Wisconsin – Milwaukee, Milwaukee, WI
1990 -1995	B.S., Electronic Engineering University of Yarmouk, Irbed, Jordan

Industrial and Academic Experience

2010 – Present   Principal Engineer, NeoCoil
Waukesha, WI
- Responsible for the design concepts and implementation of advanced RF coils for MR medical systems
- Responsible for leading the design team for development of the mechanical and electrical parts of the RF coils from concept to product release
- Insure the RF coils products meet clinical specification and are compliant with FDA, ISO, IEC and other regulatory bodies and standards

2008 – 2010   Lead System Designer, General Electric Healthcare (GEHC)
Waukesha, WI
- Leading the RF coil integration team through product requirements development, verification and validation planning and execution according to GE Quality Management System (QMS)
- Insured the RF coil products are compliant with FDA, ISO, IEC and other regulatory bodies and standards
- Worked across functions and teams internally and externally to define new coils design through business need, clinical

requirements, design feasibility, prototype evaluation, risk analysis/mitigation and product release

2007 – 2008   Engineering Project Lead, General Electric Healthcare (GEHC)
Waukesha, WI
- Responsible for leading/managing design and integration efforts for high profile RF coils at 3.0T and 1.5T
- Responsible for insuring that project deliverables are meet with desired technical and performance contents
- Led the team to address and resolve technical risks and challenges throughout the RF coils product development

2005 – 2007   MR Systems Engineer, General Electric Healthcare (GEHC)
Waukesha, WI
- Integrated range of RF coils such as Head, Neurovascular, Spine, Cardiac, Torso, Shoulder, Wrist, Knee and Foot-ankle coils
- Integrated both GE and non-GE RF coils at 1.5T and 3.0T to GE MR scanners
- Integrated GE flexible head coils for Interventional and surgery MR systems
- Tested RF coils to insure they meet safety standards through integration tests such as surface temperature test, B0, B1, and receive field distortion tests
- Tested RF coils to verify and validate they meet design requirements for performance such as SNR, IQ, coverage (FOV), parallel imaging and clinical applications
- Worked with customers, marketing and field personnel to resolve RF coils performance issues such as image quality problems, coil oscillation and poor SNR
- Provided RF coils expertise to serve as the main integrator between hardware, software and field service teams

2004 - 2005   Lecturer, Electrical Engineering Department
University of Wisconsin – Milwaukee, Milwaukee, WI
- Responsible for Electrical Engineering courses

2003 - 2005   Associate Lecturer, Mathematical Sciences Department
University of Wisconsin – Milwaukee, Milwaukee, WI
- Responsible for teaching Algebra courses using traditional classroom teaching and computer-based (ALEKS) teaching

2000 - 2003   Lead Software Engineer, Robotic Vision Systems, Inc.
New Berlin, WI
- Designed, developed and implemented software applications for automated laser/vision-based inspection and packaging systems

- Defined, managed and ensured that objectives and scope of the software tasks are clearly defined, and approved by the engineering staff
- Participated in software testing process through test review, validation and analysis
- Participated in research and development of new hardware and software technologies
- Enhanced machine software/hardware and saved the company over $70,000/year
- Developed a smart software release plane to resolve a $400,000 critical deal
- Supported manufacturing during the customer buy-off procedures
- Provided software support for field service engineers

1999 - 2000   Applications Engineer, Alliance Technologies Group, Inc.
               Vernon Hills, WI
- Developed and implemented software applications for data acquisition and processing, automation and measurements

1997 -1999   Research Assistant, Civil Engineering and Mechanics Department
2005 - 2006   University of Wisconsin – Milwaukee, Milwaukee, WI
- Developed software/hardware to control a robotic machine and to acquire data from magnetic sensors used in Magnetic-Based NDE of Prestressed and Post-Tensioned Concrete Members - The MFL System

- Developed software/hardware to control a robotic machine and to acquire data using wireless PDA and Labview software used in Magnetic-Based and Impact-Echo-Based NDE of structural defects

1996 -1999   Teaching Assistant, Electrical Engineering Department
               University of Wisconsin – Milwaukee, Milwaukee, WI
- Assisted in teaching the following courses: Power electronics, Electronic design lab, Microwave lab, Advanced Engineering Mathematics and Introduction to Microprocessors

Consulting Activities
6/2003 -1/2004   Applications Developer for Civil Engineering and Mechanics Dept
                  University of Wisconsin – Milwaukee, Milwaukee, WI
- Upgraded the Mechanics Lab to run advanced experiments using data acquisition hardware and Labview software

Computer Skills
Programming/Languages: VB.NET, VB 6.0, Java, LabVIEW and C/C++

Systems: Windows NT, Windows 95/98/2000/XP/Vista/7/Pocket PC 2003 and UNIX
Software: BridgeVIEW, LookOUT, HIQ, ALEKS, AutoCAD, ANSYS and MATLAB

Awards
Chancellor's Graduate Student Award, 2003, 2004, 2005 and 2012
University of Wisconsin-Milwaukee, Milwaukee, WI

Publications

1. **Emad Abdelsalam**, Al Ghorbanpoor "MFL System for Detection of Defects in Cables of Bridge Structures" IEEE trans., 2013 (in Progress)

2. A. Ghorbanpoor, **Emad Abdelsalam** "Corrosion Detection in Tendons of Segmental Concrete Bridges" 2012

3. Bo Liu, Leslie Ying and **Emad Abdelsalam**, "Improved Spiral Sense Reconstruction Based On Multiscale Prior Model" IEEE ISBI, 2008.

4. Bo Liu, Leslie Ying and **Emad Abdelsalam**, "Non-iterative Reconstruction of dynamic spiral MRI using temporal model-based method" ISMRM 2007.

5. Leslie Ying, **Emad Abdelsalam**, "A parallel MRI reconstruction algorithm based on a filter-array scheme" ISMRM 2007.

6. B. Liu, L. Ying, Z-P. Liang, D. Xu, **E. Abdelsalam** and J. Sheng "High-Resolution Dynamic Imaging with Spiral Scanning and Spatiotemporal Modeling", ISMRM 2007, pp. 3362

7. **Abdelsalam E**, Ying L and Klemer D, "Parallel MRI Reconstruction: Filter-bank Framework and a New Algorithm", Great Lakes Biomedical Conference, Racine, WI, April 2005.

8. Ghorbanpoor, A., Borchelt, R., Edwards, M. and **Abdelsalam, E**., "Magnetic-Based NDE of Prestressed and Post-Tensioned Concrete Members - The MFL System," Final Report No. FHWA-RD-00-026, Federal Highway Administration, U.S. Department of Transportation, May 2000, 107 pages.

9. **Emad Abdelsalam**, "Design and Implementation of Algorithms Applied in Detection of Structural Defects," M.S. Thesis, Electrical Engineering, University of Wisconsin-Milwaukee, August 1998